The Thesis committee for Luke Adam Decker
Certifies that this is the approved version of the following thesis:

Seismic Diffraction Imaging Methods and Applications

APPROVED BY

SUPERVISING COMMITTEE:

Sergey Fomel, Supervisor

Kui Ren

Clark Wilson

Seismic Diffraction Imaging Methods and Applications

by

Luke Adam Decker, B.S., B.A.

THESIS

Presented to the Faculty of the Graduate School of

The University of Texas at Austin

in Partial Fulfillment

of the Requirements

for the Degree of

Master of Science in Geological Sciences

THE UNIVERSITY OF TEXAS AT AUSTIN

May 2014

For everything and everyone that got me here and kept me from going back.

Acknowledgments

This thesis would not have been possible without so much help from so many people.

First of all, thank you to my family: my parents Gary and Betty, and brother, Adam, for their love and support.

Thank you to my adviser and co-author Professor Sergey Fomel. I collaborated with him on Decker et al. (2013), which evolved into a large part of the second chapter of this thesis. He selflessly offered me first authorship on Decker and Fomel (2014), which became this thesis' third chapter, despite the fact that the theoretical work was his. Under his guidance Decker et al. (2014) was authored, which became this thesis' fourth chapter. I could not have succeed at Texas without his brilliant guidance and patient support.

Dr. Alexander Klokov, of the Bureau of Economic Geology provided me with valuable guidance into using Madagascar, computer programming, and the nature of diffractions. We collaborated on Decker et al. (2013) and Decker and Klokov (2014), which combined form the ideas behind the bulky second chapter of this work.

I am grateful to Dr. Xavier Janson of the Bureau of Economic Geology's Reservoir Characterization Research Laboratory, my co-author on Decker et al. (2014) for his expertise in carbonate systems.

Processing for this thesis was accomplished using the Madagascar software library (Fomel et al., 2013a). I am grateful to all the Madagascar programmers and

contributors for providing the tools I needed to succeed.

My consortium mates at the Texas Consortium of Computational Seismology have been a tremendous source of inspiration and aid. In particular I am grateful to my mentor, Dr. Vladimir Bashkardin, for setting me on the right path as a graduate student, and my office-mate Yanadet Sripanich, for his enthusiasm, technical help, and enlightening conversation.

Without the help of my undergraduate advisers, Professor Jackie Caplan-Auerbach of Western Washington University, Professor Kurt Hoffman of Whitman College, and Professor Pat Langhorne of the University of Otago, I would not have had the background in research and the scientific method that enabled me to pursue my graduate degree. Thank you to Professor Dana Burgess of Whitman College for freeing my mind to think.

I am grateful to all the people at King Canyon Buffalo who helped me learn the art of Mudlogging and the value of hard work, particularly Chris Nerud, Phil Littlefield, and John Hook.

Thank you to my Master's committee members, Professor Sergey Fomel, Professor Kui Ren of The University of Texas at Austin's math department, and Professor Clark Wilson of the Jackson School of Geosciences, for reading and improving my thesis.

I am thankful to sponsors of the Texas Consortium for Computational Seismology for supporting my education. Additional partial financial support of my research was provided by Shell and RPSEA through the Ultra-Deepwater and Unconventional Natural Gas and Other Petroleum Resource program authorized by the US Energy Policy Act of 2005. RPSEA (http://www.rpsea.org/) is a nonprofit corporation whose

mission is to provide a stewardship role in ensuring the focused research, development and deployment of safe and environmentally responsible technology that can effectively deliver hydrocarbons from domestic resources to the citizens of the United States. RPSEA, operating as a consortium of premier US energy research universities, industry, and independent research organizations, manages the program under a contract with the US Department of Energys National Energy Technology Laboratory.

Seismic Diffraction Imaging Methods and Applications

Luke Adam Decker, M.S.Geo.Sci.

The University of Texas at Austin, 2014

Supervisor: Sergey Fomel

Seismic waves can either be reflected or diffracted by subsurface objects depending on the object's geometry. Diffactions can be used to determine details about the small-scale features that generate them, such as karsts, voids, pinchouts, faults, fractures, and salt flanks. Diffraction imaging can have resolution below the typical seismic wavelength. Scattered waves are recorded as significantly lower-energy signal than reflected waves, requiring that diffractions be separated from reflections. I describe three methods of such separation: data-domain plane-wave destruction, Fresnel zone Elimination, and partial-image plane-wave destruction. Once separated, diffractions can be migrated to create a seismic diffraction image and used in velocity analysis.

Common-reflection angle migrated diffractions appear flat in dip angle gathers when migrated with correct velocity. I illustrate how this property can be used to determine migration velocity through a process of oriented velocity continuation (OVC). In OVC framework diffraction data are decomposed by slope and migrated over a range of velocities. Velocities corresponding to the flattest slope gathers are

picked using semblance as a measure of flatness. This provides an estimate of migration velocity. Stacking gathers corresponding to this chosen velocity generates a seismic diffraction image.

Seismic diffraction images provide interpreters with information about small-scale geologic objects that may not be available in conventional images. Scattering features that are interesting for exploration, like voids, caves, fractures, and faults, cause diffractions and can be resolved with better focus in diffraction images than in conventional ones. This is particularly useful with geologically complex carbonate systems. Carbonates are strongly heterogeneous, making them difficult to image with conventional methods. Reservoir porosity is often contained within caves, or small vugs. These features are difficult to characterize with conventional methods because cave reflections have large geometric uncertainties in cave size and location. Velocity analysis of seismic reflection data in carbonates may not highlight vugular porosity particularity well. I illustrate how diffraction images provide improved characterization by highlighting the edges of caves, thus constraining cave geometry, and highlighting more heterogenous zones by measuring the amount of scattering those zones generate.

Table of Contents

List of Tables

List of Figures

Chapter 1

Introduction

One of the goals exploration geophysicists have is to characterize the subsurface through non-invasive methods; to determine underlying lithology and structure without direct observation. Various established techniques exist to accomplish this goal, including gravity and magnetic anomaly surveys, resistivity surveys, earthquake monitoring, ground penetrating radar imaging, and seismic reflection imaging (Burger et al., 2006). Of these methods, seismic reflection imaging has become the most used tool for petroleum exploration, and the preferred means for generating images of the Earth's shallow crust (Crummett, 1986; Fehler and Huang, 2002). Seismic reflection imaging has been effective at determining the geometry of strongly reflective strata and estimating seismic velocities. Seismic reflector geometry and velocity can be used to prospect, map, and risk key petroleum system elements, including seals, reservoirs, source rocks, and migration pathways (Onajite, 2013). While seismic reflection imaging works well for providing information about strong reflectors that curve smoothly, it only provides information at scales larger than seismic wavelength. For smaller-scale details we can turn to seismic diffractions, which Khaidukov et al. (2004) referred to as the "abandoned stepchildren of traditional seismic processing and imaging".

Seismic reflection and diffraction are fundamentally different phenomenon and their signals have different properties Klem-Musatov (1994). Diffractions interfere with but carry much less energy than seismic reflections, requiring that they be ex-

tracted to be successfully used. Because seismic diffraction signal is scattered while reflection signal is coherent, diffraction signals can contain more information about the scattering feature that produced them. Therefore, seismic diffractions can help to spatially locate diffracting objects with potentially greater accuracy than seismic reflections (Neidell, 1997). Diffractions occur when seismic waves interact with objects smaller than their wavelength. Therefore, using diffractions imaging super-resolution, or resolution below wavelength, may be possible (Khaidukov et al., 2004). This potential for improved resolution is intriguing, because diffractions are caused by geologically interesting features for petroleum exploration – faults, fractures, salt flanks, voids, pinchouts, unconformities, etc. (Khaidukov et al., 2004; Fomel et al., 2007; Moser and Howard, 2008; Klokov and Fomel, 2012; Sturzu et al., 2013) and better resolving these objects should lead to more accurate exploration. Because seismic diffraction signal takes more diverse routes after interaction with an object than reflection signal, it may also lead to a more accurate seismic velocity analysis (Neidell, 1997).

The purpose of this work is to investigate the promise seismic diffractions have for seismic processing and small-scale interpretation, to address Khaidukov et al. (2004)'s observation that "diffraction always needs more advertising". To accomplish that goal, I will first review the concept of seismic diffractions and discuss several methods through which they might be most effectively separated from reflections. Illustrations of the benefits of seismic diffraction imaging follow. I will introduce a new method for estimating seismic velocity using diffractions. Then I use seismic diffractions to image small-scale subsurface features with improved resolution relative to conventional reflection imaging. I hope the examples of diffraction imaging's usefulness will inspire other researchers to dedicate time to researching beneficial

applications of seismic diffraction imaging.

In Chapter 2, I introduce the concept of diffractions as wave-phenomenon and illustrate some of their properties.

In Chapter 3, I illustrate three methods of seismic diffraction extraction: data-domain plane-wave destruction (DD-PWD), Fresnel-zone elimination, and partial-image plane-wave destruction (PI-PWD). DD-PWD uses the different kinematics of reflection and diffraction signals in common-offset data to extract reflections. Fresnel zone elimination removes the stationary-phase portion of specular events (reflections) in migrated dip-angle gathers so that they no longer appear after stacking. I propose a new method of diffraction extraction, partial-image plane-wave destruction, which modifies the DD-PWD workflow to operate on migrated dip-angle gathers to remove the stationary-phase portion of reflections through plane-wave destruction rather than a mask. All three methods are applied to a synthetic toy model and two field data sets. I find that Fresnel zone elimination can remove more diffraction energy than the other two PWD based methods. PI-PWD removes more remnant reflection energy than DD-PWD in regions with complex geometries. The added expense of plane-wave destruction in the gather dimension required for partial-image plane-wave destruction entails that DD-PWD is best suited for most cases, and that PI-PWD is best suited for diffraction extraction in areas with complicated structures where DD-PWD might not remove all reflection energy.

In Chapter 4, I introduce a method for determining migration velocity by flattening diffraction events in decomposed slope gathers using oriented velocity continuation. The method decomposes zero-offset diffraction data by slope and then propagates decomposed diffraction data over a range of migration velocities. The

correct migration velocity corresponds to the flattest diffraction events. Semblance is used as a measure of event flatness in these continued slope gathers, and velocities with the highest semblance are selected, indicating the migration velocity that best flattens diffraction events. Picking the gathers corresponding to this maximum semblance generates a diffraction image.

In Chapter 5, I conduct 3D diffraction imaging experiments using two carbonate synthetic models. These experiments illustrate how seismic diffraction imaging can be used to better resolve geologically interesting features or highlight heterogeneous zones that might be less apparent in a conventional reflection image. In these experiments I generate synthetic zero-offset data, separate seismic diffractions using data-domain plane-wave destruction, and migrate the diffraction and complete data to generate diffraction and conventional images. I find that using the diffraction image highlights some geologically interesting features including voids, karsts, and heterogeneous strata in the synthetic models.

Chapter 6 concludes the thesis by providing a brief review of the material presented.

Chapter 2

Seismic Diffractions

Wave Propagation

Elastic perturbations spatially propagate as waves. The behavior of these waves is determined by the media through which they travel. Seismic imaging studies are primarily concerned with seismic waves traveling through the Earth. The behavior of these waves is unsurprisingly determined by elastic modulii and density of the rocks through which they propagate. These attributes determine the velocity with which the wave propagates. The two types of seismic waves are primary (P) and secondary (S) waves. P-waves transport changes in compression through a medium, and are able to propagate through solids and fluids alike. S-waves transport shear deformation through solid media, and do not propagate through fluids (Stein, 2002; Chapman, 2004; Fowler, 2004). Media properties determine the velocities at which these waves propagate via the following equations:

$$V_p = \sqrt{\frac{K + \frac{4}{3}\mu}{\rho}} \tag{2.1}$$

and

$$V_s = \sqrt{\frac{\mu}{\rho}} \tag{2.2}$$

where K is the bulk modulus of the media, a measure of incompressibility, μ is the shear modulus, a measure of rigidity, and ρ is the material density (Stein, 2002; Chapman, 2004; Fowler, 2004). The P-wave velocity is always greater than the S-wave velocity. Velocity and density combine to form a quantity known as acoustic

impedance, a measure of how much pressure is generated within a medium by vibrations, which is defined in an unperturbed medium by

$$Z_0 = V_0 \rho_0 \tag{2.3}$$

where V_0 and ρ_0 are the velocity and density of an unperturbed medium. Reflectivity can be defined as the spatial derivative of acoustic impedance (Stein, 2002; Chapman, 2004; Fowler, 2004).

Acoustic waves may be reflected or transmitted when they encounter a change in acoustic impedance. The strength of the reflected and transmitted portions of the wave is proportional to the reflectivity of the interface; how large a density and velocity contrast exists there, as well as the incident angle. Fermat's principle states that a wave will take the path through a medium corresponding to a stationary travel time and governs the change in direction that a wave experiences as it passes through an interface (Stein, 2002; Chapman, 2004; Fowler, 2004).

Reflection and diffraction as backscattering phenomenon

The behavior of a propagating acoustic wave is easier to understand and explain if we examine the context of an asymptotically high frequency wave, or a ray, and look at the propagating media as a set of different regions each with their own velocities and densities, and with a surface in between where velocities and densities instantaneously change. Reflectivity is therefore only non-zero at these surfaces. This ray describes the wave as a particle traveling through space, its path defined by a curve (Červený, 2001). If we imagine a vector normal to the reflecting surface, a surface with a high impedance contrast giving rise to a large amount of reflectivity, a reflected ray will have the same inclination angle with the normal as the incoming

ray (Stein, 2002; Chapman, 2004; Fowler, 2004).

If a reflecting surface has complex geometry the normal vector may change rapidly over short distances, which implies that a small perturbation in reflecting point location will result in a much different reflected vector direction. This can hold true for regions where the reflecting surface has large curvature, or where a vertical discontinuity exists. Inbound rays, which run parallel to each other, and may be described by a ray tube, or a geometric bundle of rays that only have energy flux at the ends, will be scattered and no longer be parallel to each other after reflection on this irregular surface. Compare this to a tube of rays reflecting off a planar surface. If the inbound rays are parallel, the outbound rays will also be. This scattering is known as wave diffraction, and diffracted rays may no longer be described by ray tubes containing bundles of parallel rays; the rays now have different directional vectors and any ray tube of diffracted rays will have flux out its sides as well as its end. Reflection occurs if the radius of curvature of a reflecting surface is greater than that of inbound ray wavelength. For reflecting surfaces with smaller radius of curvature than ray wavelength, diffraction occurs (Klem-Musatov, 1994; Khaidukov et al., 2004).

If we consider diffractors as regions which will change rays from neat bundles of ray tubes to scattered non-parallel rays, we find that in addition to reflective regions with irregular surface geometry, caustics which focus inbound rays to single point also create diffractions. Diffractions occur when rays which are initially parallel lose their parallel travel paths (Klem-Musatov, 1994). Diffractions and reflections are therefore the ends of a continuum of reflective backscattering behavior; no firm boundary between the two exists, and an interaction with a reflecting surface may have both diffractive and reflective components (Khaidukov et al., 2004).

Key differences between reflection and diffraction signals

The scattered nature of diffracted signals and the ordered nature of reflected signals lead to some key differences which may be advantageously used for velocity model creation or geological interpretation.

I use a simple model to demonstrate the appearance of reflections in an ideal seismic reflection experiment. Utilizing a constant velocity of $v = 1.0$ and varying the density along a flat interface, I generate an acoustic impedance model, Figure 2.1a. I then use seismic exploding-reflector modeling with lowrank approximation (Fomel et al., 2013b) to create a modeled zero-offset reflection response, Figure 2.1b. Notice how the modeled reflection event is quite planar.

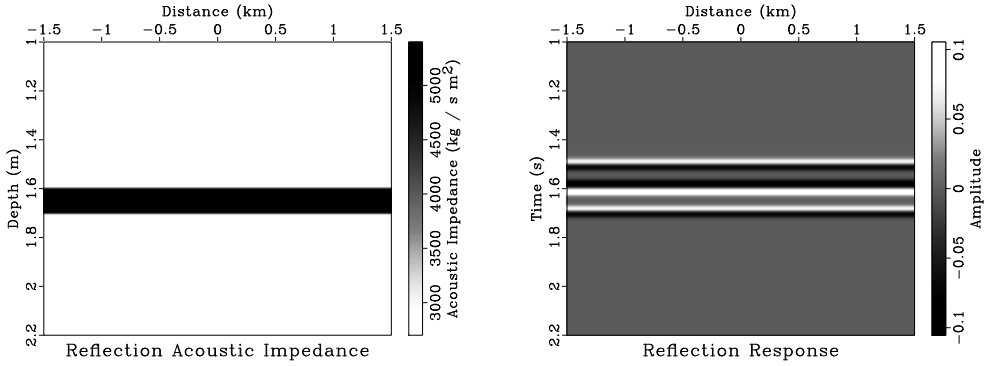

a b

Figure 2.1: (a) Synthetically generated acoustic impedance simulating a flat reflector; (b) Modeled reflection response chap01/simple ait-r,exp-r

Because of the scattering of diffraction signals, different diffracting rays may take different ray paths. A diffraction behaves as a secondary source in the subsurface (Keller, 1962), so scattered energy will travel along different paths with different slopes, traversing very different regions of the subsurface. The amount of diffraction energy recorded at a surface geophone can be about an order of magnitude lower than

reflection energy, entailing that a wide geophone aperture needs to be used to collect sufficient energy from a single diffractor. The advantage of using diffractions' scattered ray path trajectories is that they provide more information about the location of a scattering object than the relatively uniform reflecting rays do about a reflector (Neidell, 1997).

I use a simple model to demonstrate the appearance of diffractions in an ideal seismic reflection experiment. Utilizing again a constant velocity of $v = 1.0$ and increasing the density at a single point I create a point scattering object, whose acoustic impedance is visible in Figure 2.2a. I then use seismic exploding-reflector modeling to create a modeled diffraction response, Figure 2.2b. The diffraction event tails away in a hyperbola from the point scattering object.

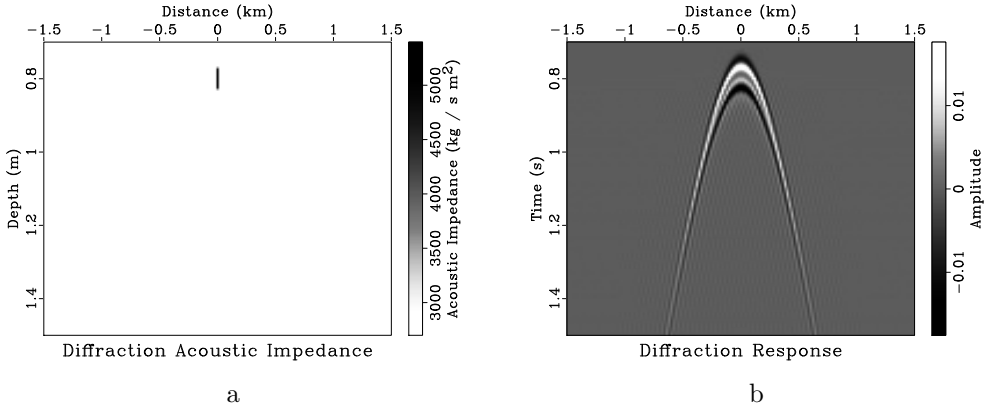

Figure 2.2: (a) Synthetically generated acoustic impedance simulating a point scattering object; (b) Modeled diffraction response chap01/simple ait-d,exp-d

Utilizing seismic diffractions

Seismic diffraction signal can be about an order of magnitude weaker than reflection signal (Klem-Musatov, 1994). This necessitates the separation of the two

phenomena for the effective use of diffractions in processing or interpretation (Klokov and Fomel, 2012). I illustrate the difference in diffraction and reflection energy with a simple synthetic model. I generate acoustic impedance for a point scattering object located above a planar reflector by varying density and holding velocity constant at $v = 1.0\frac{km}{s}$. The generated acoustic impedance is visible in Figure 2.3a. The modeled seismic response is shown in Figure 2.3b. The hyperbolic diffraction event is much weaker than the strong planar reflection event.

Realistically the diffraction and reflection signals may not be so spatially separated and easily distinguishable from each other. In the next chapter I investigate different methods of separating diffraction signals from reflection signals in more realistic situations.

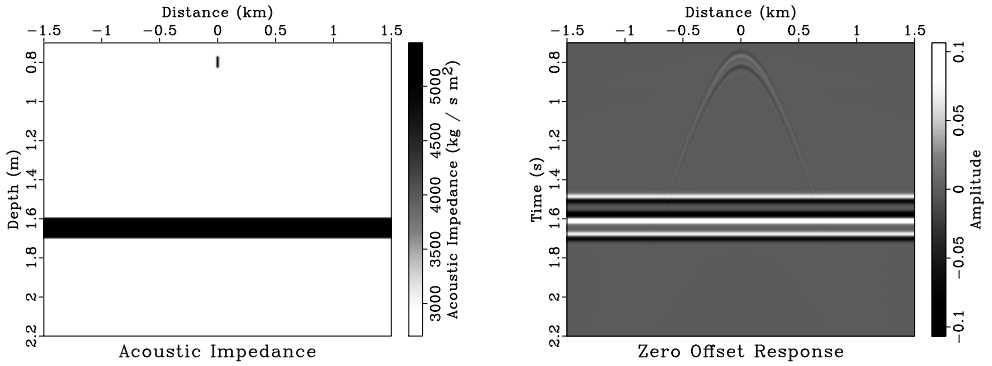

a b

Figure 2.3: (a) Synthetically generated acoustic impedance simulating a point scattering object situated above a planar reflector; (b) Modeled response chap01/simple ait-c,exp-c

Chapter 3

Separating Diffractions

MOTIVATION

As discussed previously, seismic diffraction imaging provides much promise for imaging the geologically interesting features that produce them with greater resolution than conventional seismic reflection imaging (Khaidukov et al., 2004), and can be advantageously used for determining velocity (Harlan et al., 1984; Sava et al., 2005; Fomel et al., 2007; Reshef and Landa, 2009). Because seismic diffraction signal is significantly lower energy than reflection signal, diffractions must be separated from a data set or they may be lost among the more energetic specular reflection events (Berkovitch et al., 2009).

Several methods of diffraction discrimination exist, which utilize different criteria. Different methods utilize different properties of diffractions and reflections to filter one from the other, and operate in different domains. An early effort by Harlan et al. (1984) focused on properties of diffractions in the local slant-stack domain. Landa et al. (1987) used differences in travel time properties between diffracted and reflected waves when viewed in common-offset sections to automate diffraction detection. Kanasewich and Phadke (1988) proposed a new form of moveout and amplitude correction to enhance diffraction signal, creating common-fault-point stacked sections. Landa and Keydar (1998) proposed a method of imaging diffractions by

*Parts of this chapter were submitted as (Decker et al., 2013) and (Decker and Klokov, 2014)

focusing energy around common-diffraction points. Fomel (2002) and Fomel et al. (2007) expanded and applied plane-wave destruction filters, first developed by Claerbout (1992), to isolate diffraction from reflection signal in un-migrated common-offset or stacked data. Taner et al. (2006) applied this method in the common-plane-wave domain. Khaidukov et al. (2004) used the difference between reflection and diffraction moveouts to focus reflections and diffractions at different depths, remove reflections, and then de-focus. Landa et al. (2008) and Klokov and Fomel (2012) developed methods for isolating diffractions in migrated dip-angle gathers (Kozlov et al., 2004; Moser and Howard, 2008). Sturzu et al. (2013) developed an algorithm incorporated in Kirchhoff migration loops which filters objects satisfying Snell's law, reflections, leave diffractions and other events that do not.

In this chapter I explore and illustrate two well documented forms of diffraction extraction: data-domain plane-wave destruction (Fomel et al., 2007) and dip-angle gather Fresnel zone elimination (Moser and Howard, 2008). Additionally, I alter the data-domain plane-wave destruction workflow to propose a new method of diffraction separation, partial-image plane-wave destruction, which may lead to better signal separation relative to traditional methods in regions with complex geology.

The three methods are first illustrated on a toy model initially created by Moser and Howard (2008) and reproduced by Al-Hadab (2012). They are then applied to two sets of Gulf of Mexico field-data: one containing a set of faults and the other a salt dome.

The three imaging experiments utilize angle-domain migration. This means that source and receiver or common-midpoint and offset coordinates are replaced by angular coordinates such as ray takeoff angle to source and receiver, or migration dip

and scattering angle. This form of migration uses angular rather than Cartesian coordinates to define locations in the subsurface. Through this transformation problems related to multi-pathing are reduced (Ursin et al., 2005). Angle-migration can output a set of dip-angle gathers (Xu et al., 2001). Constant-dip-angle traces constitute a set of partial-images – seismic images of the subsurface obtained after migration using a single dip angle. Stacking these partial-images over dip-angle creates an image (Klokov and Fomel, 2012, 2013b).

DATA-DOMAIN PLANE-WAVE DESTRUCTION

Plane wave destruction (PWD) filters, pioneered by Claerbout (1992) and extended by Fomel (2002), try to follow locally linear patterns of energy in data to determine the dominant local slope. They accomplish this by attempting to map data onto adjacent traces and determining the vertical shift necessary to minimize residual energy not predicted by the mapped trace. The filters can be accelerated using Newton's algorithm to attain more rapid convergence (Chen et al., 2013a) and improved to provide results even when slopes are sufficiently steep to cause spatial aliasing in the data (Chen et al., 2013b). The filters have many important applications including trace interpolation, signal and noise separation, and model regularization for use in coherency enhancement, velocity estimation, and multiple suppression (Fomel, 2002; Fomel and Guitton, 2006). For this chapter I am mostly interested in their use for diffraction imaging (Fomel et al., 2007).

Seismic wavefields resulting from reflections may be represented as local plane-waves which follow the following two-dimensional linear partial differential equation

for a wavefield u with plane-wave slope σ (Claerbout, 1992):

$$\frac{\partial u}{\partial x} + \sigma \frac{\partial u}{\partial t} = 0 \tag{3.1}$$

Conveniently, this provides a way for discriminating between reflection and diffraction events in the un-migrated data-domain. Slope, $\sigma(x,t)$, may be estimated using PWD at all points in the seismic data set. All data conforming to local slope are removed. This leaves the residual, including the set of diffractions, which are non-planar in the data-domain, as well as incoherent noise present in the data. The method relies on the assumption that reflection events have smoothly varying curvature. Field data may be polluted by noise, so additional regularization, often taking the form of a smoothing filter, is needed for output slope stability (Fomel, 2007; Chen et al., 2013a).

Several parameters need to be chosen for PWD slope estimation. The first is the order of the plane-wave destruction, which determines how many adjacent time samples will be used for slope estimation. Shaping regularization parameters must also be declared, typically taking the form of smoothing radii. To output a slope field for an N dimensional data-set there are therefore $N+1$ key parameters, which include the order of the plane-wave destruction and the shaping radius in each dimension.

Illustration of Data-Domain Plane-Wave Destruction

My first illustration of data-domain plane-wave destruction (DD-PWD) begins with a simple toy model created by Moser and Howard (2008) and previously reproduced by Al-Hadab (2012). The model, shown in Figure 3.1a features a flat reflector broken by a curved graben-like structure centered about a distance of 1 km, and a square graben, centered about a distance of 2.75 km. Zero-offset data are generated

using Kirchhoff modeling and a constant velocity of 1. Data are visible in Figure 3.1b. Data slope, shown in Figure 3.2a, is estimated using plane-wave destruction methods. I remove data conforming with local slope, providing the result shown in Figure 3.2b.

I then migrate the zero-offset data, Figure 3.1b using Kirchhoff angle-migration (Xu et al., 2001) to provide the conventional image, Figure 3.3a. The same is done to the data-domain plane-wave destruction data, Figure 3.2b to provide the data-domain plane-wave destruction diffraction image, Figure 3.3b.

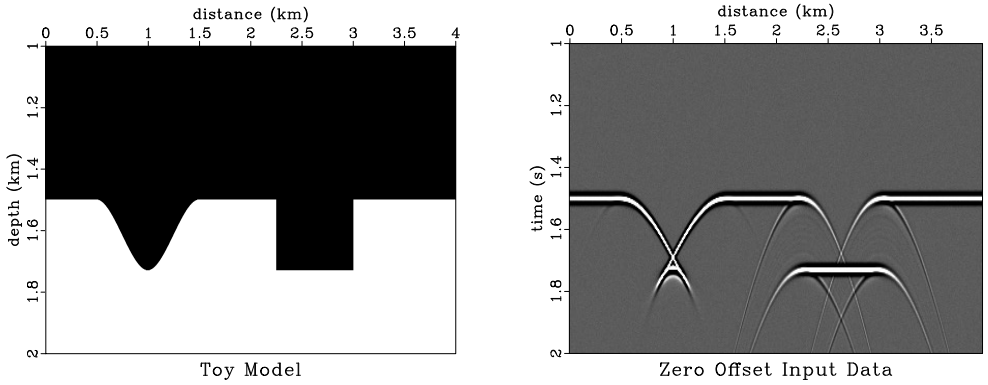

a b

Figure 3.1: (a) Toy model created by Moser and Howard (2008) and reproduced by Al-Hadab (2012); (b) Modeled zero-offset data chap02/toy m0,model0

Examining the diffraction image in Figure 3.3b, note that the method successfully isolated and imaged the diffractions arising from edge phenomenon at the corners of the square graben. The edges at distances of 2.25 km and 3 km at depths of 1.5 and 1.7 km have become very neatly isolated points. This demonstrates the strength of DD-PWD in environments where the assumptions of the method are satisfied. One can demonstrate that these points contain diffraction energy by examining dip-angle gathers (DAGs). In these gathers, correctly migrated diffraction energy appears flat, while reflections take the form of upward pointing hyperbolas (Audebert et al., 2002).

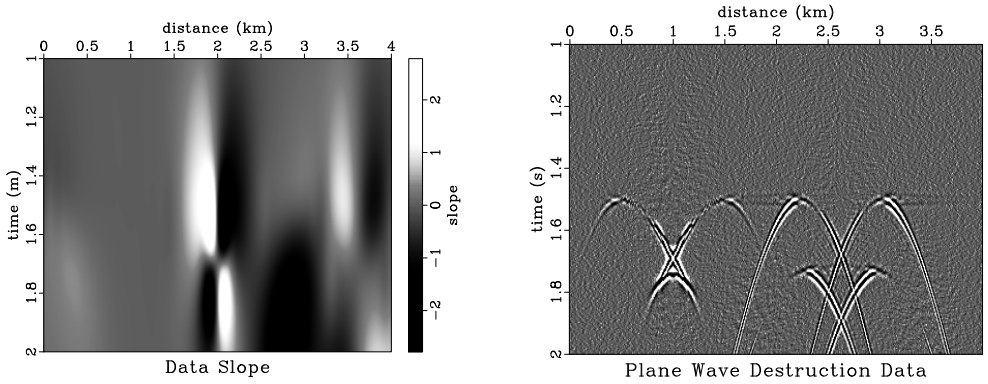

a b

Figure 3.2: (a) Toy model zero-offset data slope; (b) Plane-wave destroyed toy model data chap02/toy slope0,smsu0

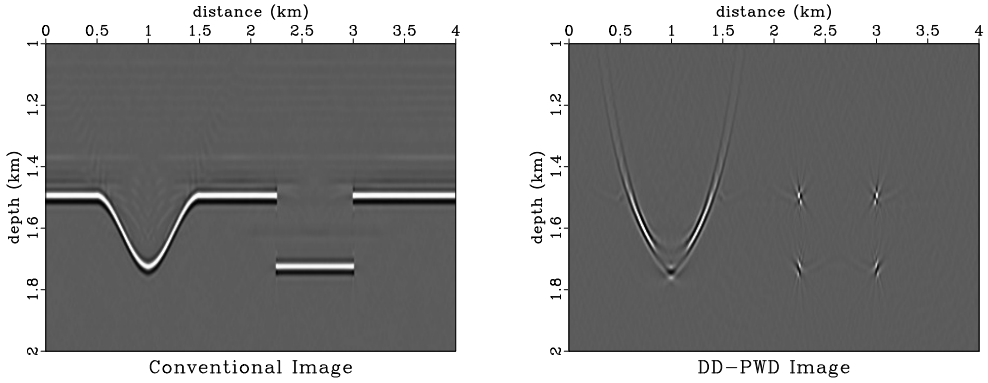

a b

Figure 3.3: (a) Conventional reflection image from migration of Figure 3.1b; (b) Toy model data-domain plane-wave destruction diffraction image from migration of Figure 3.2b chap02/toy toy-model-image0,toy-smsu-image0

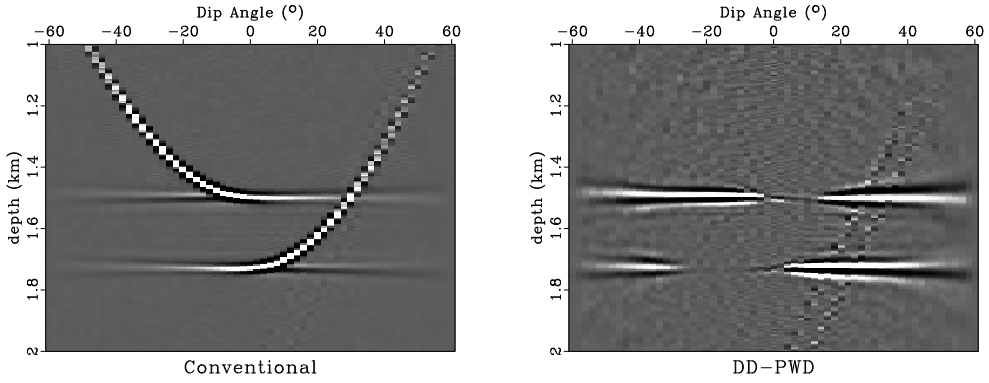

a b

Figure 3.4: Two dip-angle gathers (DAGs) centered about distance 3 km, the right edge of the square graben, in the toy model: (a) DAG from the conventional image; (b) DAG from the PI-PWD image chap02/toy onemodel-dagT1,onesmsu-dagT

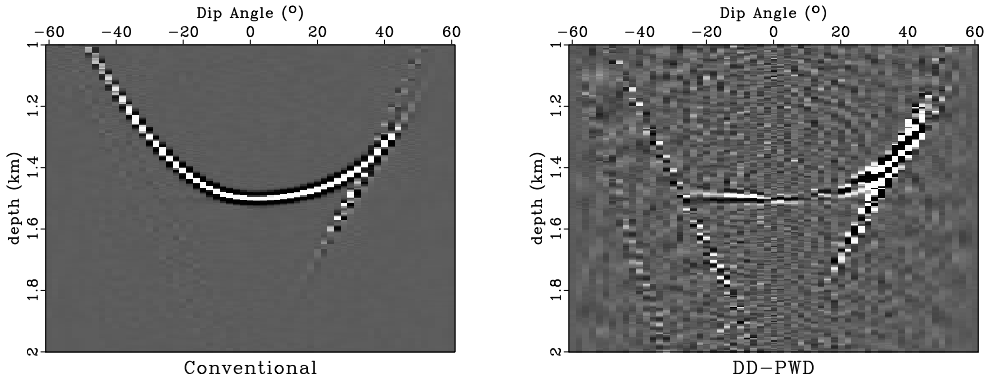

a b

Figure 3.5: Two dip-angle gathers (DAGs) centered about distance 1.5 km, the right edge of the curved graben, in the toy model: (a) DAG from the conventional image; (b) DAG from the PI-PWD image chap02/toy threemodel-dagT1,threesmsu-dagT

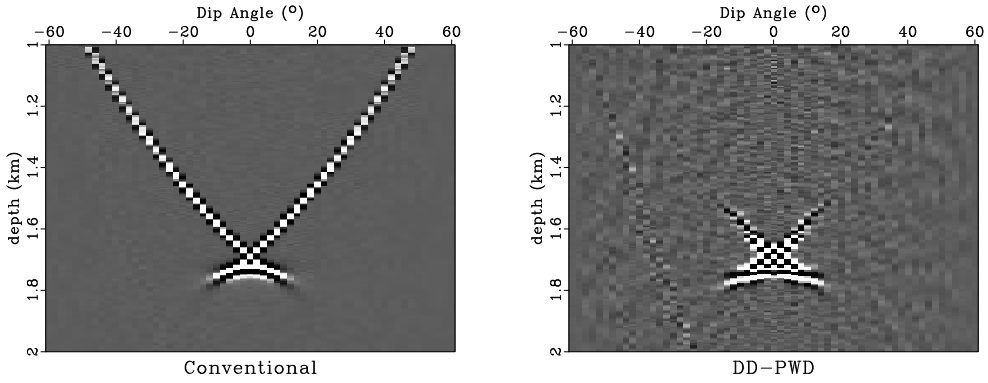

Figure 3.6: Two dip-angle gathers (DAGs) centered about distance 1 km, the center of the curved graben, in the toy model: (a) DAG from the conventional image; (b) DAG from the PI-PWD image chap02/toy twomodel-dagT1,twosmsu-dagT

A DAG from distance 3 km, the right edge of the square graben, is visible for the conventional image in Figure 3.4a and the DD-PWD image in Figure 3.4b. Figure 3.4a contains half-reflections bending upward and intersecting flat diffraction lines at 1.5 and 1.75 km depth. In Figure 3.4b only the flat diffraction events spanning depths 1.5 and 1.75 km remain, indicating that DD-PWD has successfully removed specular reflections but left diffraction signal in this portion of the image.

This experiment provides an illustration of one of the limitations of DD-PWD: the requirement of continuously variable curvature. When zero-offset data are modeled in Figure 3.1b a "bow tie" event appears centered beneath a distance of 1 km. Crossing dips exist at this event, and dip is no longer continuously variable. Expectedly, the PWD filter has difficulty predicting adjacent data there, and as is visible in Figure 3.2a, the filter is unable to predict the curved graben's slope near a distance of 1 km, so the slope is estimated to be near zero. When data conforming to local slope are extracted in Figure 3.2b the "bow tie" event remains, along with a hyperbolic

quasi-diffraction caused by the large curvature at the base of the curved graben. This event is migrated into a half-ellipse, centered about distance 1 km in Figure 3.3a, which is the most prominent feature in the diffraction image.

We can detect that this ellipse is not diffraction energy by comparing DAGs from distance 1.5 km, the right edge of the curved graben. Figure 3.5a contains the DAG for the conventional image and Figure 3.5b contains the DAG for the DD-PWD diffraction image. Note that the upward bending "smile" present in Figure 3.5a has been removed by DD-PWD in Figure 3.5b and that there is a small amount of flat diffraction energy present at a depth of 1.5 km. The ellipse artifact manifests itself as a white blob at an inline slope of 25° and a depth of 1.4 km, which is where it manifests itself below distance 1.5 km. The fact that this energy takes a distinctly non-planar form in the DAG implies that it is not diffraction energy.

Interestingly, the quasi-diffraction at the base of the ellipse and the curved graben have been successfully imaged by PI-PWD. DAGs located at distance 1 km, the center of the curved graben, are visualized for the conventional image in Figure 3.6a and the DD-PWD diffraction image in Figure 3.6b. Steeply upward curving arms from the mixed reflection-diffraction are visible in Figure 3.6a, as is a flat diffraction event near a depth of 1.75 km. Most of the upward curving arms are removed by DD-PWD in Figure 3.6b, and the flat diffraction line remains. A small amount of the arms remains as a cross in the DAG, which after stacking over inline slopes, becomes the faint artifact visible near the depth of 1.7 km and distance 1 km in Figure 3.3b.

FRESNEL ZONE ELIMINATION

The different appearance of reflections and diffractions when viewed in dip-angle gathers (DAGs) following Kirchhoff angle-migration may be used to separate reflections from diffraction events. As mentioned above, correctly migrated diffractions appear flat when viewed in a DAG centered directly on them. Reflections appear as upward bending parabolas or "smiles" with stationary points at their minima, the Fresnel zones, which occur at reflectior dips (Audebert et al., 2002). Kozlov et al. (2004) proposed a method for attenuating specular reflections and making diffractions more apparent by introducing tapering to Kirchhoff angle migration. This taper attenuated reflection Fresnel zones and thus made reflections less apparent than diffractions in the stacked image. Moser and Howard (2008) expanded on the concept, muting Fresnel zones in depth domain angle-migrated images to create a diffraction image. Klokov and Fomel (2012) were able to analytically represent diffractions and reflections in the dip-angle domain, and use the differing geometric properties of the two kinds of events to distinguish between them in dip-angle gathers transformed to the hybrid Radon space. Klokov and Fomel (2013a) demonstrated that a diffraction image could be formed by stacking along diffraction curves in partial-images formed by slicing a set of dip-angle gathers along constant dips, in a method called secondary migration, which could be used to amplify diffraction energy and reduce noise in Kirchhoff angle-migrated data-domain plane-wave destruction images.

Illustration of Fresnel Zone Elimination

I use the synthetic toy example from the previous section to demonstrate diffraction extraction by Fresnel zone elimination. As before, I begin with the zero-

offset data generated for the DD-PWD illustration, visible in Figure 3.1b. This data is migrated using Kirchhoff angle migration (Xu et al., 2001; Klokov and Fomel, 2013b) to produce a set of dip-angle gathers, Figure 3.7, which are stacked over inline slope to create an image, Figure 3.8a. Slopes are estimated for the stacked image and converted to dip angles (Figure 3.8c). This dip is used to construct a set of tapers, one of which is visible in Figure 3.9c. These tapers mute out reflection stationary points from angle-gathers in Figure 3.7 to produce a set of Fresnel zone eliminated angle-gathers. One such muted gather is shown in Figure 3.9b. These Fresnel zone eliminated gathers are stacked over slope to produce the Fresnel zone elimination diffraction image, shown in Figure 3.8b.

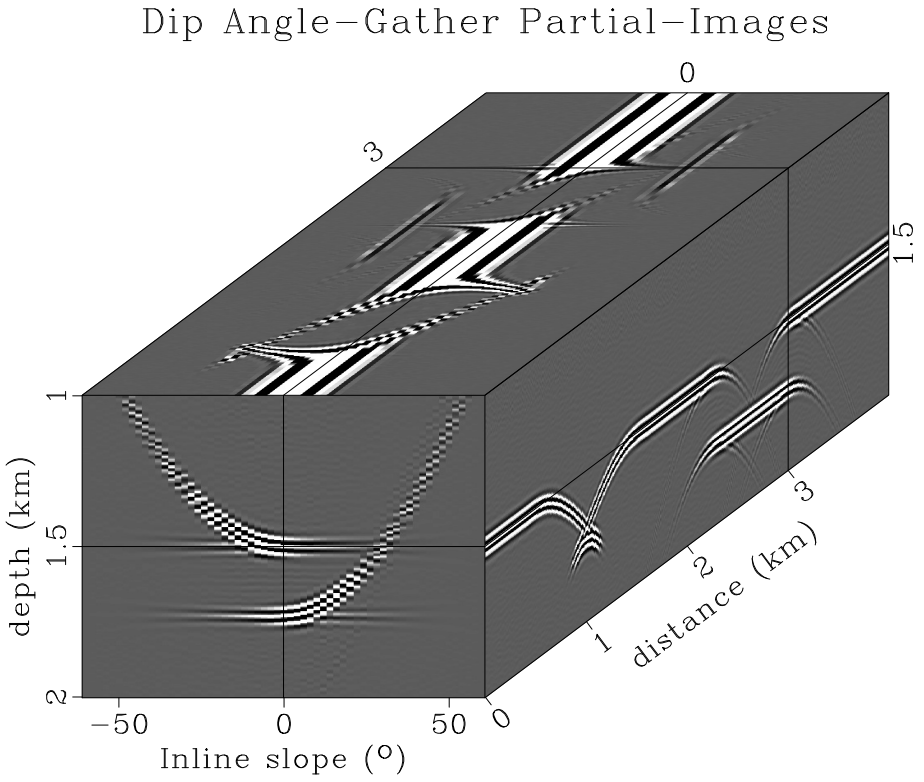

Figure 3.7: Toy model dip-angle gathers from Kirchhoff angle-migration chap02/toy pi1

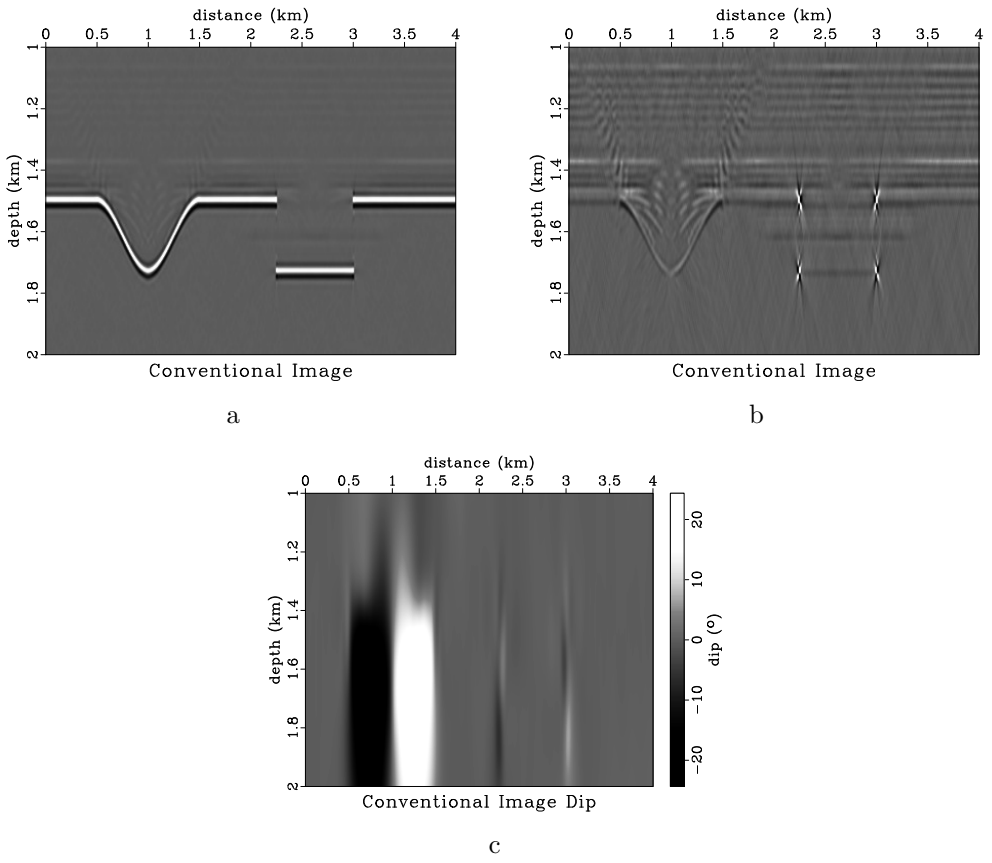

Figure 3.8: (a) Migration image produced by stacking Figure 3.7 over inline slope; (b) Fresnel zone elimination diffraction image; (c) Calculated dip for Figure 3.8a chap02/toy model-image1,ad-image0,img-dip0

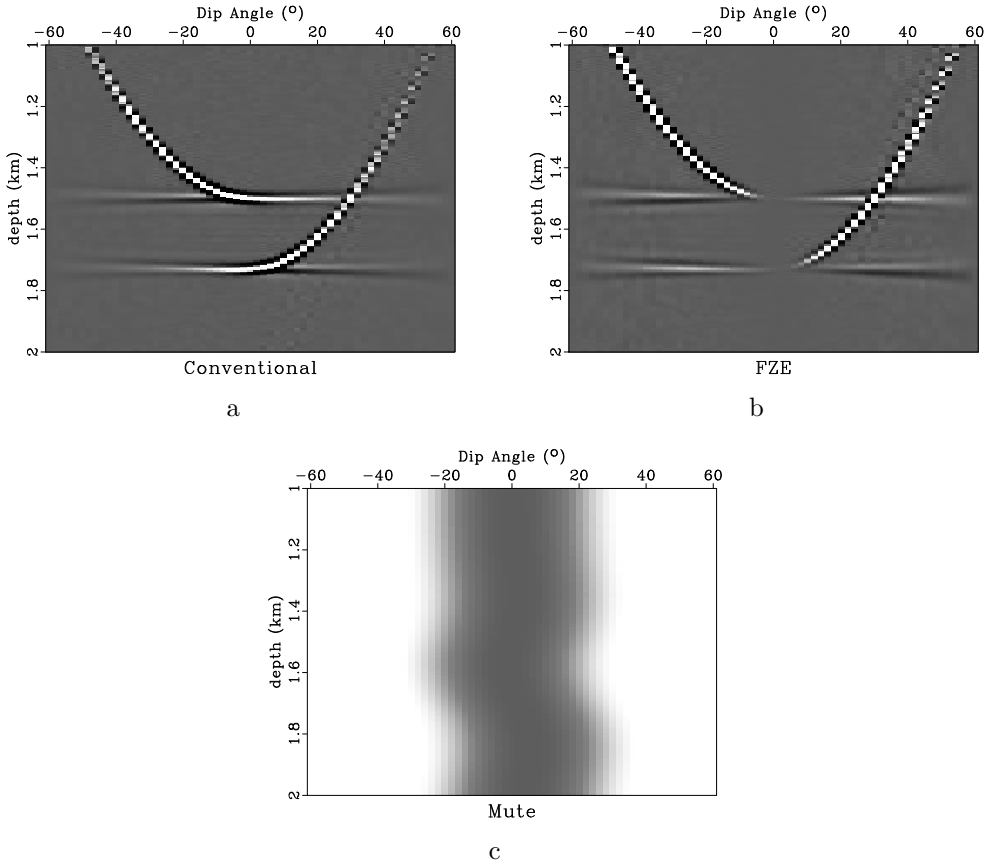

Figure 3.9: A series of DAGs from distance 3 km, the right side of the square graben: (a) DAG from conventional image, Figure 3.8a; (b) DAG from Figure 3.9a following Fresnel zone elimination; (c) Mute corresponding to the Fresnel zone in Figure 3.9a, centered at the dip calculated in Figure 3.8c. Masking the conventional DAG by this taper produces the Fresnel zone eliminated DAG. chap02/toy onemodel-dagT,onefz-eliminated,onetaper-smooth

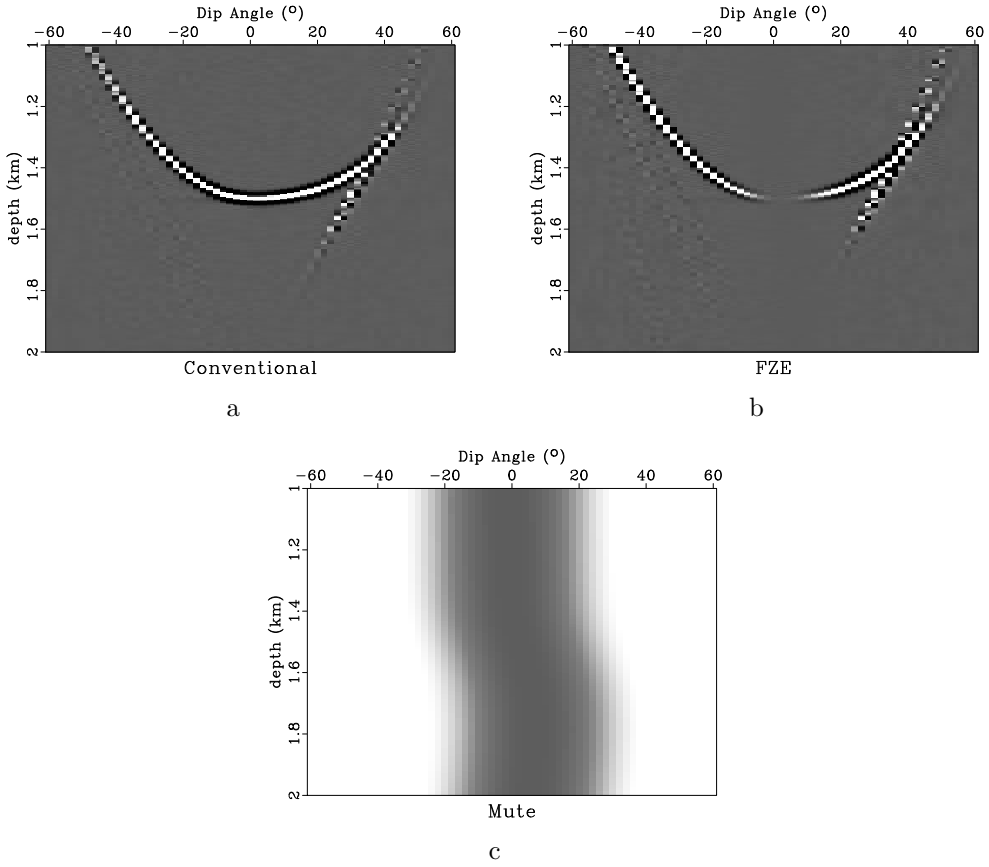

Figure 3.10: A series of DAGs from distance 1.5 km, the left edge of the curved graben: (a) DAG from conventional image, Figure 3.8a; (b) DAG from Figure 3.9a following Fresnel zone elimination; (c) Mute corresponding to the Fresnel zone in Figure 3.9a, centered at the dip calculated in Figure 3.8c. Masking the conventional DAG by this taper produces the Fresnel zone eliminated DAG. chap02/toy threemodel-dagT,threefz-eliminated,threetaper-smooth

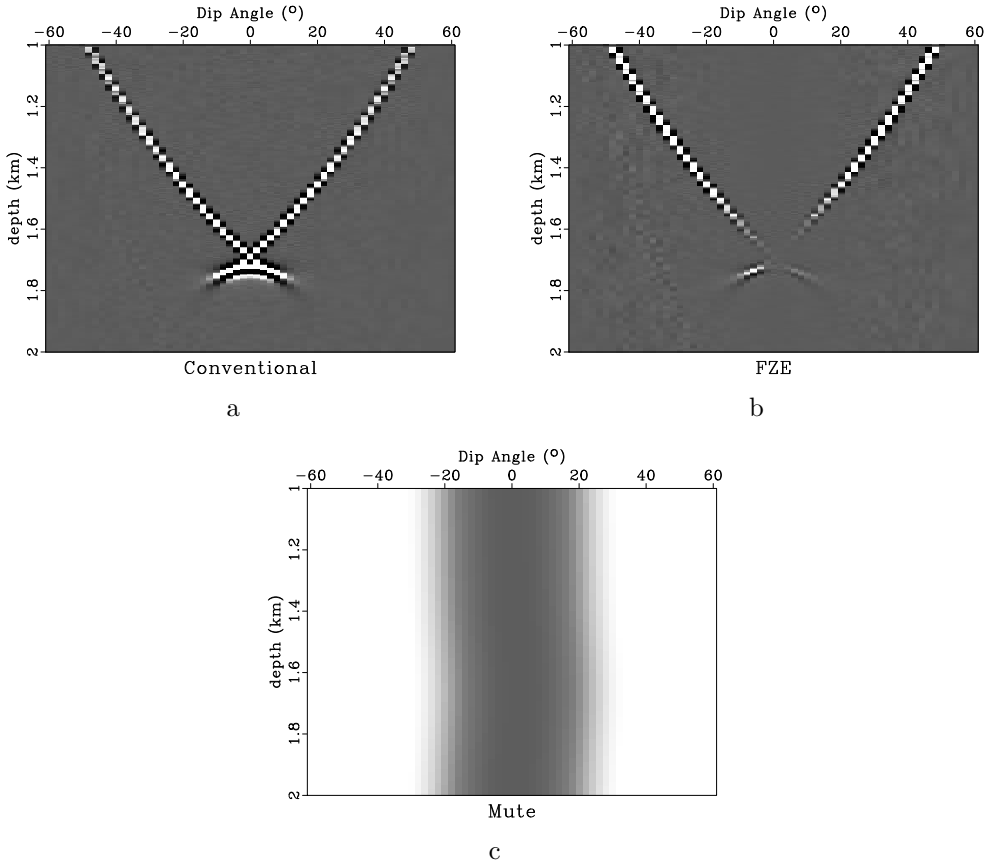

Figure 3.11: A series of DAGs from distance 1 km, the center of the curved graben: (a) DAG from conventional image, Figure 3.8a; (b) DAG from Figure 3.9a following Fresnel zone elimination; (c) Mute corresponding to the Fresnel zone in Figure 3.9a, centered at the dip calculated in Figure 3.8c. Masking the conventional DAG by this taper produces the Fresnel zone eliminated DAG. chap02/toy twomodel-dagT,twofz-eliminated,twotaper-smooth

This method successfully isolates the diffraction events at the corners of the square graben but fails to capture diffractions at the corner and base of the curved graben, as is visible in Figure 3.8b. Examining the angle-gathers provides insight into why this occurs. Examining the muted angle gather at distance 3 km, the right edge of the square graben, Figure 3.9b, notice that the mask only covers the stationary points of the upward bending reflections. Diffraction energy is spread over a large number of slopes, so the mute at the Fresnel zone does not destroy a large amount of it. Thus, after stacking, the diffractions remain.

Figure 3.10b, containing a Fresnel zone eliminated DAG from distance 1.5 km, the right edge of the curved graben, illustrates why the diffraction at the corners of the curved graben do not appear in Figure 3.8b's diffraction image. Because the diffraction at this depth is not an edge effect, but rather caused by the large curvature of the reflector, the diffraction is more confined in slope than in Figure 3.9b. This means that when a mute is applied it removes the diffraction energy along with the stationary point of the reflection. Thus, after stacking, the diffraction does not appear.

The limitation of Fresnel zone elimination for extracting diffractions caused by large curvature is also evident at the pseudo-diffraction at the bottom of the curved graben, whose angle-gather is shown in Figure 3.10b. Applying the Fresnel zone angle gather masks out the stationary portions of the pseudo-diffraction, so as with the reflections, it does not appear after stacking.

Examining Figure 3.8b, we can notice that Kirchhoff artifacts primarily paralleling reflectors are not removed by the method. These artifacts are also present in the conventional image, Figure 3.8a, but the high amplitude of the reflectors makes

them less visible. When compared to lower energy diffractions the artifacts become more apparent. These artifacts are more visible because all reflection energy has been effectively removed from the image.

PARTIAL-IMAGE PLANE-WAVE DESTRUCTION

Angle-migration can output a set of dip-angle gathers (Xu et al., 2001). Constant-dip-angle traces constitute a set of partial-images – seismic images of the subsurface obtained after migration using a single dip angle. Stacking these partial-images over dip-angle creates an image (Klokov and Fomel, 2012, 2013b). In the angle migrated partial-image domain reflection events appear planar and diffraction events have a hyperbolic character, similar to their appearance in un-migrated common-offset data, as illustrated in Figure 3.14a (Klokov and Fomel, 2013a). In this section, I propose a method for diffraction extraction that uses this discrepancy to predict and remove reflection events by modifying the workflow for data-domain plane-wave destruction (DD-PWD) so it operates in the partial-image domain (PI-PWD).

I propose that difficulties associated with separating diffractions and reflections in regions with complex geometries can be overcome by utilizing plane-wave destruction in constant-dip partial-images. Destroying reflections in angle-migrated partial-images by stationary image slope and stacking over dip angle produces a diffraction image. This method may create diffraction images containing less remnant reflection energy than plane-wave destruction in the data-domain. The extra dip-angle dimension associated with partial-image plane-wave destruction makes the method significantly more expensive than data-domain plane-wave destruction, and thus best suited for regions with complex geometries.

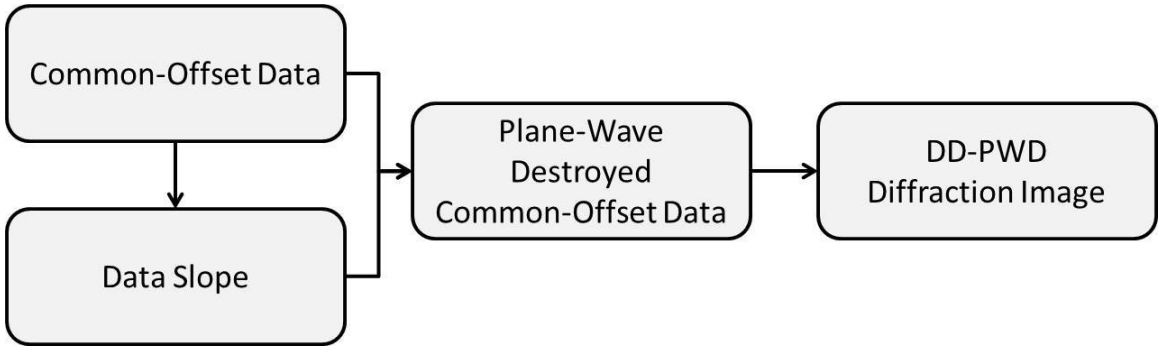

a

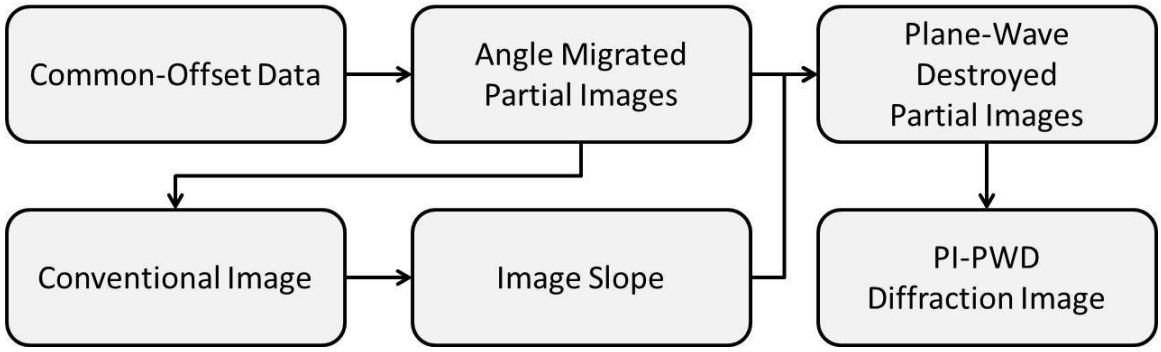

b

Figure 3.12: Diffraction imaging workflows for: (a) data-domain plane-wave destruction; (b) partial-image plane-wave destruction. chap02/. DD-PWD,PI-PWD4

The conventional workflow for DD-PWD (Fomel et al., 2007) is illustrated in Figure 3.12a. Dominant slope is estimated from common-offset data using PWD filters. Reflections conforming with that slope are removed, leaving plane-wave destroyed common-offset data, which contains diffraction events. These PWD data are migrated, providing a DD-PWD diffraction image.

I modify DD-PWD's workflow for application in the angle migrated partial-image domain. The modified workflow is shown in Figure 3.12b. Angle migration generates a set of constant-dip-angle partial-images, which are stacked to generate a conventional image. Reflectors have different slopes in partial-images, but only partial-image reflectors featuring image slope are constructive on stacking. Reflectors with other slopes interfere destructively and can be safely ignored. Therefore, destroying partial-image reflections by stationary slope will remove reflections from the stacked image.

Image slope is calculated with PWD filters, and plane-wave destruction is applied to the set of constant-dip partial-images. Plane-wave destruction removes dominant reflection events from the partial-images and leaves diffraction events. Stacking plane-wave-destroyed partial-images produces a PI-PWD diffraction image.

Calculating PWD slope from the migrated image provides a benefit to PI-PWD over DD-PWD. This is because one of the requirements of PWD filters is continuously variable slope, and when that requirement is not fulfilled the filters may encounter singularity points. As I will illustrate in the following examples, migration of seismic data from regions with complex geometry removes the singularity points where slope is not continuously variable, enabling plane-wave destruction filters to better predict slope and destroy reflection energy.

Illustration of Partial-Image Plane-Wave Destruction

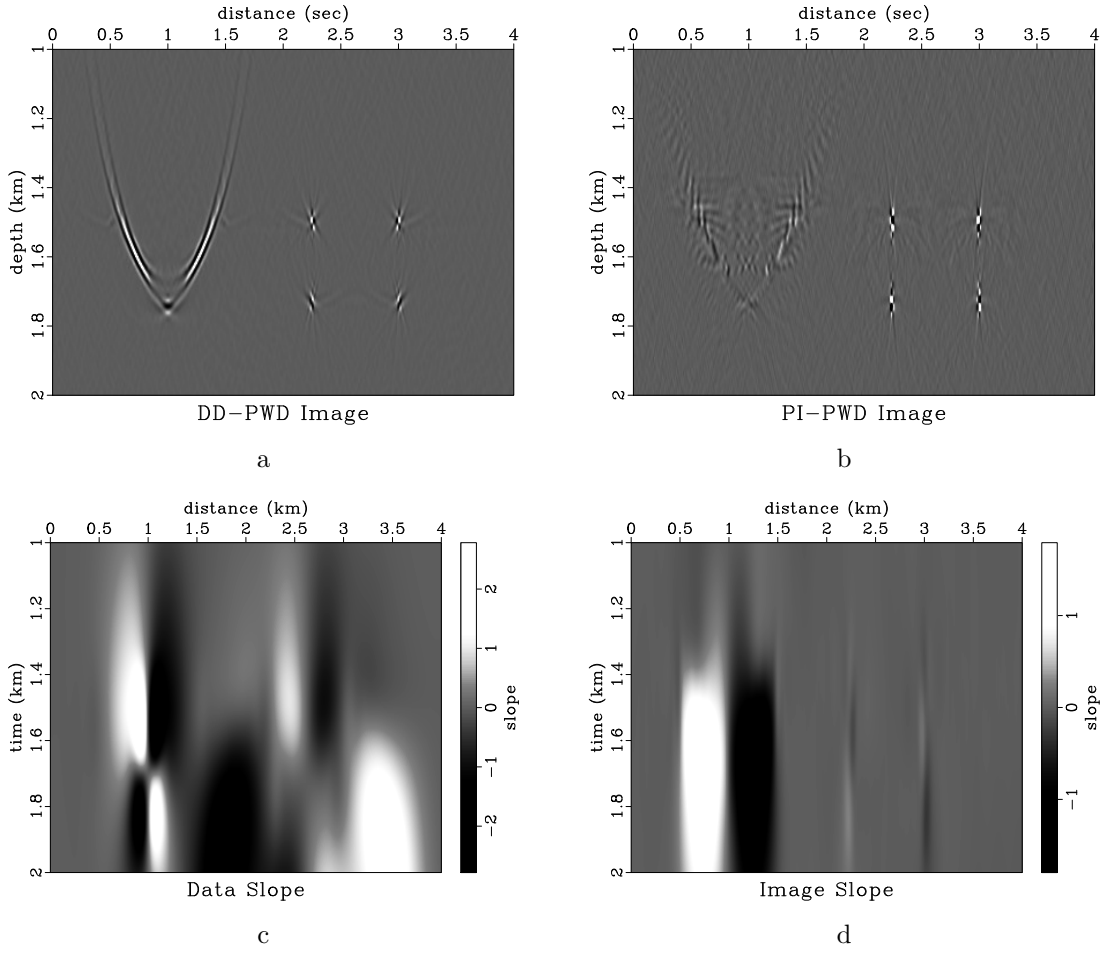

Figure 3.13: (a) data-domain plane-wave destruction image; (b) partial-image plane-wave destruction image (c) data slope calculated from Figure 3.1b; (d) image slope calculated from Figure 3.3a. chap02/pipwd smsu-image,i-pwd-image,slope,img-slope

I demonstrate partial-image plane-wave destruction and compare it to data-domain plane-wave destruction on the synthetic toy model from the previous section. Zero-offset seismic data are modeled, Figure 3.1b and used as the input for both workflows.

The DD-PWD workflow begins by estimating zero-offset data slope, Fig-

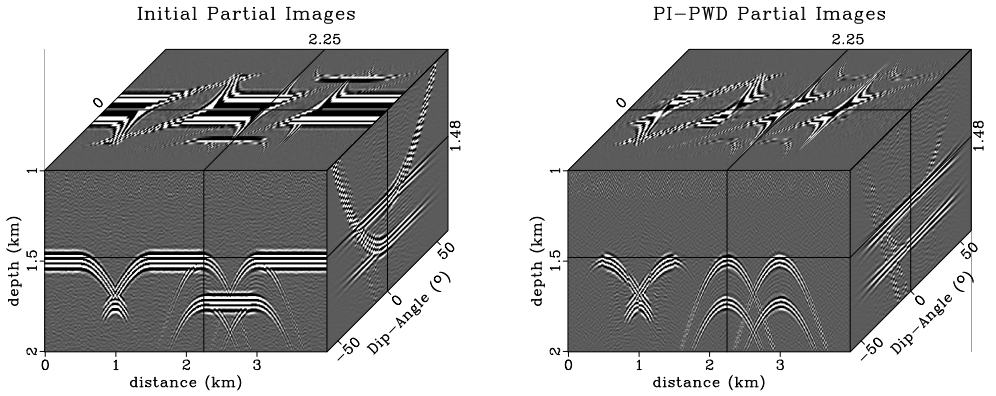

Figure 3.14: Angle migrated partial-images for constant-dip-angle $\alpha = 0°$ for: (a) conventional image, stacking produces Figure 3.3a; (b) partial-image plane-wave destruction diffraction image, stacking produces Figure 3.13b. chap02/pipwd pi,dpi

ure 3.13c, and removing planar features with local slope, providing a set of unmigrated diffraction events, Figure 3.2b. Plane-wave destroyed data are angle migrated forming a set of constant-dip-angle partial-images, which are stacked over dip-angle to produce a DD-PWD diffraction image, Figure 3.3b.

The PI-PWD workflow begins by angle-migrating zero-offset data, Figure 3.1b, to generate a set of constant-dip-angle partial-images, Figure 3.14a. These partial-images are stacked over dip-angle to generate the conventional image, Figure 3.3a. Image slope is calculated, Figure 3.13d, and Figure 3.14a's partial-images are plane-wave destroyed by that slope, removing reflections and leaving hyperbolic diffractions, visible in Figure 3.14b's partial-images. Stacking partial-images over dip-angle provides a PI-PWD diffraction image, Figure 3.13b.

Comparing the data slope (Figure 3.13c) with the image slope (Figure 3.13d), we can notice that the oscillations in data slope near the "bow tie" event centered below 1 km at 1.7 s time are not present in image slope. Image slope varies smoothly

through the curved graben, leading to a more stable plane-wave destruction capable of generating a diffraction image without the elliptic artifact of remnant reflection energy.

EFFECTS OF MIGRATION VELOCITY

In the real seismic reflection experiment,the exact migration velocity is unknown. As diffractions are migrated their downward pointing hyperbolas collapse into points when the correct migration velocity is used and then turn to upward pointing hyperbolas when over-migrated with too high of a migration velocity (Fomel, 2003b). In the dip-angle gather domain diffraction events curve upward when under-migrated, are flat when correct migration velocity is used, and then curve downward when over-migrated (Audebert et al., 2002; Landa et al., 2008; Klokov and Fomel, 2012). Data-domain plane-wave destruction separates diffraction energy prior to migration, so migration velocity does not affect its ability to operate. However, both Fresnel zone elimination and partial-image plane-wave destruction operate on migrated images, so an incorrect migration velocity may affect their ability to correctly function.

In order to test the dependence of each of the previously described diffraction extraction methods on migration velocity I repeat the toy model experiments shown in the previous sections while under-migrating data with $\frac{V_{mig}}{V} = 0.8$, correctly migrate them with $\frac{V_{mig}}{V} = 1$, and over-migrate them with $\frac{V_{mig}}{V} = 1.2$.

I begin by examining how conventional images are affected by migration velocity. Comparing the under-migrated conventional image, Figure 3.15a, the correctly migrated conventional image, Figure 3.16a, and the over-migrated conventional image, Figure 3.17a, the reflective portion of the image does not appear to change

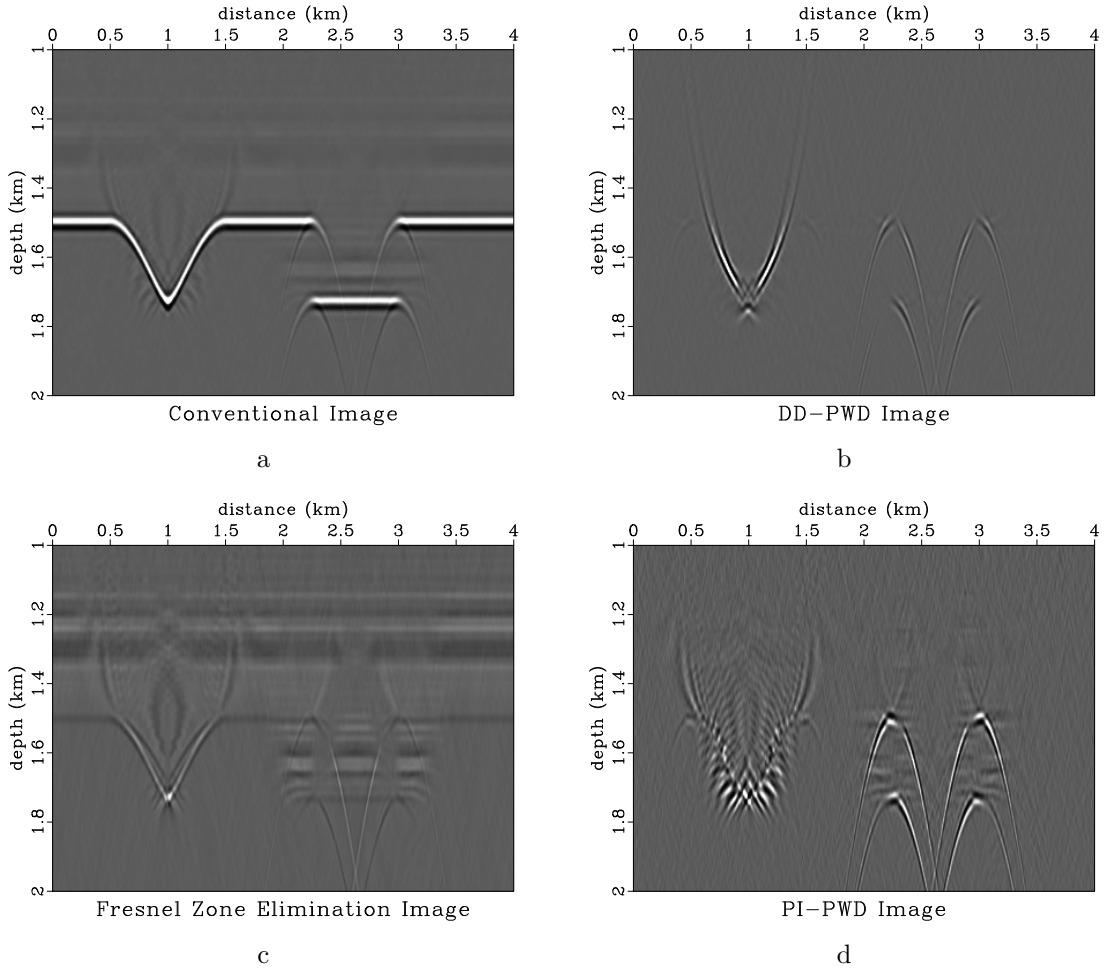

Figure 3.15: Under-migration with $\frac{V_{mig}}{V} = 0.8$ on a: (a) conventional image; (b) DD-PWD diffraction image; (c) Fresnel zone elimination diffraction image; (d) PI-PWD diffraction image. chap02/toy model-imageu2,smsu-imageu2,ad-imageu,i-pwd-imageu0

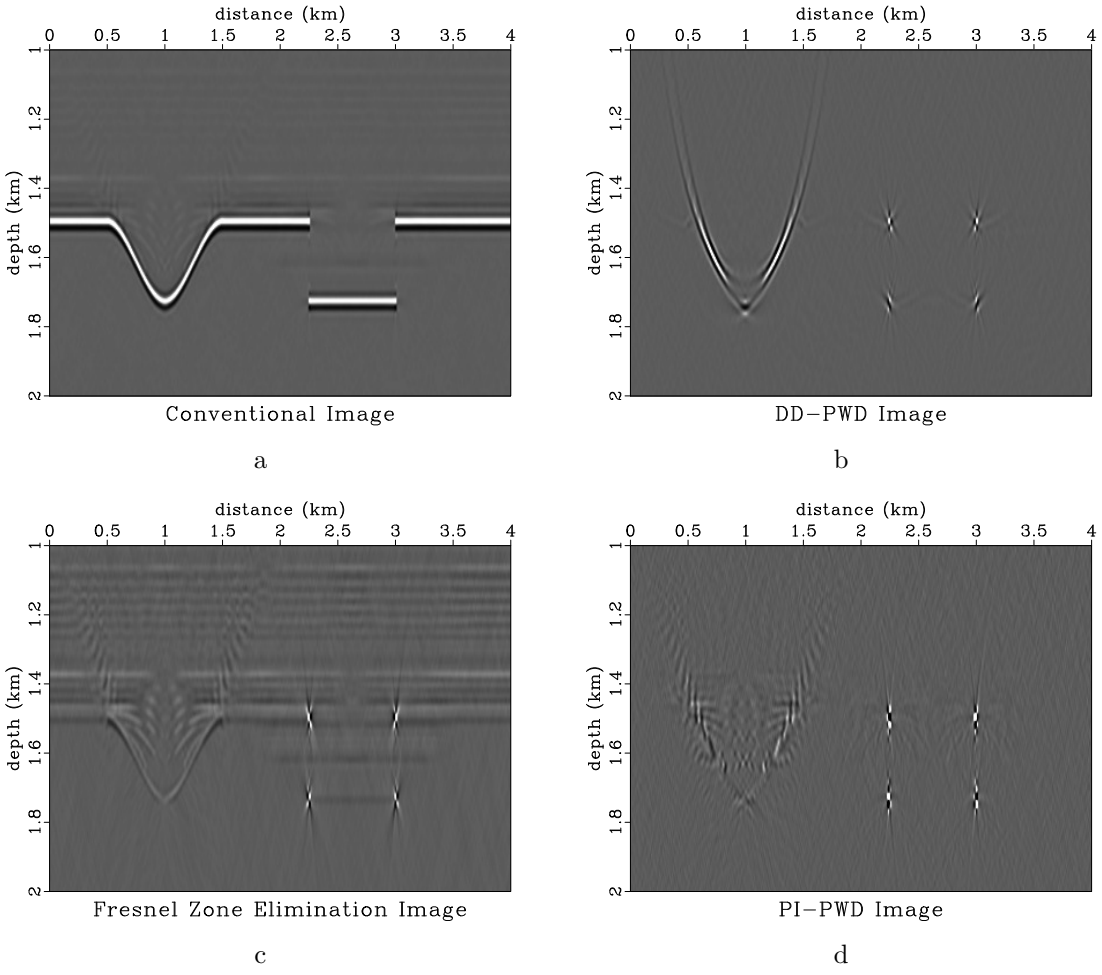

Figure 3.16: Correct migration with $\frac{V_{mig}}{V} = 1$ on a: (a) conventional image; (b) PI-PWD diffraction image; (c) Fresnel zone elimination diffraction image; (d) PI-PWD diffraction image. chap02/toy model-image2,smsu-image2,ad-image,i-pwd-image0

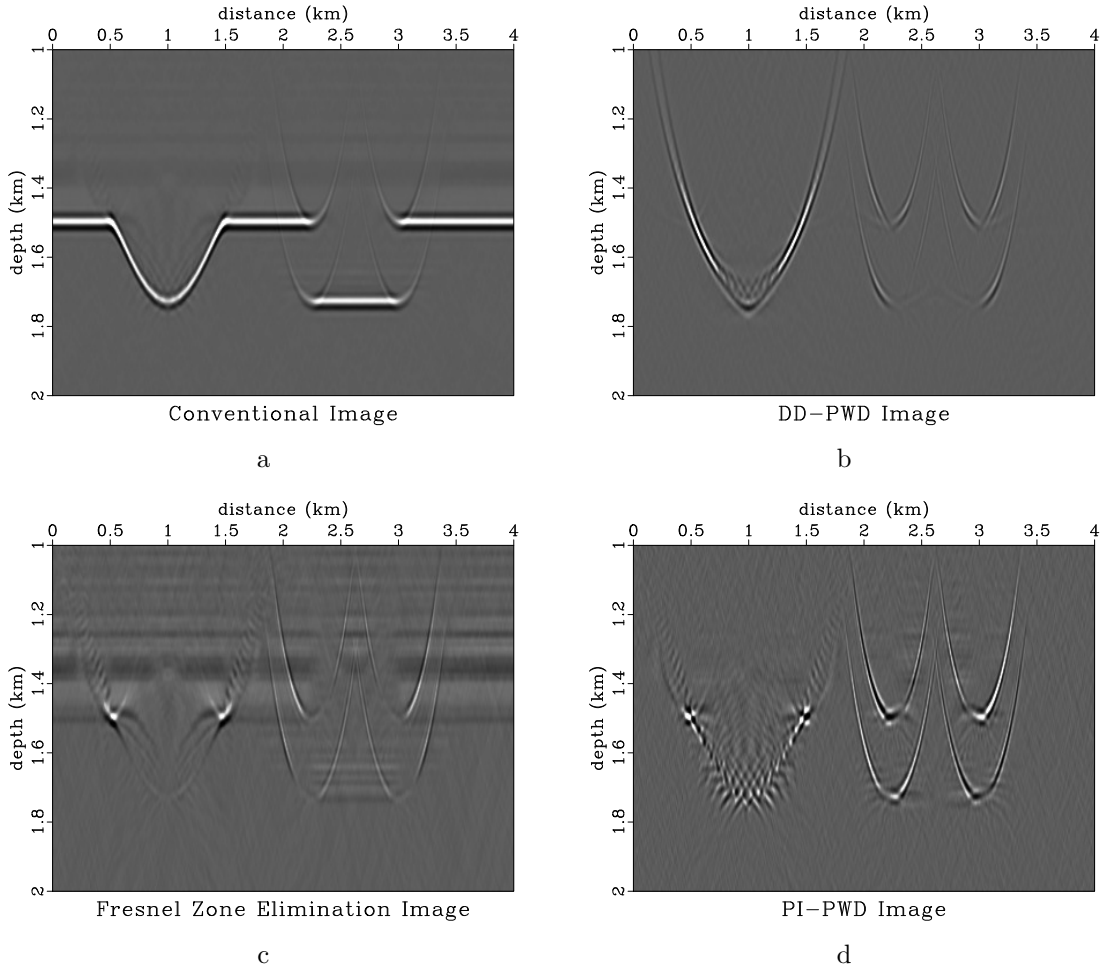

Figure 3.17: Over-migration with $\frac{V_{mig}}{V} = 1.2$ on a: (a) conventional image; (b) DD-PWD diffraction image; (c) Fresnel zone elimination diffraction image; (d) PI-PWD diffraction image. chap02/toy model-imageo2,smsu-imageo2,ad-imageo,i-pwd-imageo0

significantly when the migration velocity is varied. Reflectors are placed at a slightly greater depth in the under-migrated image and at slightly shallower depth in the over-migrated image. The largest difference in these images is visible in the diffractions at the edges of the reflector. The diffractions become hidden by the reflections when migrated with correct velocity. They appear hyperbolic downward when under-migrated, and hyperbolic upward when over-migrated. Examiniing the conventional image DAGs from a distance of 3 km, visible in the left panels of Figures 3.18a-3.18c, notice that the reflection energy within the DAG curves upward for all migration cases. The weakly visible diffraction energy component curves upward when under-migrated, is flat when correctly migrated, and curves downward when over-migrated.

Comparing the appearance of the data-domain plane-wave destruction images shows a clearer view of the effects of migration velocity on diffractions. Because DD-PWD operates in the un-migrated data-domain, migration velocity does not affect the diffraction extraction process, and thus this experiment shows how under and over-migrated diffractions ought to appear. Diffractions are distinctly hyperbolic downward in the under-migrated DD-PWD image, Figure 3.15b, collapse to points in the correctly migrated image, Figure 3.16b, and appear hyperbolic upward in the over-migrated diffraction image, Figure 3.17b. Examining an individual DD-PWD DAG for the three migration cases, the second from the left panel in Figures 3.18a-3.18c, provides insight into how diffraction energy may appear in the angle-gather domain. When diffractions are under migrated they curve upward in the DAG domain. When correctly migrated they appear flat. When over-migrated they point downward.

The effectiveness of the post-migration diffraction extraction methods can be assessed by comparing the results of their images and angle gathers to see how well diffraction energy is isolated.

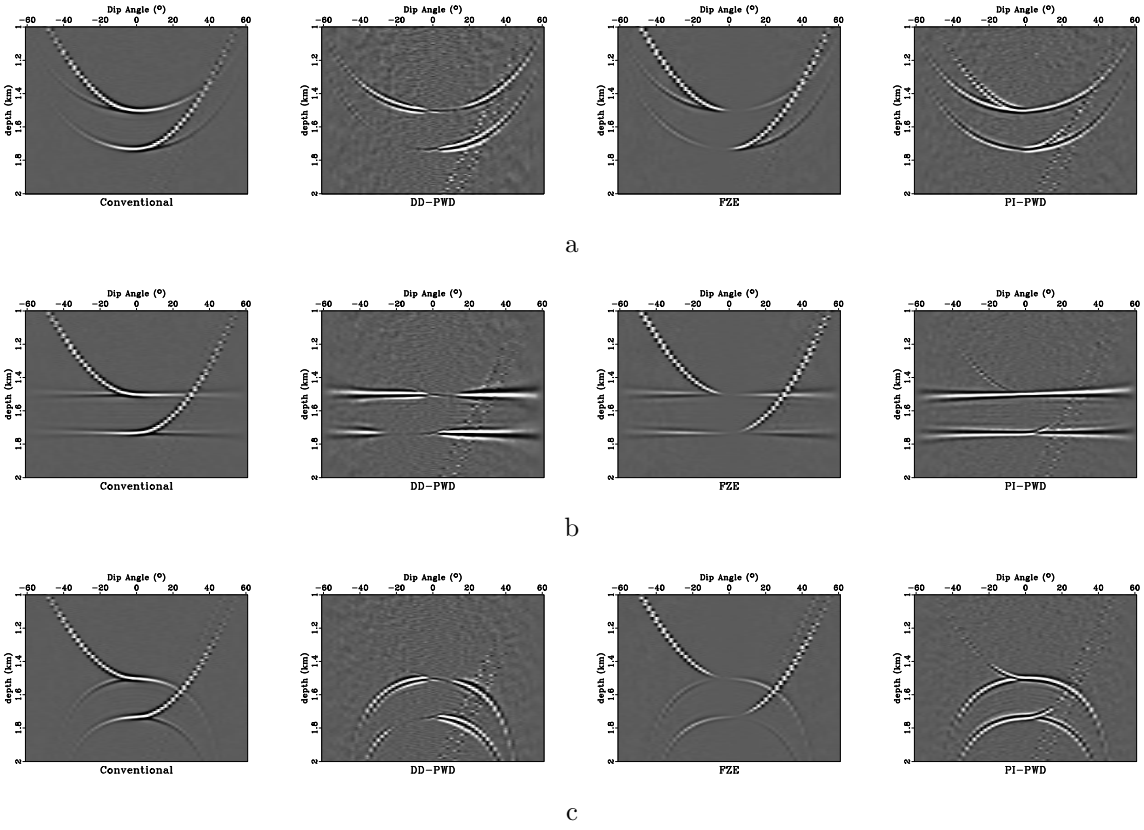

Figure 3.18: Comparison of the effects of migration velocity on a set of dip-angle gathers from distance 3 km for conventional imaging, DD-PWD diffraction image, Fresnel zone elimination, and PI-PWD diffraction image for:
(a) under-migration with $\frac{V_{mig}}{V} = 0.8$;
(b) correct migration with $\frac{V_{mig}}{V} = 1$;
(c) over-migration with $\frac{V_{mig}}{V} = 1.2$; chap02/toy dagsu,dags,dagso

Fresnel zone elimination has difficulty extracting diffractions migrated with incorrect velocity. Fresnel zone diffraction images are visible for under-migration in Figure 3.15c, correct migration in Figure 3.16c, and over-migration in Figure 3.17c. Examining the under and over migrated images, notice that very little diffraction energy from the square grabens is successfully isolated. Examining the Fresnel zone elimination DAGs, the third panel of Figures 3.18a-c, the reason for diffraction energy's attenuation is visible. When migrated with an incorrect velocity, diffractions are no longer flat, and thus are no longer stationary across all dip angles in the gather. This means that when central angles are muted to remove the stationary parts of reflections, the stationary portion of incorrectly migrated diffractions is muted as well.

PI-PWD appears very effective at isolating diffractions even when an incorrect migration velocity is used. PI-PWD diffraction images are visible for under-migrated in Figure 3.15d, correct migration in Figure 3.16d, and over-migration in Figure 3.17d. Because PI-PWD does not migrate a point of reflection energy into an ellipse, diffraction energy is more apparent than in the DD-PWD case. Under-migrated diffraction events point hyperbolically downward, correctly migrated events collapse, and over-migrated events point upward. Migration artifacts surrounding the curved graben which can be seen in the PI-PWD diffraction image's under and over-migrated cases are also apparent in the conventional under and over-migrated images upon close inspection.

Examining the DAGs, the rightmost images in Figures 3.18a-c show that PI-PWD successfully isolates the most diffraction energy in all cases. This is because even DD-PWD destroys diffraction energy conforming with data slope, removing a portion near the data slope. This is apparent as dimming of the diffraction events. PI-PWD does not have this effect, and diffraction events enjoy near constant amplitude

across all dip angles of the aperture.

FIELD DATA APPLICATION

I next apply data-domain plane-wave destruction (DD-PWD), Fresnel zone elimination (FZE), and partial-image plane-wave destruction (PI-PWD) to two Gulf of Mexico datasets, the first containg a series of faults and the second a salt dome (Claerbout, 2005; Fomel et al., 2007).

Fault Data Set

I begin with a field-data set from the Gulf of Mexico containing a series of faults, which cause diffractions. DMO stacked common offset data is visible in Figure 3.19a. PWD data slope is calculated, Figure 3.20a, and reflections conforming with local slope are removed, leaving data-domain plane-wave destruction data, Figure 3.19b. Conventional and diffraction data are Kirchhoff angle-migrated with wide aperture (60°) to create conventional and DD-PWD diffraction images, Figures 3.21a and 3.21b respectively.

To generate FZE and PI-PWD diffracton images I begin by calculating image slope from Figure 3.21a, visible in Figure 3.20b.

I convert image slope to image dip for FZE, generate a set of tapers, and mute out the Fresnel zones in the wide-angle migration, providing the FZE diffraction image, Figure 3.22a.

Destroying the full set of Kirchhoff migrated partial-images by the image slope provides the wide aperture PI-PWD diffraction image, Figure 3.22b.

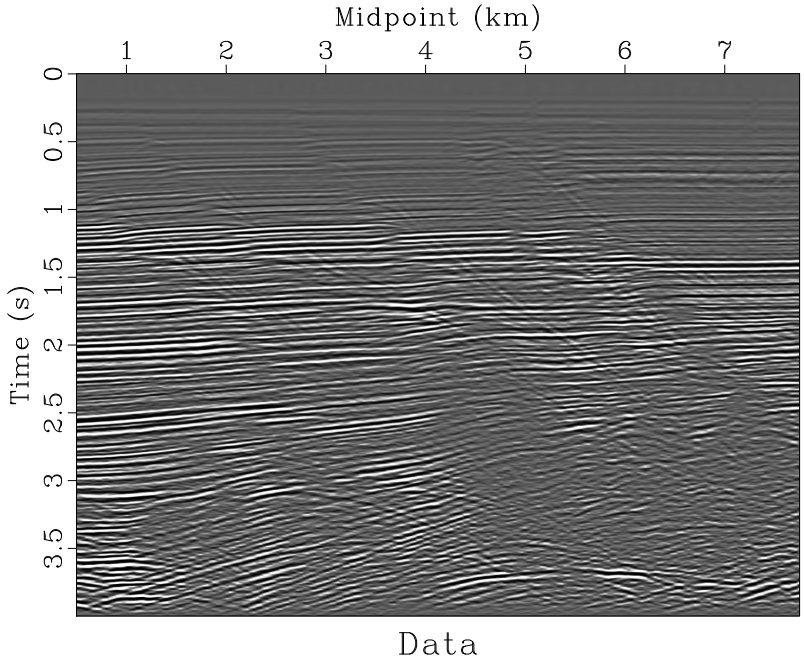

a

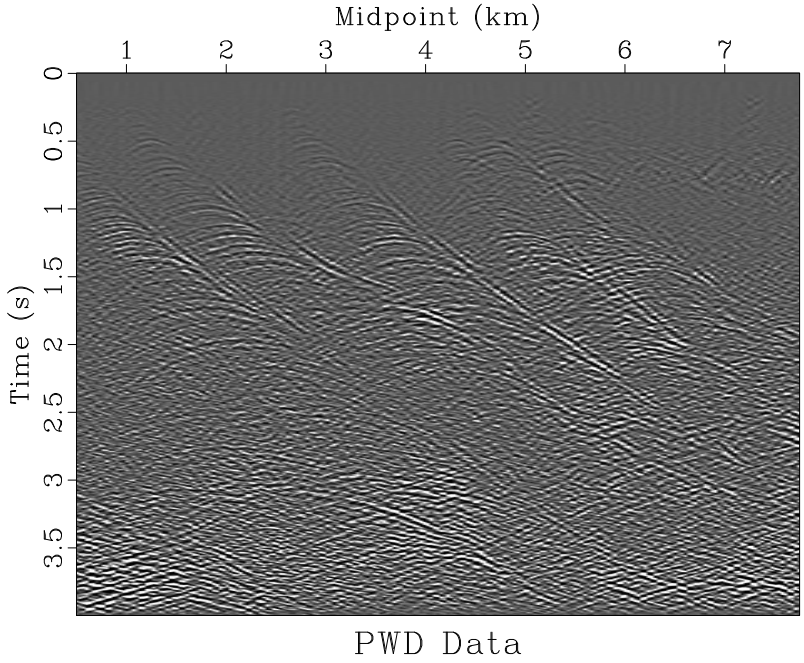

b

Figure 3.19: DMO stacked field-data from the Gulf of Mexico containing a series of faults (Fault field dataset): (a) conventional data; (b) data-domain PWD data chap02/fault bei-stk1,bei-pwd1

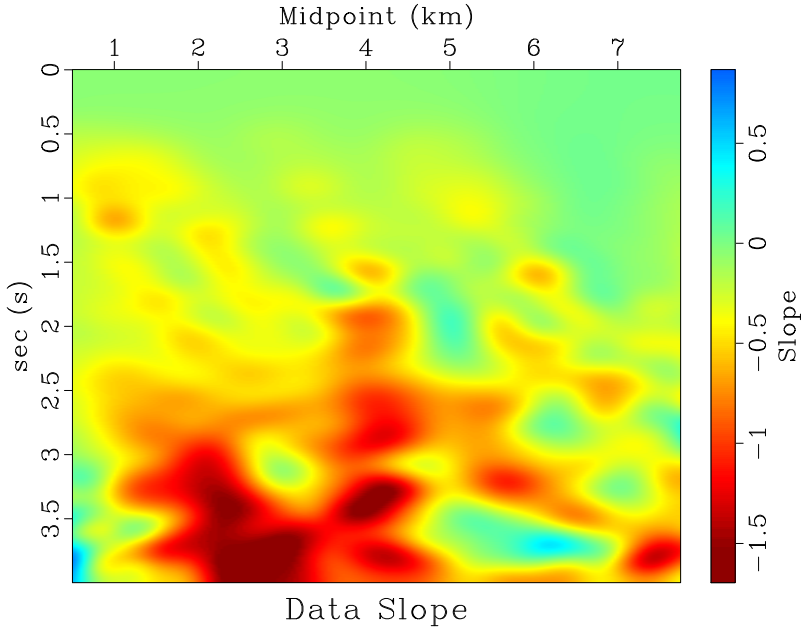

Data Slope

a

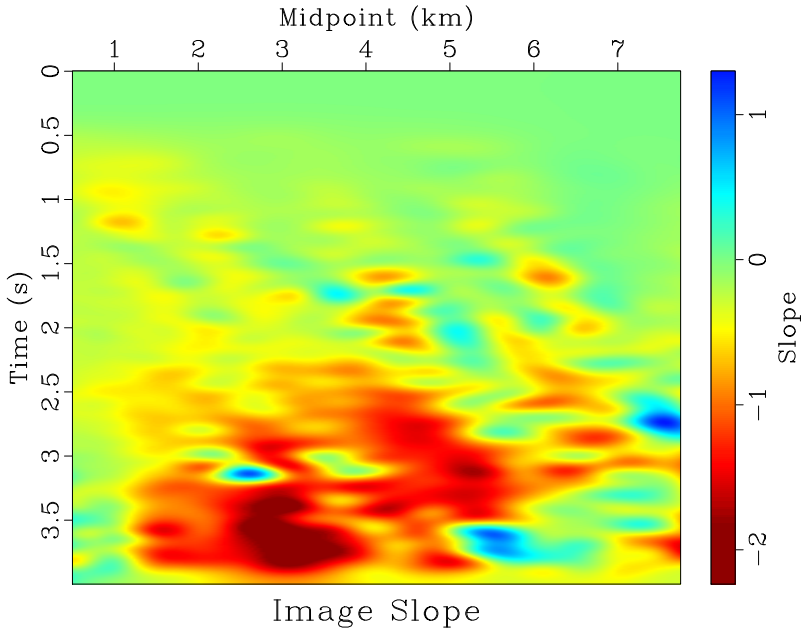

Image Slope

b

Figure 3.20: Fault field dataset slopes: (a) data slope for Figure 3.19a; (b) image slope for Figure 3.21a chap02/fault bei-stk2-slope,bei-img-slope

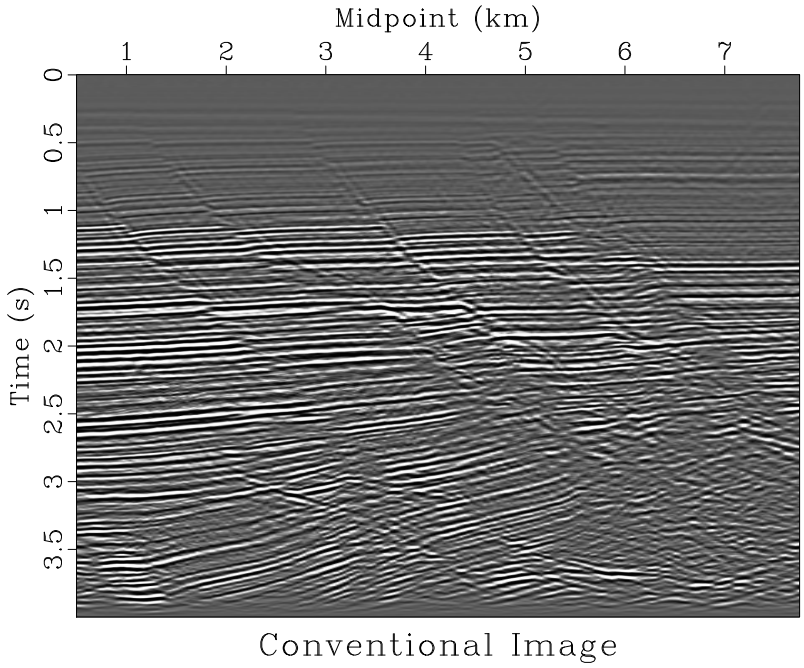

a

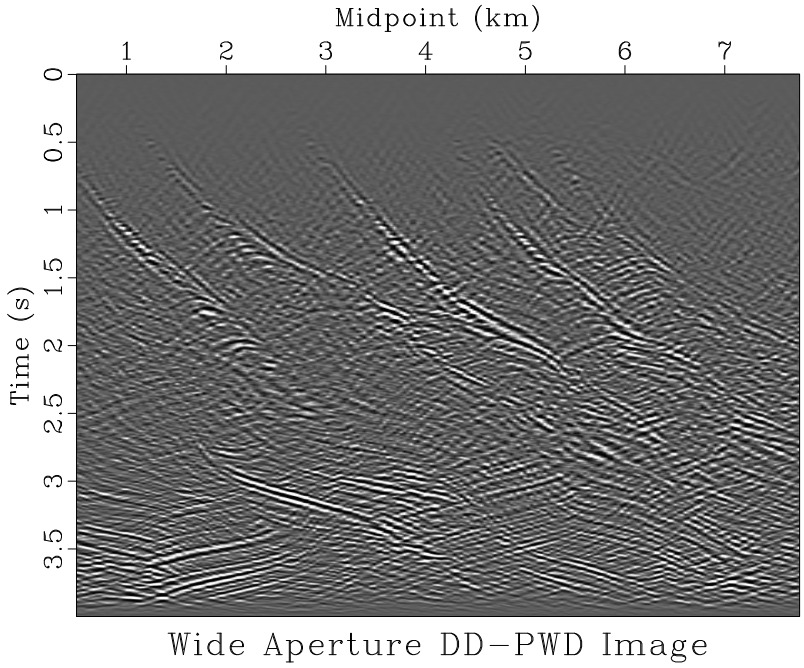

b

Figure 3.21: Fault field dataset wide-aperture (60°) Kirchoff angle-migrated images: (a) conventional; (b) diffraction chap02/fault bei-stk2-image,bei-pwd-image0

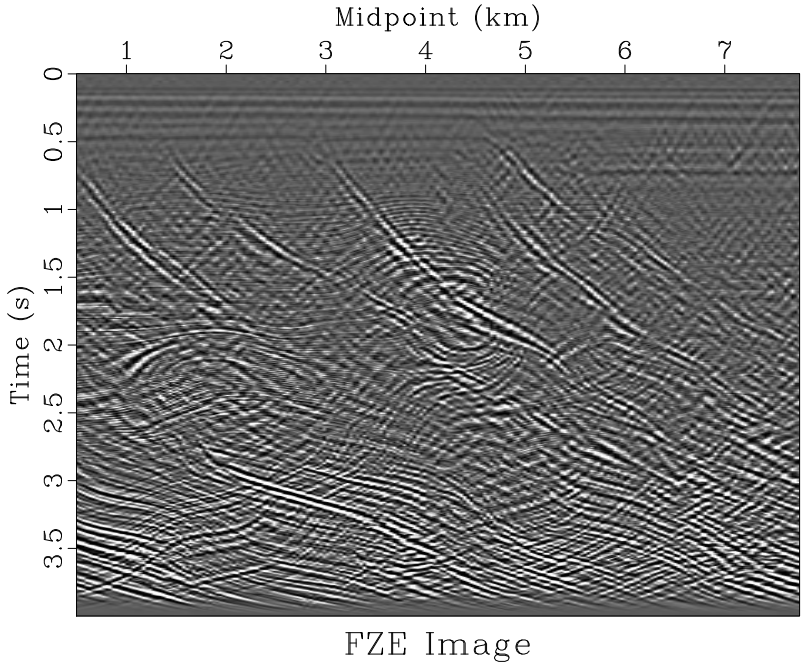

a

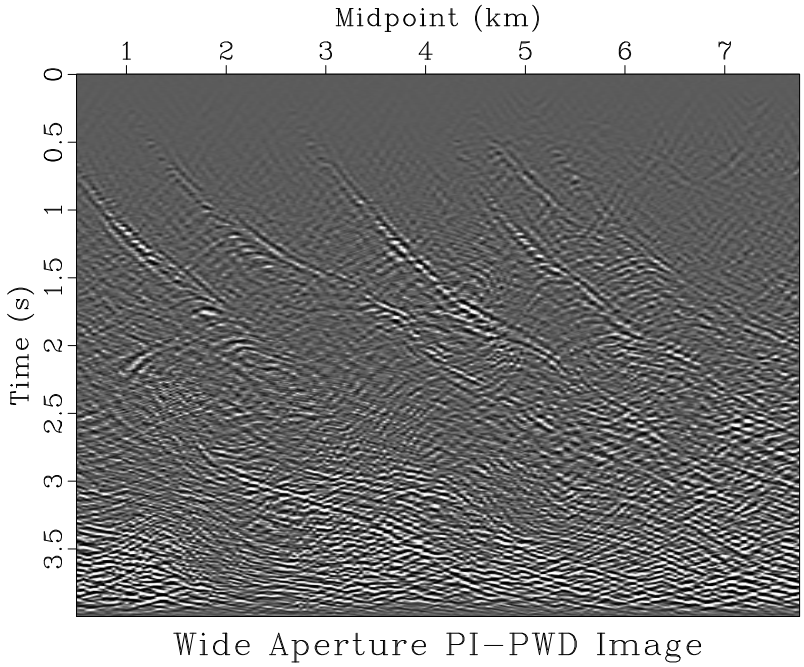

b

Figure 3.22: Fault field dataset wide-aperture migration (±60°) diffraction images: (a) Fresnel zone elimination; (b) partial-image plane-wave destruction. chap02/fault bei-ad-image,bei-i-pwd-image

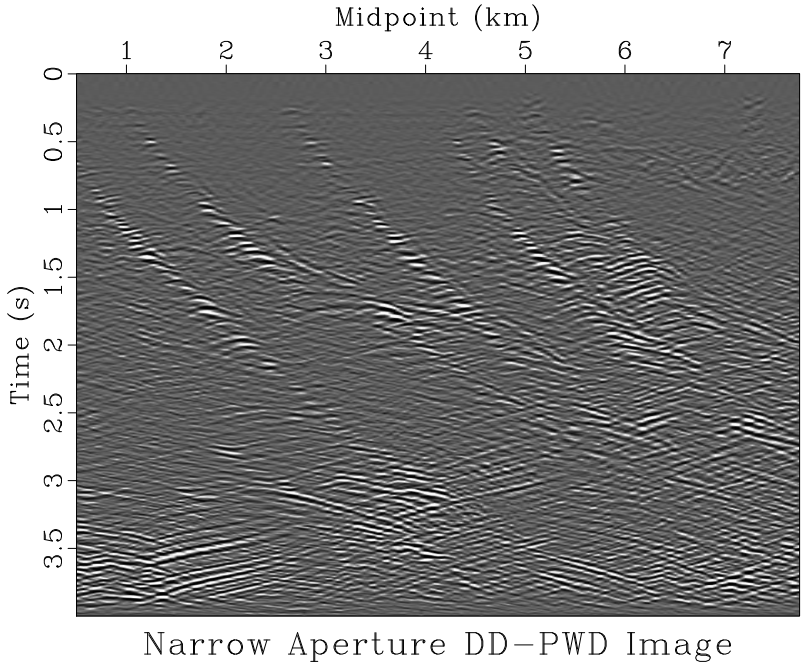

a

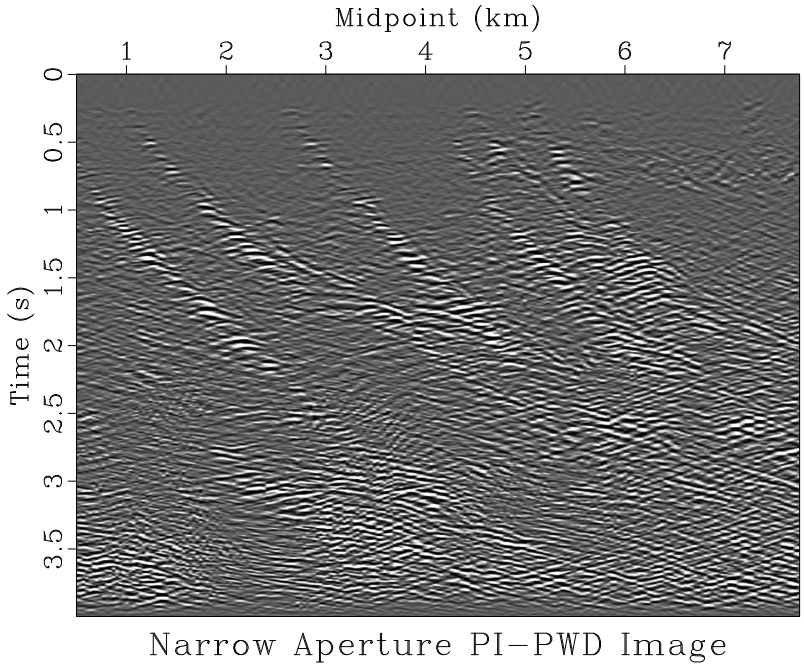

b

Figure 3.23: Fault field dataset narrow-aperture migration (±15°) diffraction images: (a) data-domain plane-wave destruction; (b) partial-image plane-wave destruction. chap02/fault bei-pwd-imagew,bei-i-pwd-imagew

I find that the wide aperture angle-migration, although necessary for generating a FZE diffraction image, reduces the signal to noise ratio of the diffraction image. By stacking only over narrow common-reflection angle gathers, up to $\pm 15^{\circ}$, superior diffraction images for both DD-PWD and PI-PWD methods can be created. The narrow-aperture DD-PWD diffraction image is visible in Figure 3.23a. The narrow-aperture PI-PWD diffraction image is visible in Figure 3.23b.

Fault Diffraction Image Discussion

DD-PWD appears to be best suited for diffraction imaging on this dataset. The superior diffraction images for DD-PWD and PI-PWD using narrow aperture indicate that the majority of diffraction energy is contained within $\pm 15^{\circ}$ in the common-reflection angle domain. When the stationary portions of reflections are masked with FZE, a mask with 15° width and an additional 15° transitional "grey area" was required. The majority of diffraction energy was contained within the Fresnel zone, and was removed along with the stationary portion of reflections. Thus, in the FZE diffraction image, Figure 3.22a, the prominent visible features are not actually diffractions, but rather the steeply dipping reflections off of the faults, are stationary at a different common-reflection angle than the more powerful reflections off of geologic strata, which affect the PWD slope output.

The narrow aperture DD-PWD (Figure 3.23a) and PI-PWD (Figure 3.23a) diffraction images are very similar. DD-PWD had a significantly lower computational cost than PI-PWD, since PI-PWD had to use the destruction operator on 30 partial-images, while DD-PWD only operated on zero-offset data. Because DD-PWD produced an equivalent image using less computational time, I conclude that it was best suited for diffraction extraction on this dataset.

Salt Dome Data Set

The second field-data set from the Gulf of Mexico contains reflections and diffractions from a salt dome. Stacked data is visible in Figure 3.24a. I calculate data slope (Figure 3.25a), and plane-wave destroy the data, leaving the set of data-domain plane-wave destruction diffraction events, shown in Figure 3.24b.

Complete and diffraction data are migrated using oriented velocity continuation, which will be further discussed in the next chapter. This method (OVC) decomposes data into slope, and migrates the decomposed data over a range of velocities. The oriented velocity continued slope gather corresponding to the correct migration velocity is selected, producing a set of gathers which are equivalent to Kirchhoff angle migration dip-angle gathers.

The complete image is visible in Figure 3.26a. The DD-PWD diffraction image is visible in Figure 3.26b. I calculate the image slope from Figure 3.26a to use in Fresnel zone elimination and partial-image plane-wave destruction. The slope field is visible in Figure 3.25b.

A set of Fresnel zone masks are constructed and applied to the OVC slope gathers. Muted gathers are stacked, providing the FZE diffraction image, Figure 3.27a.

Constant slope partial-images are plane wave destroyed by complete image slope (Figure 3.25b) and stacked to produce the PI-PWD diffraction image, visible in Figure 3.27b.

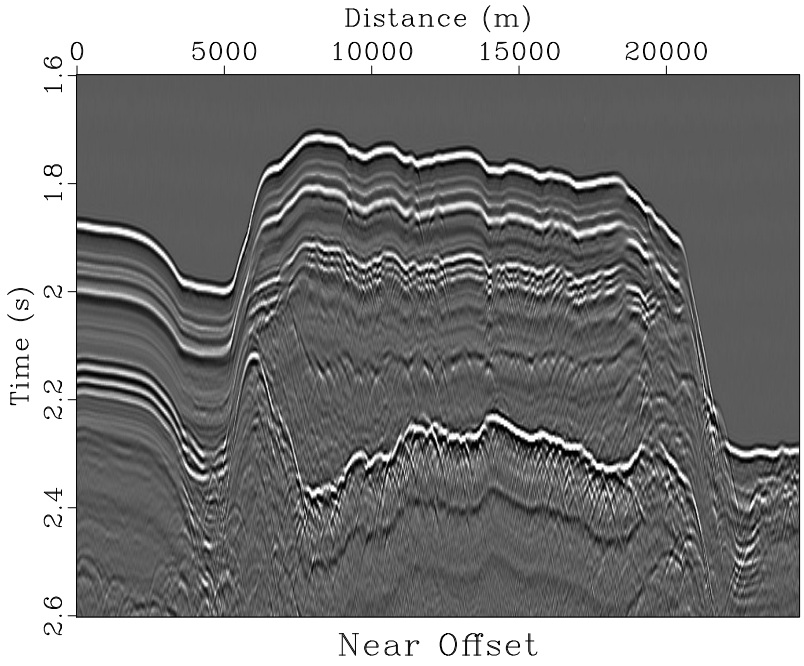

a

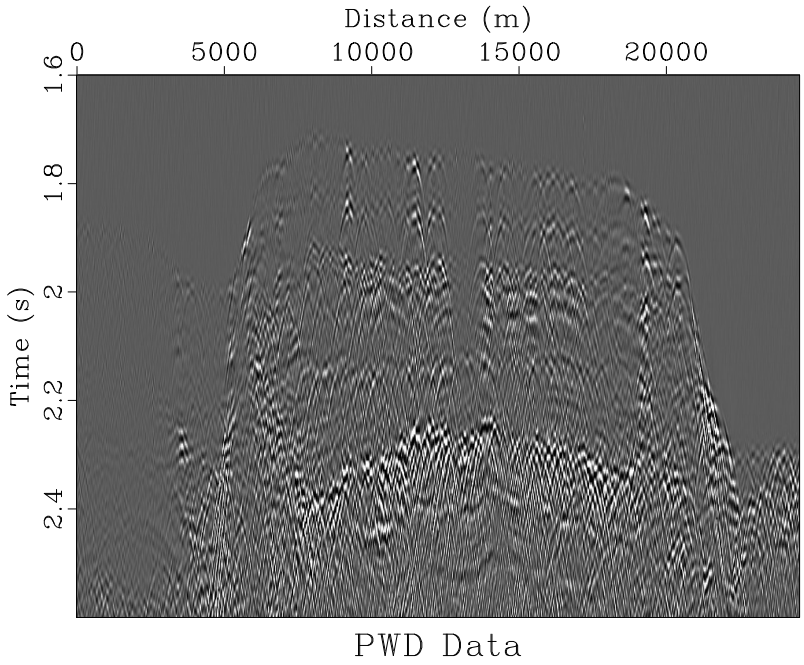

b

Figure 3.24: Stacked near-offset field-data from the Gulf of Mexico containing a salt dome (salt dome dataset): (a) conventional data; (b) data-domain PWD data chap02/gom gom,pwd2

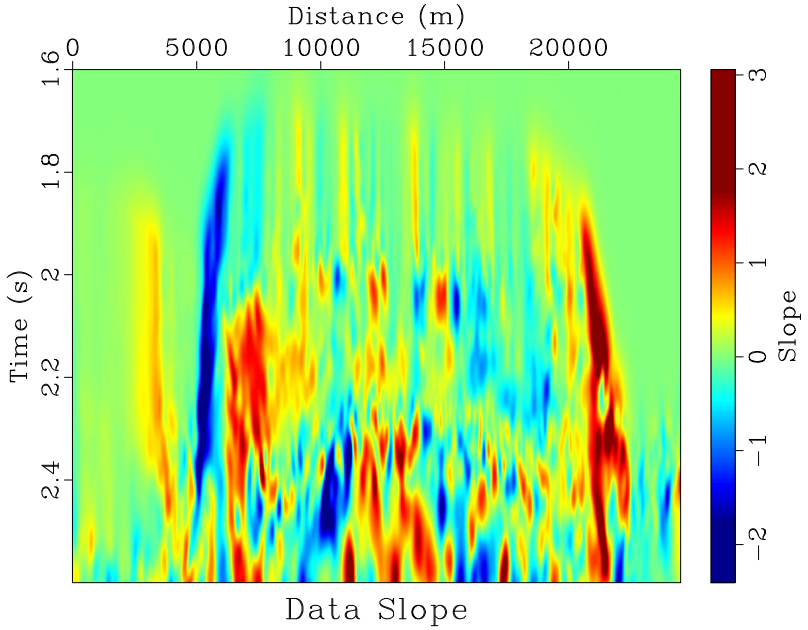

a

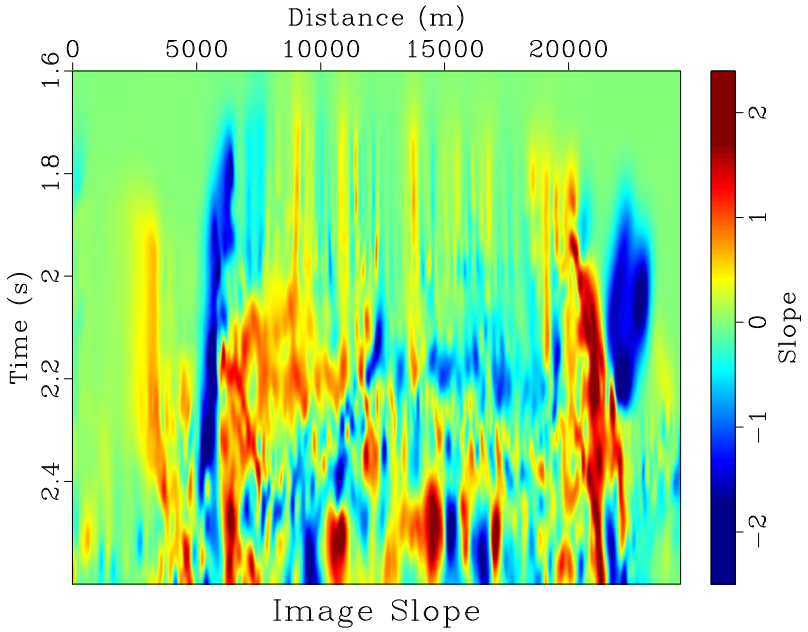

b

Figure 3.25: Salt dome dataset slopes: (a) data slope for Figure 3.24a; (b) image slope for Figure 3.26a chap02/gom dip2,gom-image-slope

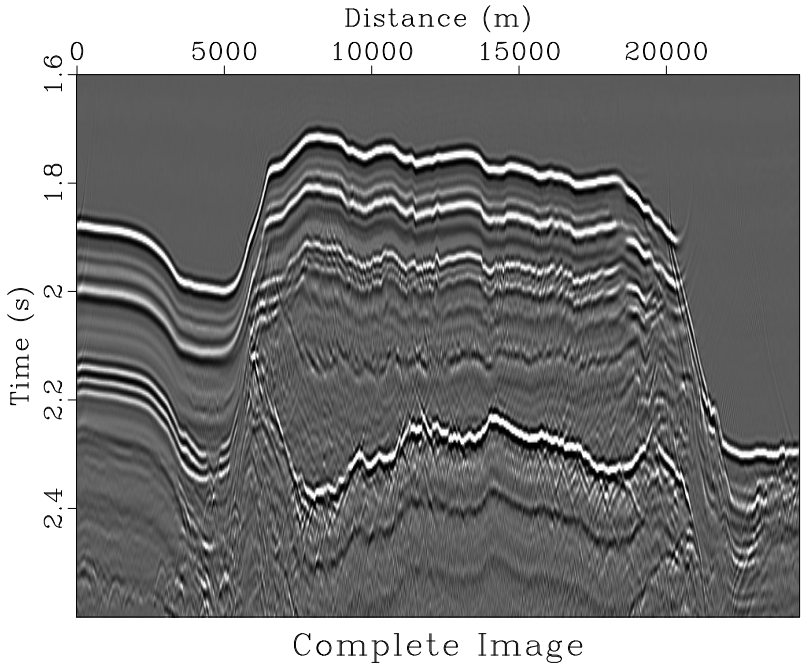

a

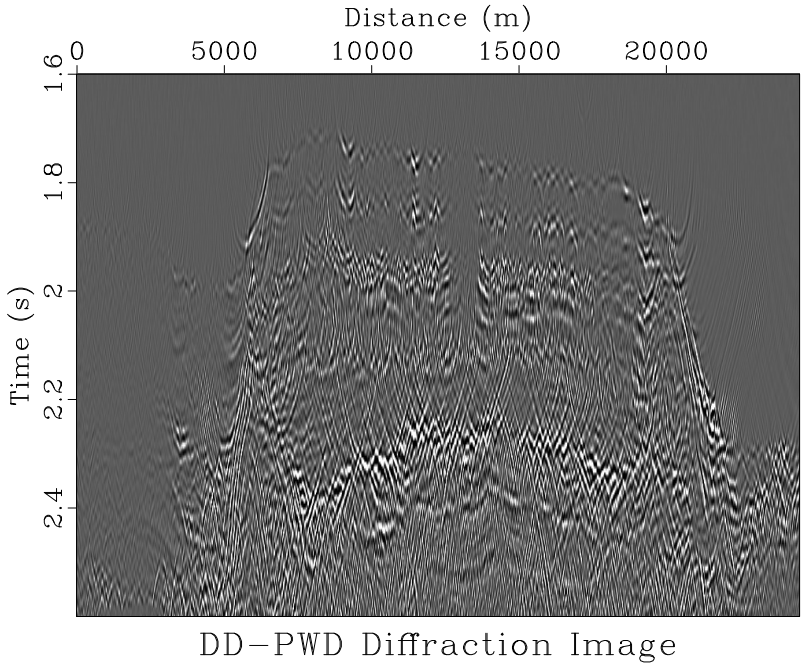

b

Figure 3.26: Salt dome dataset OVC migrated: (a) complete image; (b) data-domain plane-wave destruction diffraction image. chap02/gom gom-image,pwd2-image

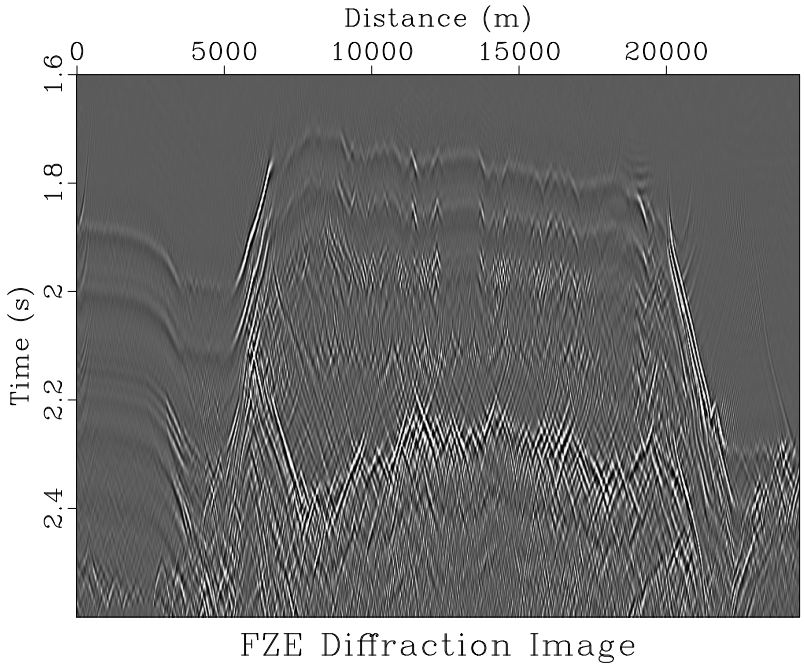

a

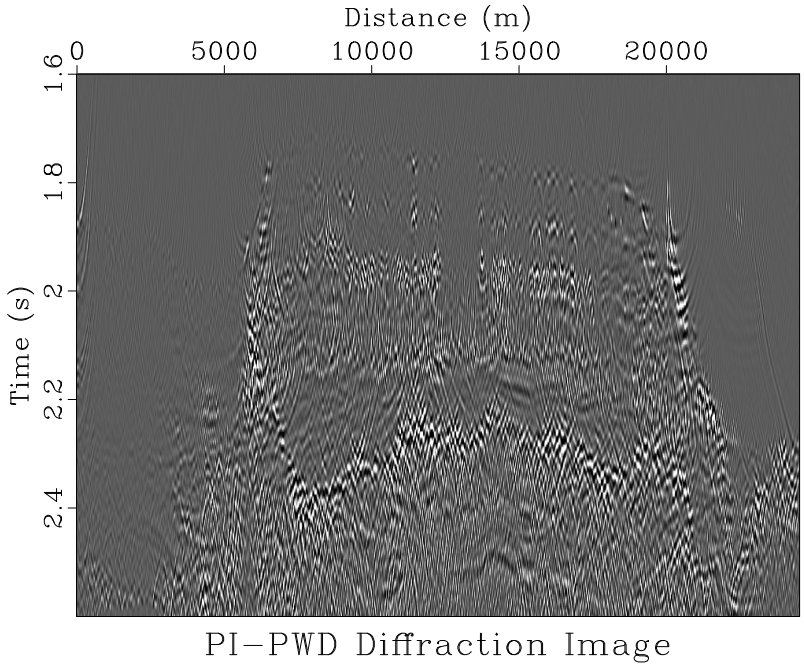

b

Figure 3.27: Salt dome dataset OVC migrated: (a) Fresnel zone elimination diffraction image; (b) partial-image plane-wave destruction diffraction image. chap02/gom gom-image-fze,gom-image-pwd

Salt Dome Diffraction Image Discussion

Data-domain plane-wave destruction produces the best diffraction image in the salt dome data set, and Fresnel zone elimination is the least effective at creating a diffraction image.

Examining the FZE diffraction image, Figure 3.27a, notice that diffractions are not very prominent, and that low frequency reflections are still present in the data despite high-pass filtering which attenuates signal below 10 Hz. Increasing the mask width was unable to mask these reflections without also removing all diffraction information.

Data-domain plane-wave destruction produces a reasonable diffraction image, Figure 3.24b. Diffraction energy is well isolated and clearly evident in the image. Little reflection energy is present in the image.

Partial-image plane-wave destruction produces the diffraction image (Figure 3.27b) with the most reflection energy removed. Planar features evident in the DD-PWD image (Figure 3.24b) near Time 2.4 sec between Distance 10000 m and 18000 m have been removed, as have planar features near Time 2 sec appearing intermittently between Distance 9000 m. Additionally, some remnant reflections present at the edges of the graben to the left of the salt dome DD-PWD image are removed in the PI-PWD image. A small amount of remnant reflection energy remains in the PI-PWD image, but less so than in the DD-PWD image.

METHOD COMPARISON

In my experiments with a toy model and two field datasets, data-domain plane wave destruction, Fresnel zone elimination, and partial-image plane-wave destruction all

were able to remove reflection energy. PWD methods left comparatively more diffraction energy in the resulting image, and better preserved diffractions, which are often isolated to the muted Fresnel zone. This feature made PWD methods of extraction more effective for use in the field data sets.

In the toy example, DD-PWD was able to isolate diffractions from sharp corners but left a large migration artifact. This was because PWD failed to remove a single point at the base of the curved graben lacking continuously variable slope. When this single point was migrated it became a circle. FZE was able to suppress reflections without leaving singularity points but it also removed a significant portion of diffraction energy and left Kirchhoff artifacts present in the image. PI-PWD was able to best isolate diffractions via stationary phase elimination by plane-wave destruction. It left a large quantity of diffraction energy, similar to DD-PWD. Because dip was calculated in the migrated image domain, singularity points were removed from the dip calculation enabling a more successful plane-wave destruction. This more stable dip calculation is evident comparing the data slope (Figure 3.13c), and the image slope (Figure 3.13d). Oscillations in slope value present at the base of the curved graven in the data near distance 1 km and depth 1.7 sec are not present in the image slope field.

In general, PWD methods fared better than FZE when creating a diffraction image migrated with incorrect migration velocity. DD-PWD operates in the data-domain, and was unaffected by migration velocity. PI-PWD was able to successfully remove reflections and leave diffractions in both under and over-migrated conditions. Because incorrectly migrated diffractions are not flat in the dip-angle gather domain, they become stationary near dip angles. These stationary portions tend to coincide with the stationary portions of reflections, so they are masked with reflection energy,

with FZE removing both reflections and diffractions.

In the first field data example containing a set of faults, both PWD methods produced accurate diffraction images. Both PWD diffraction images were fairly equivalent, so DD-PWD was judged to be the superior method thanks to its decreased computational cost. Fresnel zone elimination removed reflection energy, but because diffraction energy was primarily contained at small dip angles, it was suppressed as well.

PI-PWD most effectively removed reflection energy in the second field data example containing reflections and diffractions from a salt dome. Fresnel-zone elimination suppressed much diffraction energy and left low frequency planar signal. DD-PWD was able to isolate diffractions, but left some remnant reflection signal. Remnant reflection energy coincided with areas where data slope changes rapidly and where data curvature may not be continuous. Although the migrated image contains reflections whose slope changes rapidly, migration has somewhat smoothed these events, enabling better slope field calculation, and hence superior diffraction extraction when operating on partial-images. This resulted in a PI-PWD diffraction image with less remnant reflection energy.

Direct comparison of PWD methods and FZE is difficult because all methods contain several adjustable parameters. PWD's primary parameter is the smoothing used in dip calculation. If smoothing is too great the PWD filter may leave reflections with laterally variable dip. If smoothing is too small, the filter will destroy diffractions. AD relies on more parameters than PWD: in addition to calculating dip for Fresnel zone masking, a mask width must be supplied. If too narrow a mask is used reflections will remain. Expanding mask width further reduces diffraction energy. Based on

the experiments of this chapter, PWD methods appear more effective at diffraction extraction than FZE because they do not remove diffraction energy which is present near the Fresnel zone.

DD-PWD and PI-PWD both produce accurate diffraction images. Plane-wave destruction in the extra dip-angle dimension adds an extra computational cost to PI-PWD. PI-PWD is limited to angle migration techniques that output constant-dip partial-images, while DD-PWD operates in the data-domain and therefore can be used with any migration algorithm. PI-PWD seems best suited for diffraction imaging of complex media where DD-PWD may fail to remove all reflections from un-migrated data.

Chapter 4

Diffraction imaging and velocity analysis using oriented velocity continuation

In this chapter, I propose a method for seismic diffraction imaging and velocity analysis by separating diffractions from specular reflections and decomposing them into slope components. I image slope components using extrapolation in migration velocity in time-space-slope coordinates. The extrapolation is described by a convection-type partial differential equation and implemented efficiently in the Fourier domain. Synthetic and field data experiments show that the proposed algorithm is able to detect accurate time-migration velocities by automatically measuring the flatness of events in dip-angle gathers.

INTRODUCTION

The idea of separating diffractions from specular reflections and using diffraction focusing as a tool for velocity analysis goes back to the work of Harlan et al. (1984). Sava et al. (2005) adopted it for wave-equation migration velocity analysis in depth migration. Fomel et al. (2007) developed a constructive procedure for diffraction separation based on plane-wave destruction and diffraction focusing analysis based on velocity continuation and local kurtosis. The procedure was extended to 3-D azimuthally-anisotropic velocity analysis by Burnett and Fomel (2011). However,

*Some of the material in this chapter was submitted as Decker and Fomel (2014)

local kurtosis may not be an optimal measure for diffraction focusing, because it requires smoothing or windowing in space, which may reduce spatial resolution.

A particularly convenient domain for separating diffractions and reflections and for analyzing migration velocities is dip-angle gathers (Landa et al., 2008; Reshef and Landa, 2009; Klokov and Fomel, 2012). In the dip-angle domain, specular reflections appear as hyperbolic events centered at the reflector dip, and diffractions appear flat when imaged at the location of the diffractor with the correct velocity (Audebert et al., 2002). Measuring flatness of diffraction events in dip-angle gathers, as opposed to flatness of reflection and diffraction events in reflection-angle gathers, provides an alternative constraint on seismic velocity. Traditionally, dip-angle gathers are constructed with Kirchhoff migration (Fomel and Prucha, 1999; Xu et al., 2001; Brandesberg-Dahl et al., 2003; Cheng et al., 2011; Koren and Ravve, 2011; Bashkardin et al., 2012; Klokov and Fomel, 2013b).

In this paper, I adopt the dip-angle approach to devise a constructive and efficient procedure for estimating velocities in time-domain processing using data decomposition in dip (Ghosh and Fomel, 2012) and velocity continuation in the midpoint-time-slope domain. By analogy with the "oriented wave equation" (Fomel, 2003a), I call this approach *oriented velocity continuation* and develop a fast spectral method for its practical implementation. Using a field-data experiment, I demonstrate the effectiveness of oriented velocity continuation in diffraction imaging and velocity analysis.

ORIENTED VELOCITY CONTINUATION

Velocity continuation (Fomel, 2003c) is the imaginary process of a continuous transformation of seismic time-migrated images in migration velocity. In the most general terms, the kinematics of velocity continuation can be described by an equation of the Hamilton-Jacobi type

$$\frac{\partial \tau}{\partial v} = F(v, \tau, \mathbf{x}, \nabla \tau) \ , \tag{4.1}$$

where $\tau(\mathbf{x}, v)$ is the location of a time-migrated reflector imaged with time-migration velocity v. The particular form of function F in equation (4.1) depends on the acquisition geometry of the input data. For the simplest case of zero-offset 2D velocity continuation,

$$F(v, t, x, p) = v\, t\, p^2 \ , \tag{4.2}$$

and equation (4.1) corresponds to the characteristic equation of the image propagation process (Claerbout, 1986; Fomel, 1994)

$$\frac{\partial^2 I}{\partial t\, \partial v} = v\, t\, \frac{\partial^2 I}{\partial t\, \partial x^2} \ , \tag{4.3}$$

which described a propagation of the time-migrated image $I(t, x, v)$ in velocity v. Time-domain imaging can be performed effectively by extrapolating images in velocity and estimating velocity $v_m(t, x)$ of the best image (Rothman et al., 1985; Larner and Beasley, 1987; Fomel, 2003b; Fomel and Landa, 2014).

As shown by Fomel (2003a), it is possible to extend the formulation of a wave propagation process from the usual time-and-space coordinates to the phase space consisting of time, space, and slope. Applying a similar approach to equation (4.1) and employing the Hamilton-Jacobi theory (Courant and Hilbert, 1989; Evans, 2010) leads

to the corresponding system of ordinary differential equations for the characteristics (velocity rays), as follows:

$$\frac{d\mathbf{x}}{dv} = -\nabla_p F \;, \tag{4.4}$$

$$\frac{d\mathbf{p}}{dv} = \nabla_x F + \frac{\partial F}{\partial t}\,\mathbf{p} \;, \tag{4.5}$$

$$\frac{dt}{dv} = F - \nabla_p F \cdot \mathbf{p} \;, \tag{4.6}$$

where $\mathbf{p}$ stands for $\nabla\tau$.

If the image $I(t, \mathbf{x}, v)$ is decomposed in slope components $\widehat{I}(t, \mathbf{x}, \mathbf{p}, v)$ so that

$$I(t, \mathbf{x}, v) = \int \widehat{I}(t, \mathbf{x}, \mathbf{p}, v)\, d\mathbf{p} \;, \tag{4.7}$$

We can then look for an equation that would adequately describe a continuous transformation of $\widehat{I}$. To preserve the geometry of the transformation, it is sufficient to require that $\widehat{I}$ transports along the characteristics described by equations (4.4-4.6). Applying partial derivatives and the chain rule, yields the Liouville equation

$$\frac{\partial \widehat{I}}{\partial v} = (F - \nabla_p F \cdot \mathbf{p})\,\frac{\partial \widehat{I}}{\partial t} - \nabla_p F \cdot \nabla_x \widehat{I} + \left(\nabla_x F + \frac{\partial F}{\partial \tau}\,\mathbf{p}\right) \cdot \nabla_p \widehat{I} \;. \tag{4.8}$$

Equation (4.8) describes, in the most general form, the process of *oriented velocity continuation*, image propagation in velocity in the coordinates of time-space-slope. It is a linear first-order partial differential equation of convection type.

Zero-offset velocity continuation

To adopt the general theory described above to the simplest case of zero-offset 2D velocity continuation, I substitute equation (4.2) into (4.8), arriving at the equation

$$\frac{\partial \widehat{I}}{\partial v} = -v\,t\,p^2\,\frac{\partial \widehat{I}}{\partial t} - 2\,v\,t\,p\,\frac{\partial \widehat{I}}{\partial x} + v\,p^3\,\frac{\partial \widehat{I}}{\partial p} \;, \tag{4.9}$$

which is analogous to equation (4.3) but describes image propagation in the time-space-slope coordinates rather than the usual time-space coordinates. After this kind of extrapolation, regular images can be reconstructed by stacking over slope according to equation (4.7). On the other hand, dip-angle gathers can be extracted before stacking by analyzing $\{t, p\}$ panels for different image locations x and velocities v. Measuring flatness of diffraction events in dip-angle gathers provides a constructive method for estimating migration velocity.

For practical implementation, the formulation of oriented velocity continuation can be simplified further by employing a stretch from the regular time coordinate to squared time $\sigma = t^2$ (Fomel, 2003b). According to this transformation, the Hamilton-Jacobi equation (4.1) becomes

$$\frac{\partial \sigma}{\partial v} = \frac{v}{2} \left(\frac{\partial \sigma}{\partial x} \right)^2 , \tag{4.10}$$

which leads to the simpler form of the oriented equation

$$\frac{\partial \hat{I}}{\partial v} = -\frac{v}{2} q^2 \frac{\partial \hat{I}}{\partial \sigma} - v\, q \frac{\partial \hat{I}}{\partial x} , \tag{4.11}$$

where q corresponds to $\partial\sigma/\partial x$, and the image is constructed in $\{\sigma, x, q\}$ coordinates instead of $\{t, x, p\}$ coordinates. Applying the Fourier transform, I further transform equation (4.9) to

$$\frac{\partial \tilde{I}}{\partial v} = -i\,\omega \frac{v}{2} q^2 \tilde{I} - i\, v\, q\, k\, \tilde{I} , \tag{4.12}$$

where $\tilde{I}(\omega, k, q, v)$ is the double Fourier transform of $\hat{I}(\sigma, x, q, v)$ in σ and x. Equation (4.12) has the simple analytical solution

$$\tilde{I}(\omega, k, q, v) = \tilde{I}(\omega, k, q, v_0)\, e^{-i\,(\omega\, q^2/4 + q\, k/2)\,(v^2 - v_0^2)} . \tag{4.13}$$

This derivation suggests the following algorithm for time-domain imaging using zero-offset 2D oriented velocity continuation:

1. Start with initial time migration with a constant velocity v_0 to generate $I(t, x, v_0)$.
2. Apply vertical time stretch to transform from t to σ.
3. Apply Fourier transform from σ to ω.
4. Perform slope decomposition (described in the next section) to generate $\hat{I}(\omega, x, q, v_0)$. This operation is parallel in ω.
5. Apply Fourier transform from x to k to generate $\tilde{I}(\omega, k, q, v_0)$. This operation is parallel in q.
6. Apply the phase-shift filter from equation (4.13) to generate $\tilde{I}(\omega, k, q, v)$ for multiple values of v. This operation is data-intensive but parallel in both q and k.
7. Apply inverse double Fourier transform to generate $\hat{I}(\sigma, x, q, v)$.
8. Apply inverse time stretch from σ to t.
9. Stack over q and extract the slice at time-migration velocity $v_m(t, x)$ to generate the final time-migrated image $I(t, x, v_m(t, x))$.

In order to estimate the velocity $v_m(t, x)$, I adopt the workflow described above to diffraction imaging and modify it as follows:

- After Step 1, I separate reflections and diffractions in the initial image using DD-PWD described in the previous chapter.
- After Step 8, I analyze dip-angle gathers $\hat{I}(t, x, q, v)$ and pick the velocity $v_m(t, x)$ that corresponds to the maximum flatness (semblance) over q. This

approach follows the principle of flatness of diffraction events in dip-angle gathers (Landa et al., 2008; Reshef and Landa, 2009; Klokov and Fomel, 2012).

SLOPE DECOMPOSITION

In order to perform the initial slope decomposition (Step 4 in the algorithm above), I adopt the method of Ghosh and Fomel (2012). Analogous slope decomposition was discussed by Ottolini (1986) and implemented previously using the local-slant stack transform (Ventosa et al., 2012). The slope-decomposition algorithm suggested by Ghosh and Fomel (2012) is based on the time-frequency decomposition of Liu and Fomel (2013). Namely, at each frequency ω, I apply regularized non-stationary regression (Fomel, 2009) to transform from space x to space-slope x-q domain. The non-stationary regression amounts to finding complex coefficients $A_n(\omega, x)$ in the decomposition

$$D(\omega, x) = \sum_{n=1}^{N_p} D_n(\omega, x) \ , \tag{4.14}$$

where $D(\omega, x)$ is the image slice, and $d_n(\omega, x)$ is its slope component with slope q_n:

$$D_n(\omega, x) = A_n(\omega, x)\, e^{i\,\omega\,x\,q_n} \ . \tag{4.15}$$

Equation (4.14) is the discrete analog of equation (4.7). Similarly to the time-frequency decomposition proposed by Liu and Fomel (2013), shaping regularization is used to control the variability of A_n coefficients and to accelerate the algorithm.

SYNTHETIC EXAMPLE

To test the proposed method, I generate a synthetic zero-offset dataset using a constant velocity gradient (Figure 4.1a) and varying density (Figure 4.1b) to create

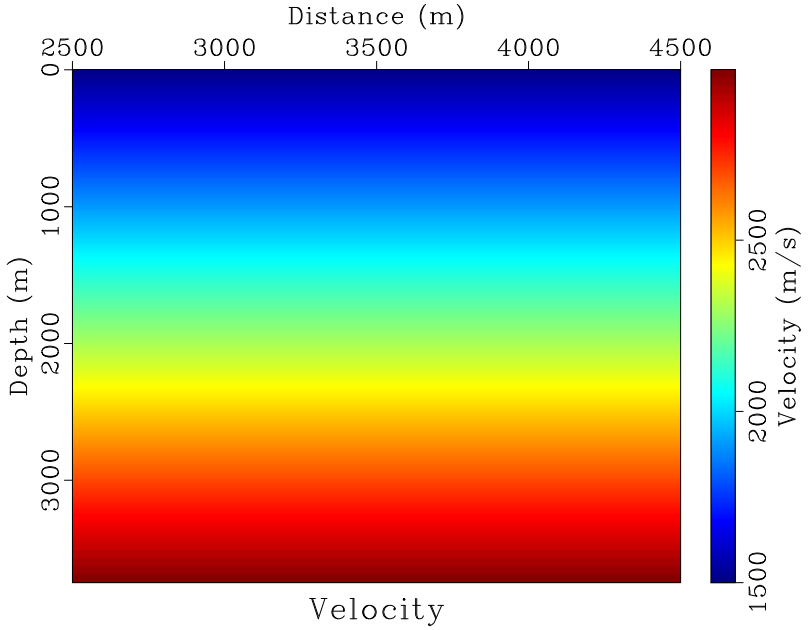

a

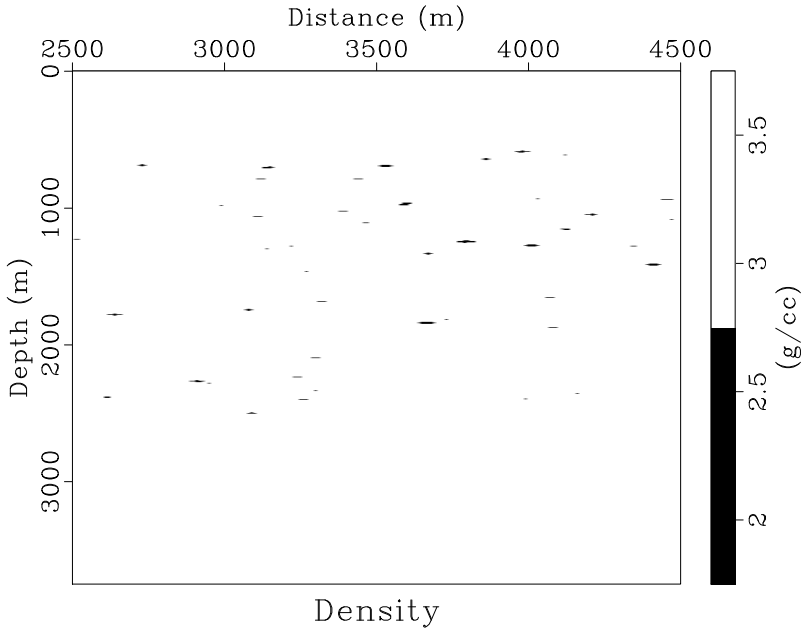

b

Figure 4.1: Synthetic model for OVC: (a) constant gradient velocity field; (b) density field, variations of which cause diffractions. chap03/simple vel,den

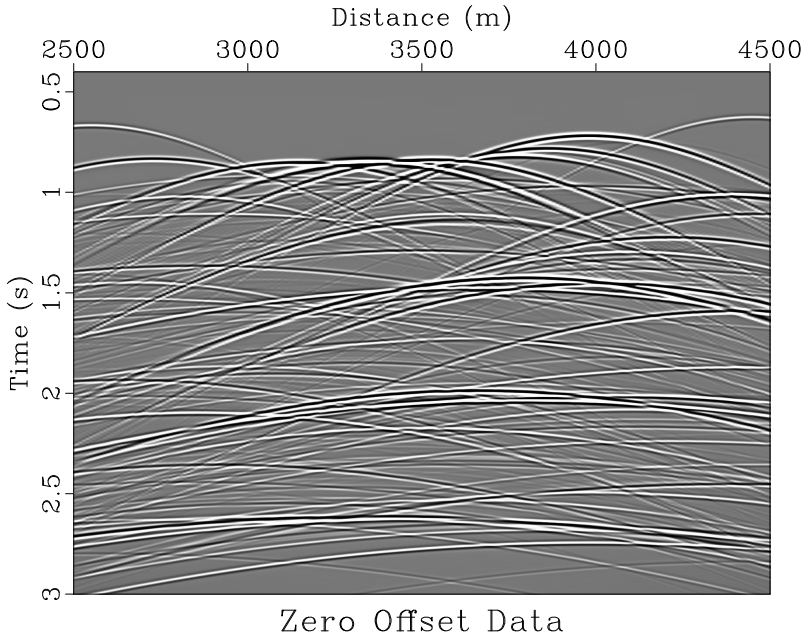

a

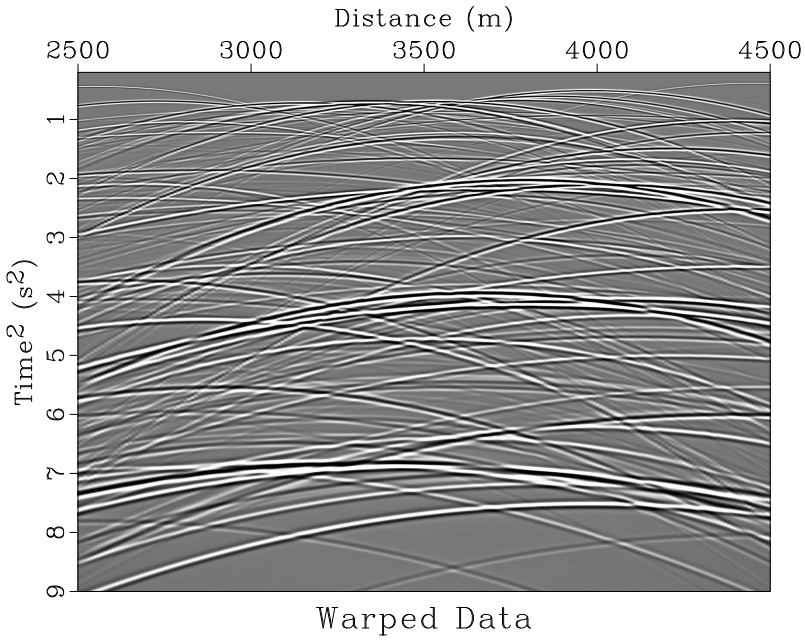

b

Figure 4.2: Synthetic diffraction data: (a) low-rank modeled zero-offset data; (b) diffraction data warped to squared time. chap03/simple exp,warp

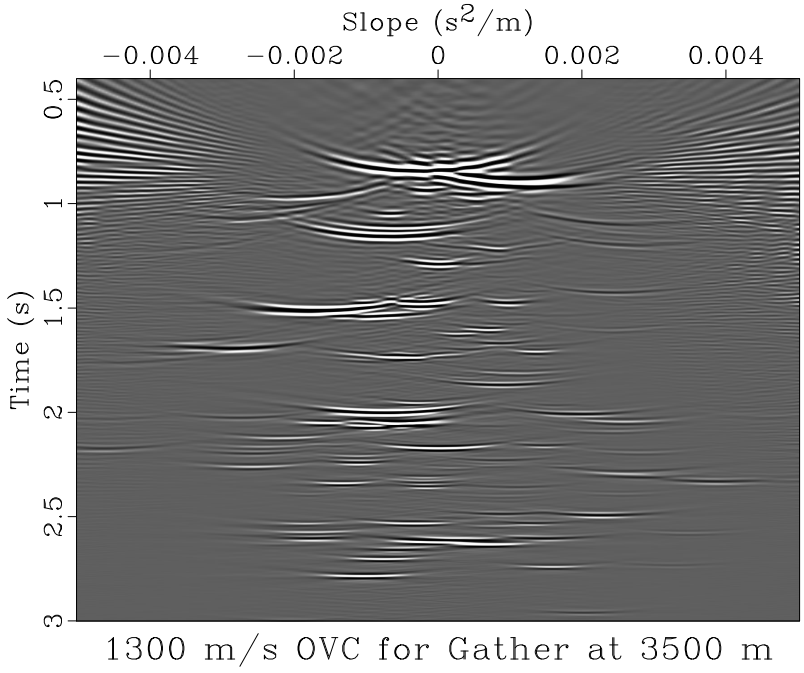

a

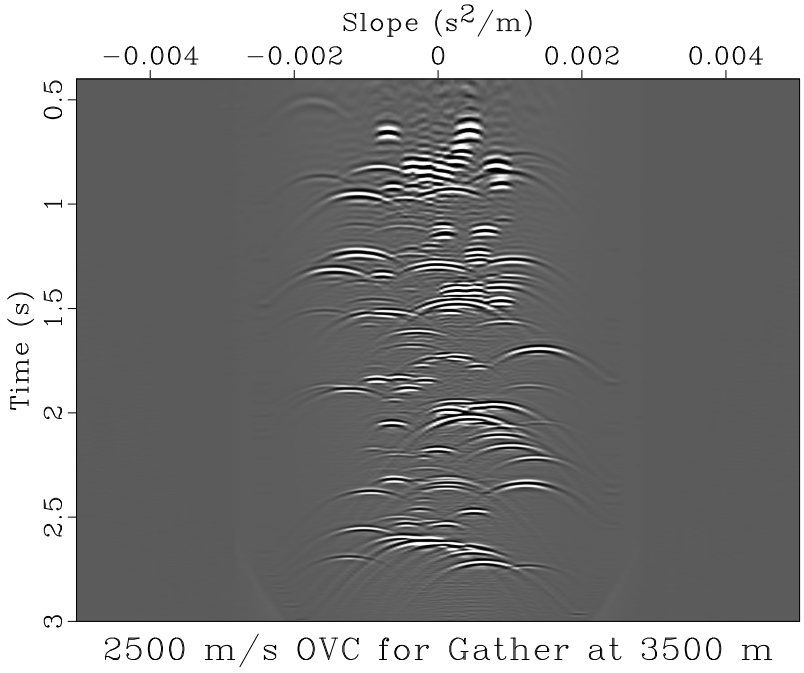

b

Figure 4.3: OVC for gather at distance 3500 m using: (a) minimum continuation velocity, $1300\frac{m}{s}$; (b) maximum continuation velocity, $2500\frac{m}{s}$. chap03/simple dagmin,dagmax

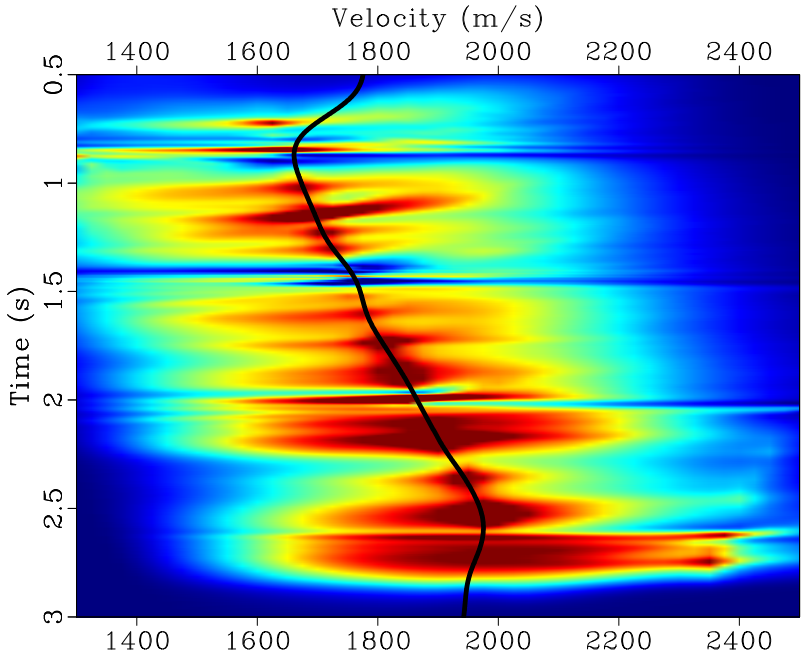

a

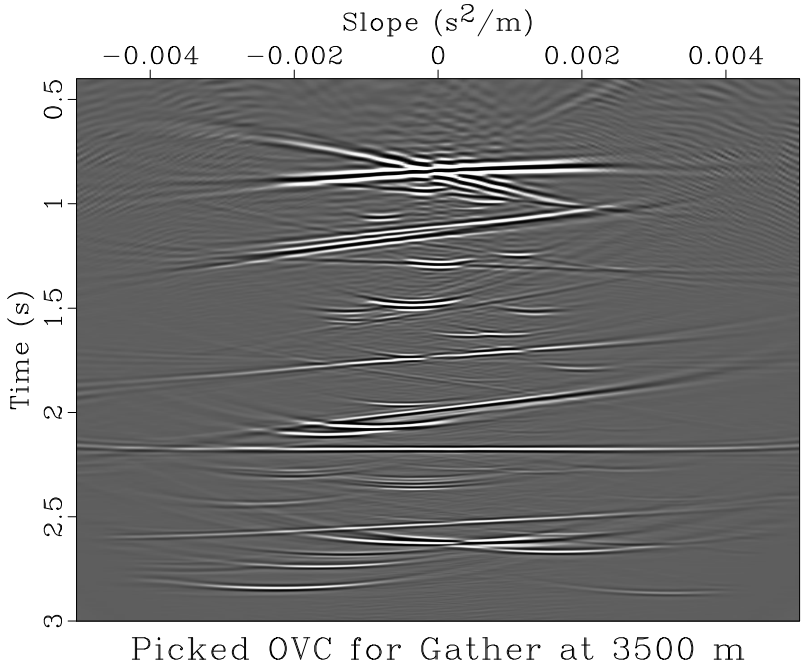

b

Figure 4.4: (a) Semblance field and picked velocity for gather at distance 3500 m; (b) OVC for gather at distance 3500 m using picked velocity. chap03/simple test,slice-dag

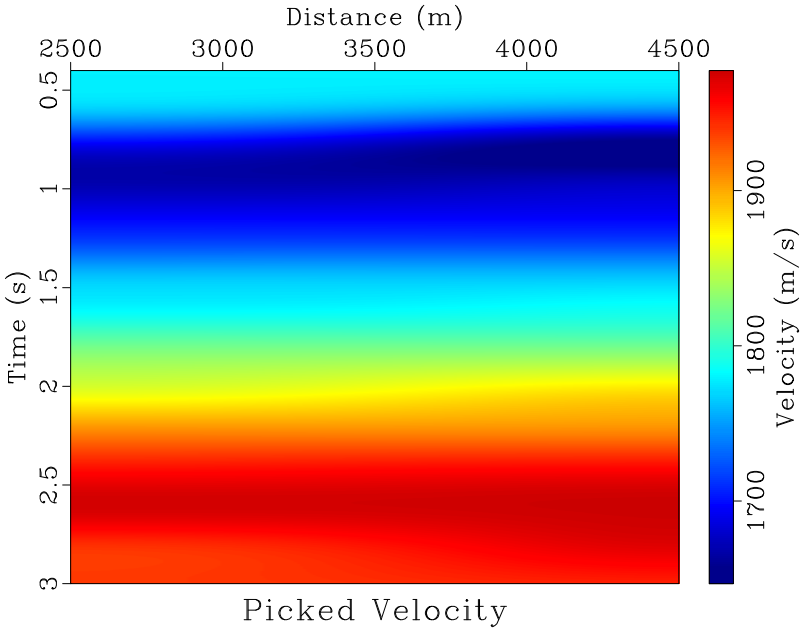

Figure 4.5: Picked migration velocity. chap03/simple vpick

diffractions. Zero-offset seismic reflection data are modeled (Figure 4.2a), and warped to squared time, (Figure 4.2b).

Slope decomposition and OVC are performed on warped data. A gather from distance = 3500 m, the center of the dataset, is visible for the minimum continued velocity in Figure 4.3a and the maximum continued velocity in Figure 4.3b. Notice that in Figure 4.3a slope gather diffraction events tend to bend upward, indicating under-migration, while diffraction events in Figure 4.3a bend downward, indicating over-migration.

Gather semblance, a measure of flatness, is calculated, and the velocity corresponding to maximum semblance is picked. The semblance and picking for the illustrated gather at distance = 3500 m is visible in Figure 4.4a, and the picked velocity field is visibile in Figure 4.5.

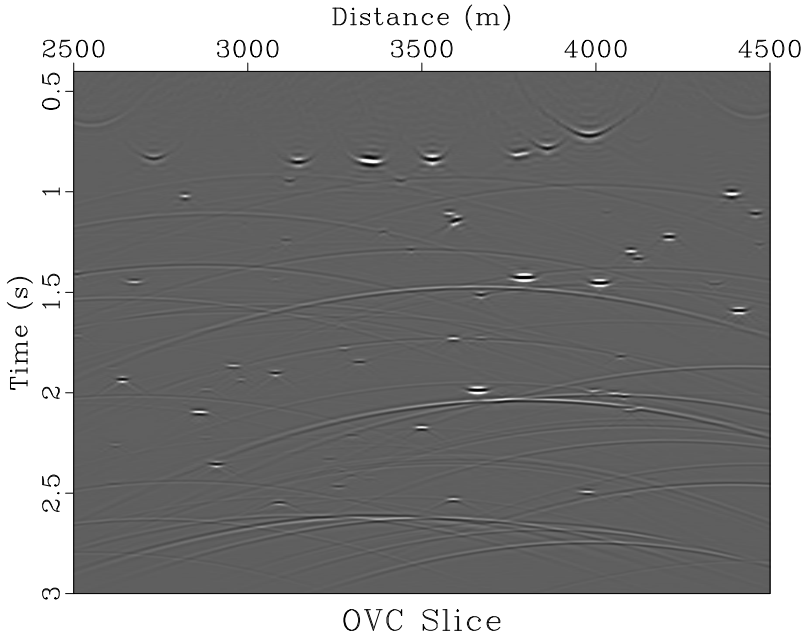

a

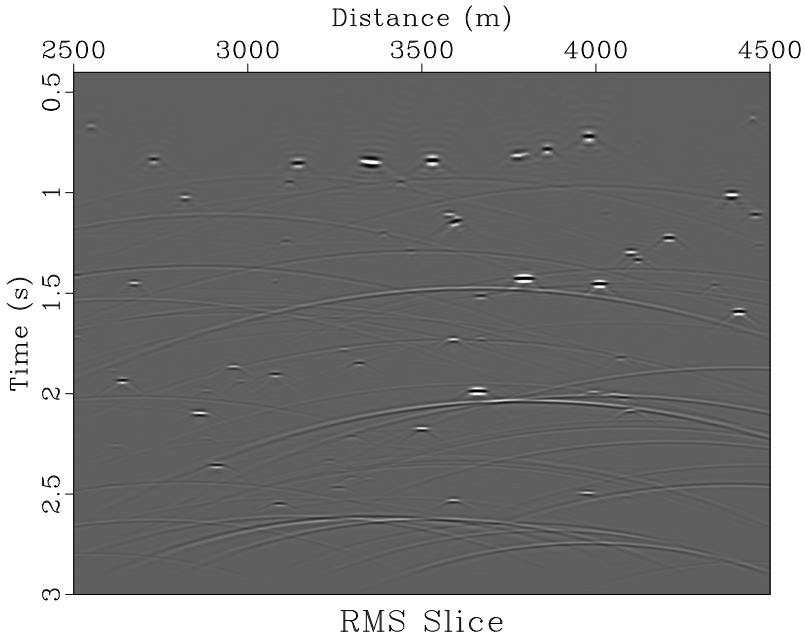

b

Figure 4.6: Synthetic model migrated images: (a) using picked velocity; (b) using ideal RMS velocity. chap03/simple slice,rms-slice

This velocity is used to pick the flattest gathers. An example picked gather from distance = 3500 m is visible in Figure 4.4b. Stacking across slope provides the diffraction image, Figure 4.6a. Diffractions are well focused, compare to the ideal migration image in Figure 4.6b.

FIELD DATA EXAMPLE

I next demonstrate an application of OVC on a Gulf of Mexico dataset, Figure 3.19a, containing a series of fault diffractions (Claerbout, 2005; Fomel et al., 2007). Similarly to the previous chapter, diffractions are extracted via DD-PWD (Figure 3.19b) and decomposed into slope (Figure 4.7a).

Next, I take the decomposed data through oriented velocity continuation over a range of velocities. Diffraction events bend upward in the minimum continuation velocity's slope gather (Figure 4.8a), indicating under-migration. Diffraction events in the maximum continuation velocity's slope gather (Figure 4.8b) bend downward, indicating over-migration.

Gather semblance is calculated for each continuation velocity, and the velocity with the maximum semblance value is picked, providing an estimated migration velocity field, shown in Figure 4.9. Gathers corresponding to this picked velocity are selected. Examining a slope-gather picked using migration velocity (Figure 4.7b), diffraction events near $t = 1.2$ s now appear flat, indicating that they have been correctly migrated. Diffraction events near $t = 1.4$ s have an upward slope because they come from a different midpoint.

Stacking over slope provides the final diffraction image (Figure 4.10a). Diffraction events tend to be well focused, indicating that the correct migration velocity has

been picked. I apply oriented velocity continuation to the original data from Figure 3.19a and stack over gathers selected with the appropriate velocity to generate the image of reflections and diffractions (Figure 4.10b).

CONCLUSIONS

I have developed and demonstrated an efficient and constructive procedure for time-domain velocity estimation. The method functions by decomposing data by slope and propagating slope components in velocity in the midpoint-time-slope domain. Semblance in dip-angle gathers is used as a measure for selecting velocities that correspond to correctly migrated flat diffraction events. Chosen velocities can be used to generate both diffraction and reflection images.

Flatness of slope-decomposed diffraction events can be more responsive to velocity perturbation than diffraction focusing, because it does not require smoothing or windowing in space. Therefore, the proposed method has the potential for diffraction velocity estimation with superior resolution.

This method can be easily extended to prestack data to improve velocity resolution. Extension to three dimensions using data decomposition by inline and crossline slope is also possible. Although such an extension adds an expense of additional dimensions, the high parallelism of Fourier-domain operations make it feasible.

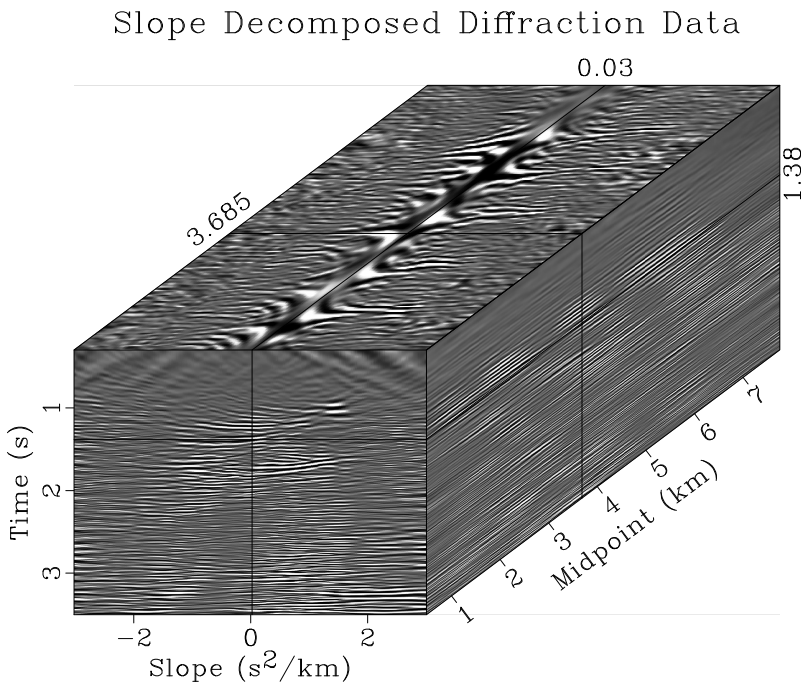

a

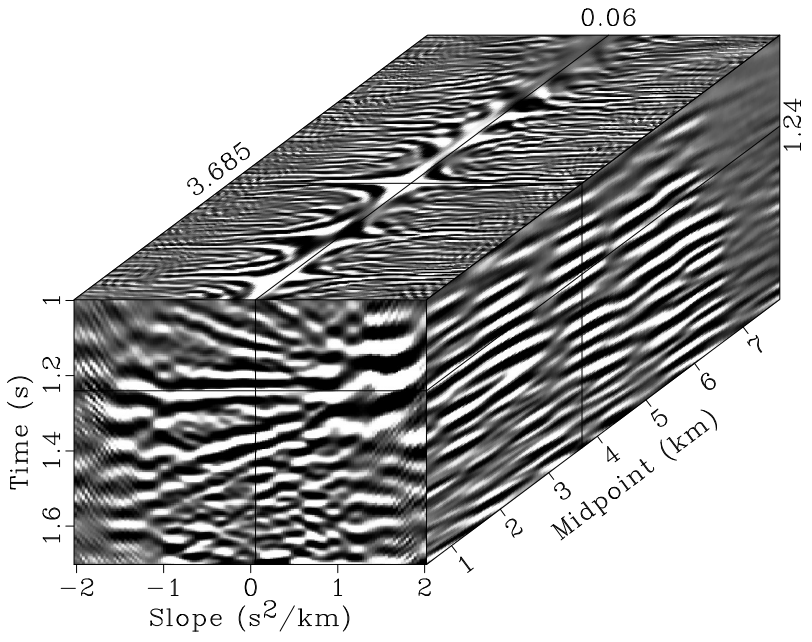

b

Figure 4.7: Gulf of Mexico field data example: (a) slope decomposition of diffraction data; (b) Oriented velocity continued gather using picked velocity from Figure 4.9 chap03/fault bei-pwd-txp,bei-pwd-image-gather

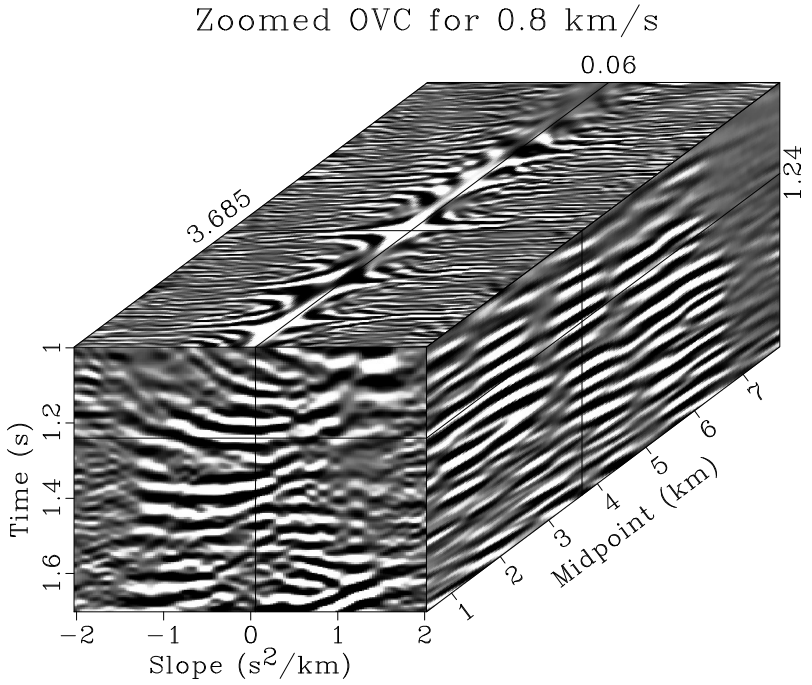

a

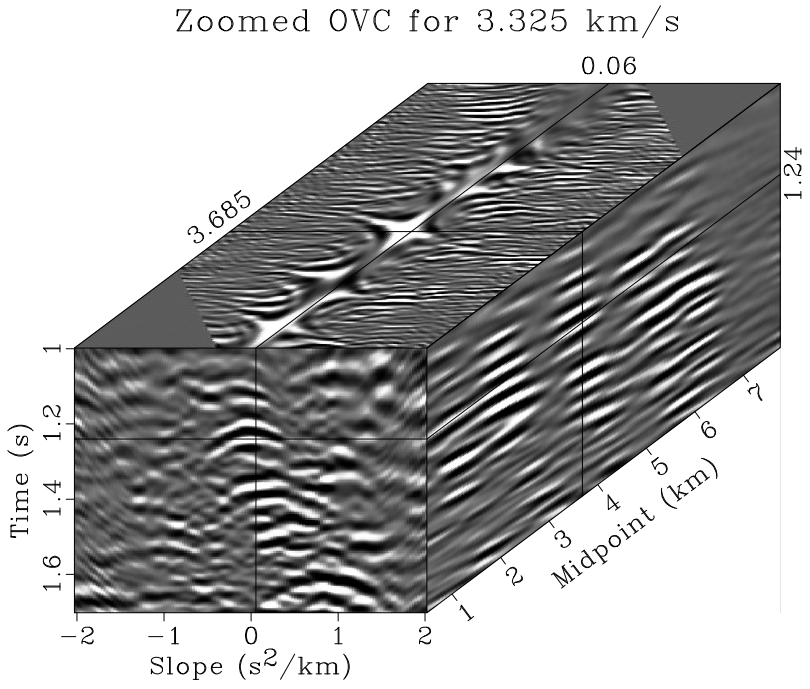

b

Figure 4.8: Oriented velocity continuation on Figure 4.7a using: (a) minimum continuation velocity, 0.8 km/s; (b) maximum continuation velocity, 3.325 km/s. chap03/fault bei-pwd-txp-vmin,bei-pwd-txp-vmax

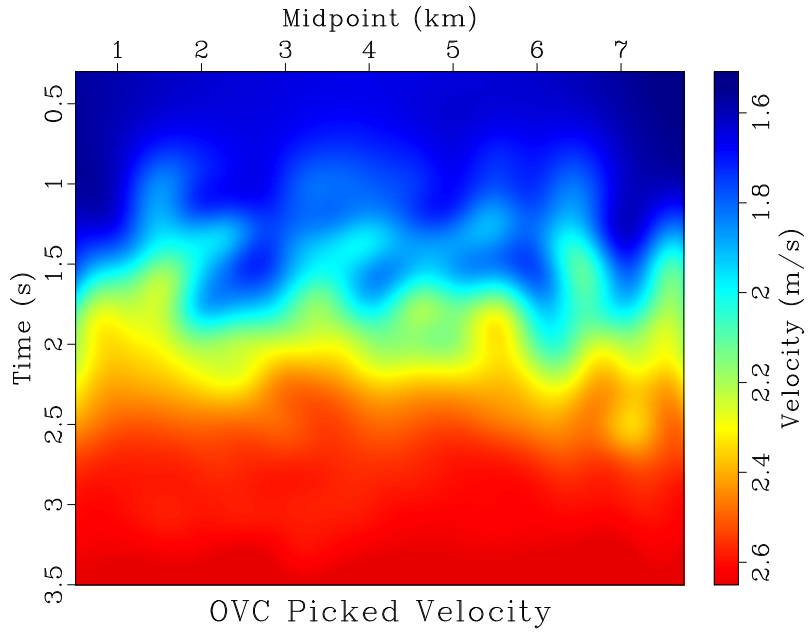

Figure 4.9: Picked velocity using oriented velocity continuation chap03/fault bei-vpick

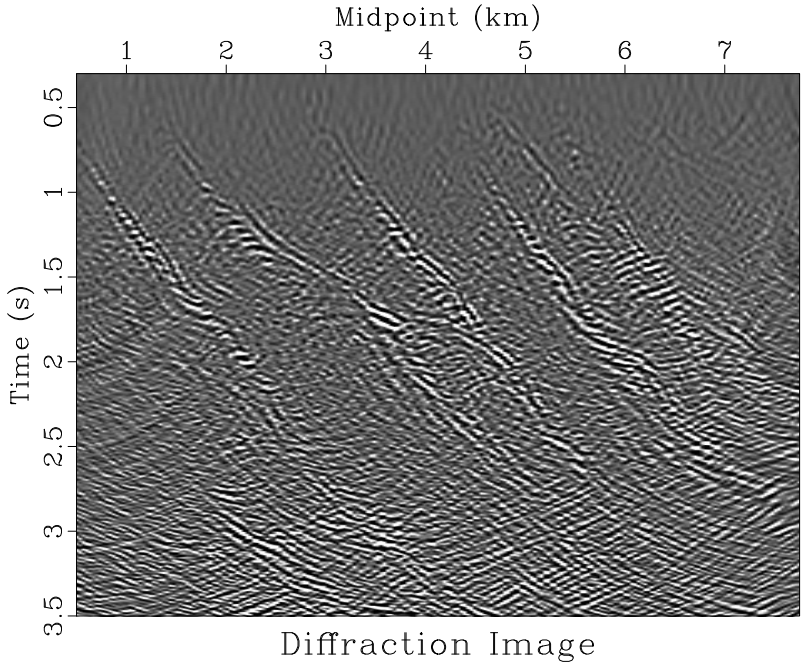

a

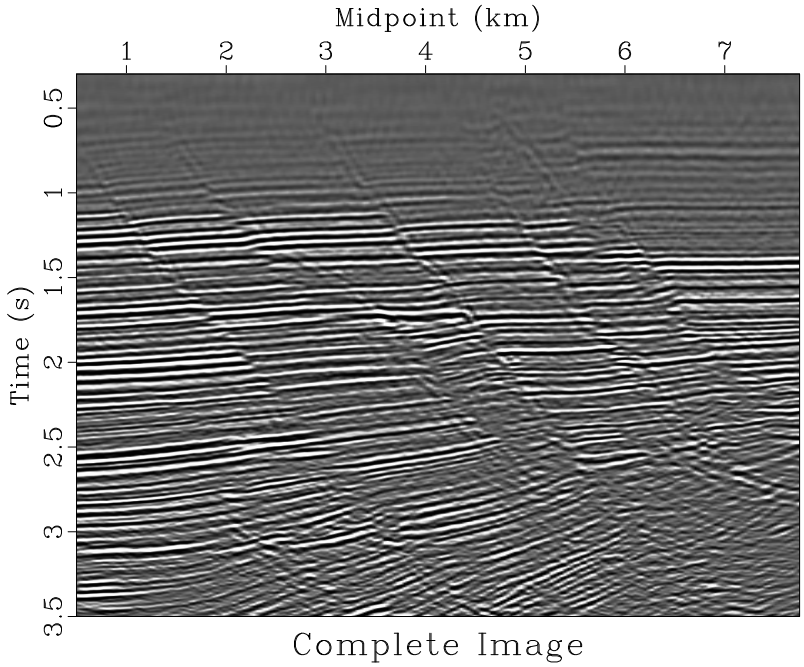

b

Figure 4.10: Migrated images using velocity field from Figure 4.9: (a) image of diffractions; (b) complete image. chap03/fault bei-pwd-image,bei-image

Chapter 5

Carbonate reservoir characterization using seismic diffraction imaging

Although extremely prolific worldwide, carbonate reservoirs are often challenging to characterize using traditional seismic reflection imaging techniques. In this chapter, I use computational experiments with synthetic models to demonstrate the possibility seismic diffraction imaging has of overcoming common obstacles associated with seismic reflection imaging and aiding interpreters of carbonate systems. I show that diffraction imaging improves the horizontal resolution of individual voids in a karst reservoir model and identification of heterogeneous regions below the resolution of reflections in a reservoir scale model.

INTRODUCTION

Carbonate reservoirs contain a majority of remaining proven oil reserves, yet are much more difficult to evaluate than their siliclastic counterparts (Fontaine et al., 1987; Palaz and Marfurt, 1997; Eberli et al., 2003; Sayers and Latimer, 2008). Many aspects of carbonate rocks make their seismic signature complex and difficult to interpret either qualitatively or quantitatively (Fontaine et al., 1987; Palaz and Marfurt, 1997; Eberli et al., 2004). Because carbonate rocks are generally faster than siliclastics, horizontal and vertical resolution is commonly low.

*Some of the material in this chapter was submitted as Decker et al. (2014)

Carbonate sediments are also more prone to complex, rapid diagenetic alteration after deposition which continues through the burial process (Vanario et al., 2008). These diagenetic processes are complex and significantly affect the acoustic properties of carbonate rocks. Postdepositional alteration such as karst processes or dolimitization can further complicate already heterogeneous deposits. Carbonate heterogeneity exists at different scales. Carbonates often posses larger-scale vugs, caves, and fracture networks, accompanied by small scale features such as microfractures, intergrainular porosity, and chemical alteration (Lucia, 1999).

The acoustic properties of carbonate rocks are not a simple function of mineralogy and porosity. Recent advances in rock mechanics have shown that the acoustic properties of carbonate rocks also depend on their pore type, size, shape, and distribution (Wang, 1997; Eberli et al., 2003; Baechle et al., 2005; Adam and Batzle, 2008; Weger et al., 2009). Heterogeneities in carbonates can scatter seismic energy, attenuating high frequency signal and reducing resolution. High impedance contrasts typically exist between carbonate structures and surrounding rocks, leading to a strong reflective interface that can generate multiple reflections. Impedance contrasts for strata within the carbonate body tend to be relatively weak, and horizontal heterogeneity means that reflections rarely have strong lateral continuation.

Rock physics models developed for siliclastics often fail to effectively describe carbonate systems (Sayers, 2008; Baechle et al., 2008). This makes relating velocities from core, sonic logs, and seismic very difficult, as these are sampled with different frequency waves. As a result, seismic images of carbonate deposits are usually not easily interpreted, especially at the reservoir scale (1-5 km). In addition, because of the intertwined control factors on the seismic response of carbonates, quantitative interpretation of the seismic signal is even more challenging. Janson et al. (2010)

and Janson and Fomel (2011) used outcrop analogues and synthetic models to better understand the seismic response of carbonate reservoirs.

The difficulties associated with reflection imaging encourage turning to seismic diffraction imaging. As explained in Chapter 1, seismic diffractions are a fundamentally different phenomenon than seismic reflections (Klem-Musatov, 1994). They occur when a seismic wave encounters a small scale feature and gets scattered. Diffractions may be caused by carbonate-related features including voids, faults, fractures, karsts, and other small-scale heterogeneities (Harlan et al., 1984; Khaidukov et al., 2004; Fomel et al., 2007; Moser and Howard, 2008; Klokov and Fomel, 2012). Rays emanating from seismic diffractions take more diverse paths than those associated with reflection events, and thus can contain more information about the subsurface (Neidell, 1997). These more diverse ray paths enable super-resolution with seismic diffraction imaging (Khaidukov et al., 2004).

I hypothesize that seismic diffraction imaging can potentially highlight features commonly observed in carbonates, such as karsts, voids, and small scale heterogeneities, with high resolution. These characteristics make seismic diffraction imaging well suited for use with carbonate imaging targets, where reflection resolution is typically limited. In this chapter, I use two synthetic models to illustrate how seismic diffraction imaging can better constrain void geometry and detect heterogenous zones that may not be immediately apparent in conventional reflection imaging.

SYNTHETIC MODELS

Ordovician Model

The first synthetic model is based on the very deeply buried (5,500-6,500 m) Ordovician limestone strata in Northwest China's Tarim Basin, which features anomalous seismic amplitude bright spots. These amplitude bright spots correspond to high-gamma-ray, low-velocity zones in wireline logs and have been interpreted by Zeng et al. (2011a) as paleokarst features. A geocellular model was built to study the seismic response of the paelokarst in detail (Janson et al., 2010; Zeng et al., 2011b). The synthetic model uses the Ordovician unconformity surface (boundary between a basal Ordovician interval and an overlying Silurian siliciclastic interval) which was mapped from subsurface seismic data (Figure 5.1). Collapsed paleocaves with cave sediments were modeled by randomly distributing low-AI circular geobodies that measured 300 $\times$ 300 m in the horizontal dimension and 18 m in vertical dimension. The AI (approximated by acoustic velocity) is distributed using a sequential Gaussian simulation with parameters derived from a sonic log in the cored well (Janson et al., 2010; Zeng et al., 2011a,b).

Permo Triassic Khuff Model

The second model examines rocks equivalent to the Permian-Triassic Khuff-A and -B reservoirs, which crop out near Buraydah in central Saudi Arabia. An outcrop-based geocellular model 600 m $\times$ 385 m $\times$ some 30 m was built to investigate the effect of small-scale carbonate reservoir heterogeneities on subsurface flow models (Janson et al., 2013). In addition, the 3D geological geocellular model was converted into a acoustic impedence (AI) model using laboratory velocity (Figure 5.2a) and density (Figure 5.2b) measurement from outcrop plugs. An average acoustic impedance value

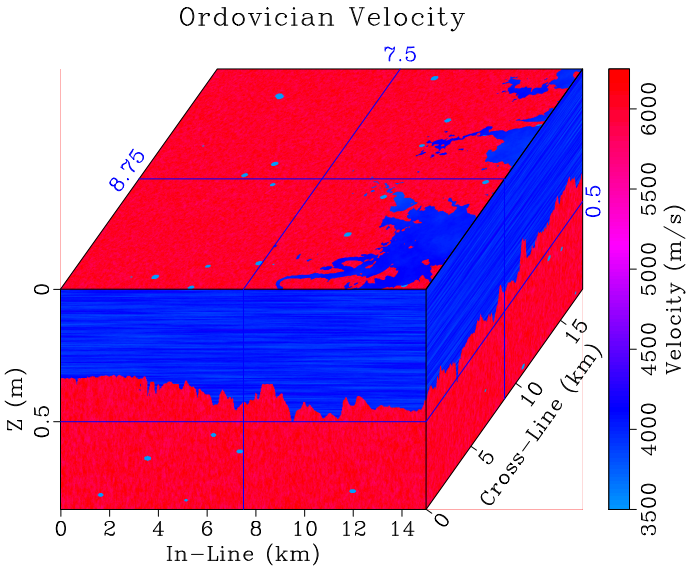

Figure 5.1: Ordovician velocity model. chap04/ord20hz vp

for each lithofacies present in the geological model was used to convert the lithofacies model into an impedance volume (Figure 5.3) in order to maintain the realistic level and distribution of reservoir heterogeneities. Because of its limited size, the outcrop-based geocellular model was scaled up for seismic modeling by addition of a similar but simpler model of strata below it as well as acoustically constant buffer layers above and below to make the final model 110 m thick.

METHOD

As explained in Chapter 1, seismic diffraction events carry much less energy than reflection events, requiring that they be separated to be utilized. Several methods for seismic diffraction extraction exist (Harlan et al., 1984; Landa et al., 1987; Kanasewich and Phadke, 1988; Landa and Keydar, 1998; Khaidukov et al., 2004; Landa et al., 2008; Klokov and Fomel, 2012; Decker et al., 2013), including plane-wave destruction

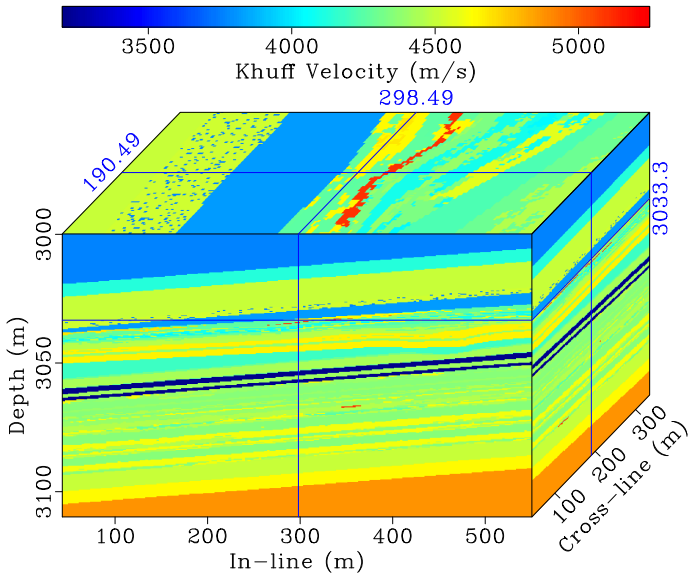

a

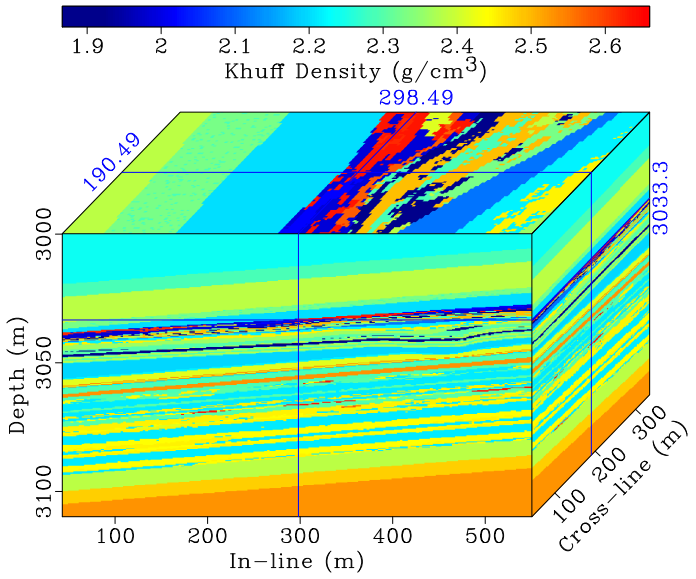

b

Figure 5.2: Khuff synthetic model: (a) velocity; (b) density
chap04/smallkhuff kvp,kden

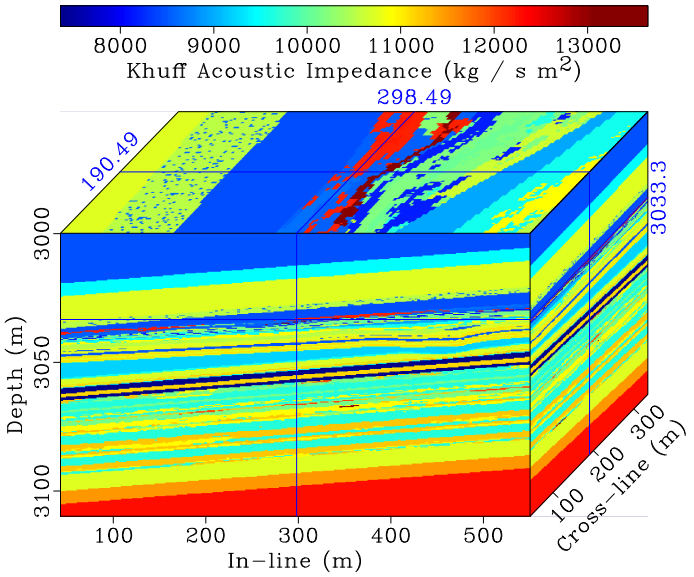

Figure 5.3: Khuff synthetic model acoustic impedance chap04/smallkhuff kai

applied to common-offset data (Fomel et al., 2007).

I use the DD-PWD method from Chapter 2 to determine the dominant slope field of our modeled zero-offset data and remove the reflections that conform with local slope, providing zero-offset diffraction data. Zero-offset "conventional" data containing diffractions and reflections as well as zero-offset diffraction data are migrated, providing our conventional and diffraction images respectively. A workflow for the diffraction extraction and imaging process starting from common-offset data is displayed in Figure 3.12a.

Although I employ the same method of diffraction extraction on both the Orodovician and Khuff synthetic models, I adopt different methods of modeling and migration that are best suited for each model's scale and subsurface position. Reverse-time migration (Zhang and Sun, 2009; Fomel et al., 2013b) is used on the Ordovician model for greater accuracy. One-way wave-equation migration (Gazdag and

Sguazzero, 1984; Kessinger, 1992) is utilized on the reservoir-scale Khuff model to allow for upward continuation of modeled data through an overburden in order to model the response of the interval at a geologically plausible depth.

RESULTS

I begin my first experiment on the constant-density Ordovician synthetic velocity model, Figure 5.1, by calculating reflectivity. I transform this reflectivity to the time domain, convolve it with a 20 Hz ricker wavelet, and transform it back to the depth domain to create an idealized seismic reflectivity image. Forward modeling is operated on the idealized image using low-rank method in the time domain (Fomel et al., 2013b), providing conventional zero-offset data, shown in Figure 5.4a.

Data slope are calculated using PWD, and reflections conforming with that slope are removed, providing the set of diffraction data shown in Figure 5.4b. Conventional and diffraction data are then migrated using low-rank RTM with a smoothed-slowness velocity field to provide a conventional image, shown in Figure 5.5a, and a diffraction image, shown in Figure 5.5b.

To highlight the improvement in horizontal feature resolution using diffraction imaging I take two depth slices from the images. The depth slices represent the average of a 20 m interval centered around the target depth. Depth slices of the conventional and diffraction images for the first depth, 0.55 km, are visible in Figures 5.6a and 5.6b. Zooming in on an interesting region of these slices to generates Figure 5.7.

Conventional and diffraction image slices for the second depth, 0.7 km, are shown in Figure 5.8. Zooming in on an interesting part of these slices creates Fig-

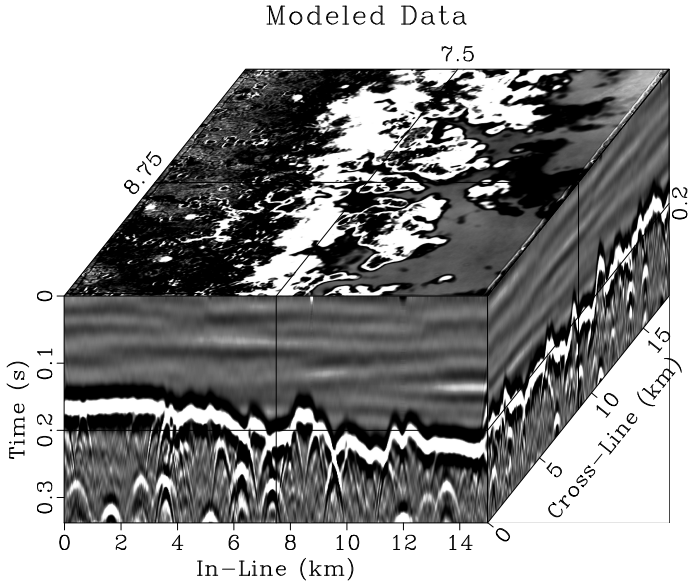

a

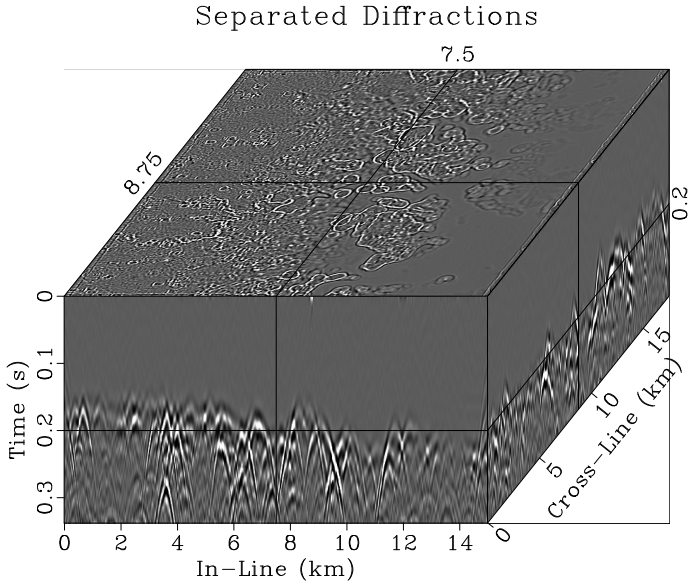

b

Figure 5.4: Modeled Ordovician zero-offset data: (a) conventional data; (b) separated diffraction data chap04/ord20hz exp0,diffractions

ure 5.9.

I next use the Khuff synthetic model to illustrate how diffractions may be used to characterize features at the reservoir scale using higher frequency data.

The experiment begins with the Khuff velocity and density models, shown in Figures 5.2a and 5.2b respectively. I multiply density and velocity data to obtain acoustic impedance (Figure 5.3). Reflectivity is calculated from this acoustic impedance, transformed to the time domain, convolved with a 100 Hz ricker wavelet, and transformed back to the depth domain to provide an idealized seismic reflection image. I model the zero-offset reservoir response using one-way wave equation modeling, and then upward continue the reservoir response through a 3 km thick overburden to generate the zero-offset data, shown in Figure 5.10a.

I separate diffractions using PWD. Data slope are calculated and reflection events conforming to slope are removed, leaving zero-offset diffraction data (Figure 5.10b).

Conventional and diffraction zero-offset data are then downward continued through the smoothed-slowness overburden, and then depth migrated through the smoothed-slowness reservoir. This provides a conventional image (Figure 5.11a) and a diffraction image (Figure 5.11b). I zoom in on a horizontal cross section along Cross-Line 150 m for the conventional and diffraction images, creating Figure 5.12. I also generate a cross section along In-Line 250 m (Figure 5.13).

INTERPRETATION

The following analysis shows that seismic diffraction imaging can better highlight features in synthetic models compared with reflection imaging.

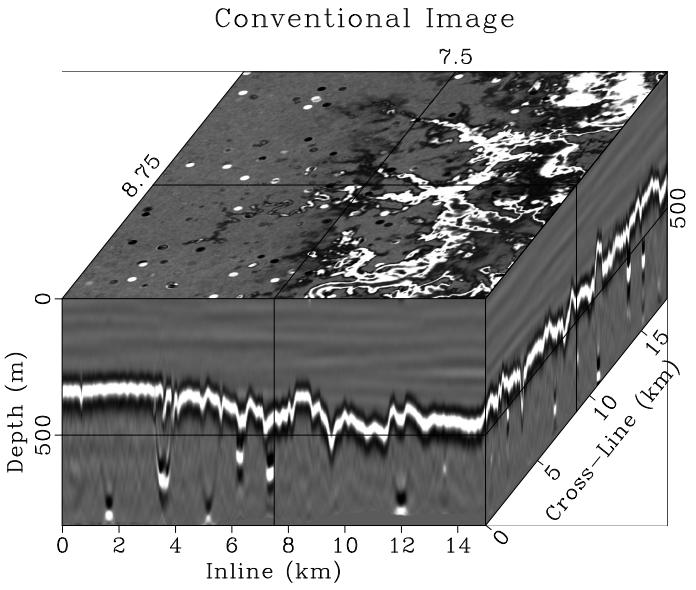

a

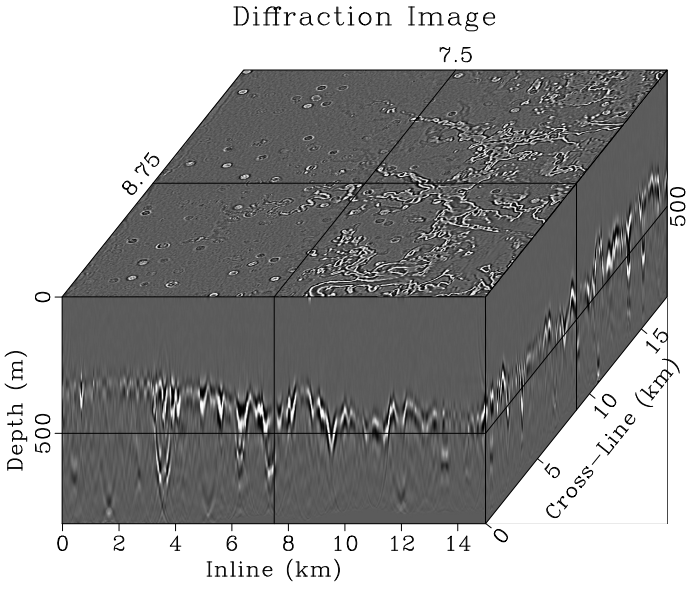

b

Figure 5.5: Low-rank RTM smoothed-slowness images for Ordovician model: (a) conventional image; (b) seismic diffraction image chap04/ord20hz exp0-mig,diffractions-mig

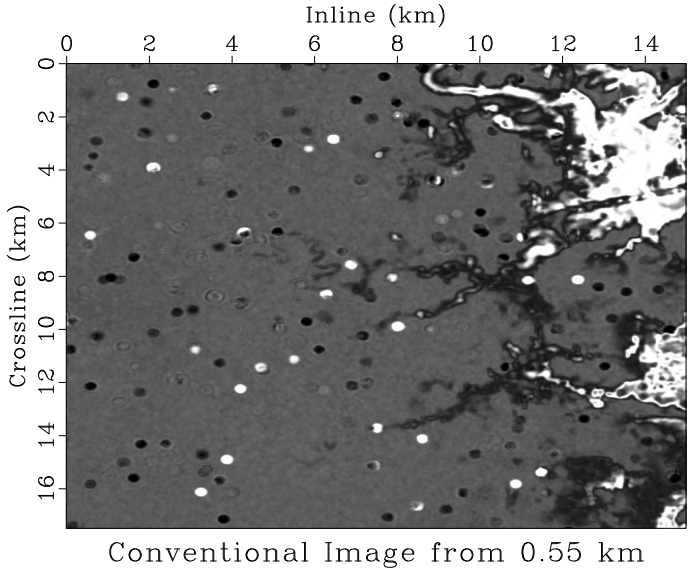

a

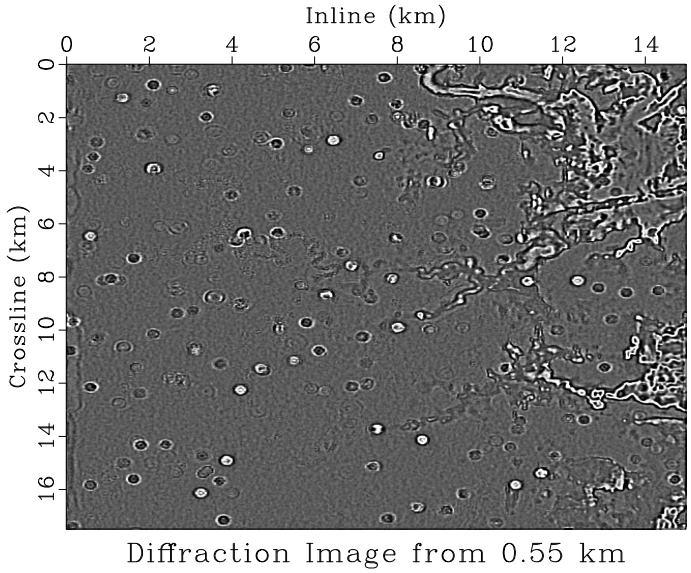

b

Figure 5.6: Ordovician depth slices from 0.55 km: (a) conventional image; (b) seismic diffraction image chap04/ord20hz img2dstk-1,dif2dstk-1

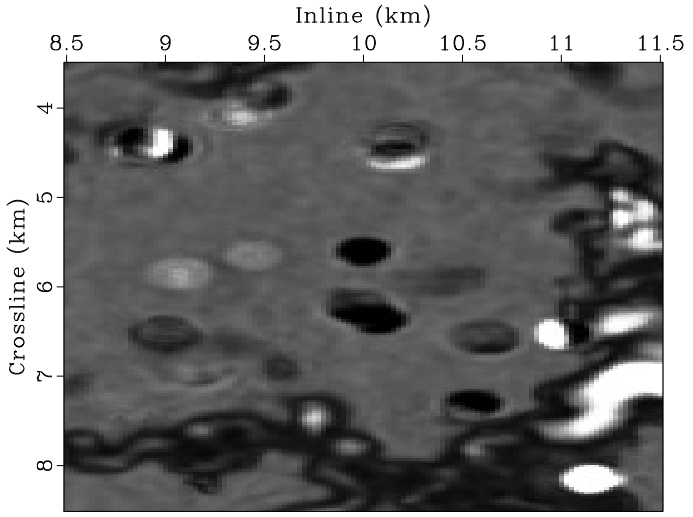

Zoomed Conventional Image from 0.55 km

a

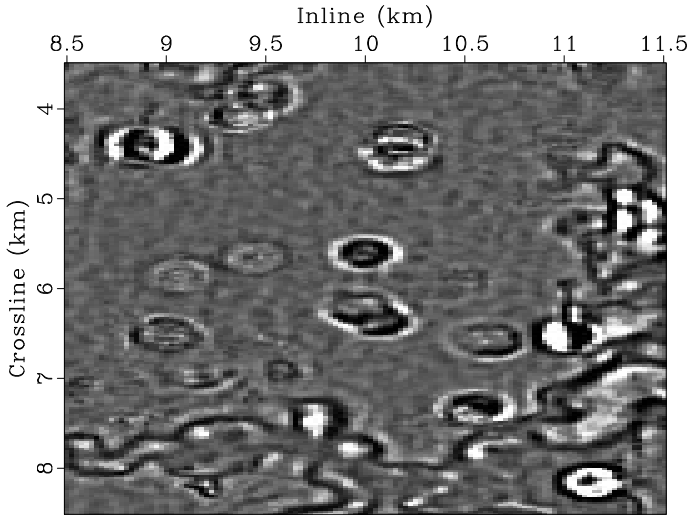

Zoomed Diffraction Image from 0.55 km

b

Figure 5.7: Zoomed Ordovician depth slices from 0.55 km: (a) conventional image; (b) seismic diffraction image chap04/ord20hz img2dstka-1,dif2dstka-1

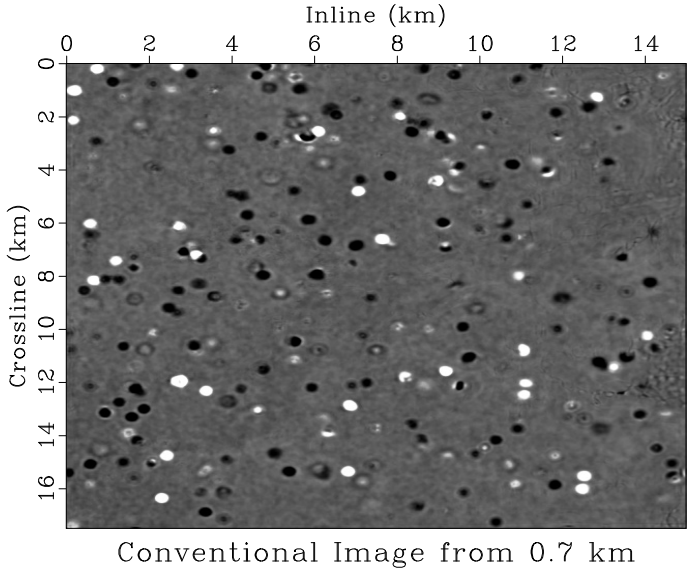

a

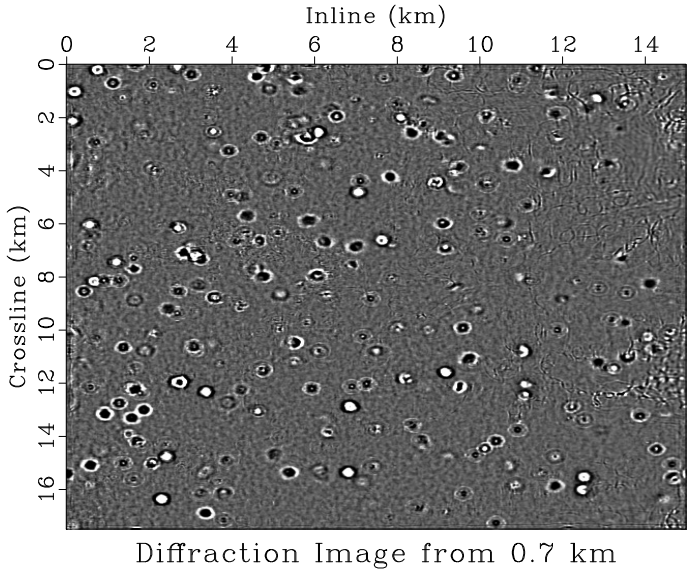

b

Figure 5.8: Ordovician depth slices from 0.7 km: (a) conventional image; (b) seismic diffraction image chap04/ord20hz img2dstk-2,dif2dstk-2

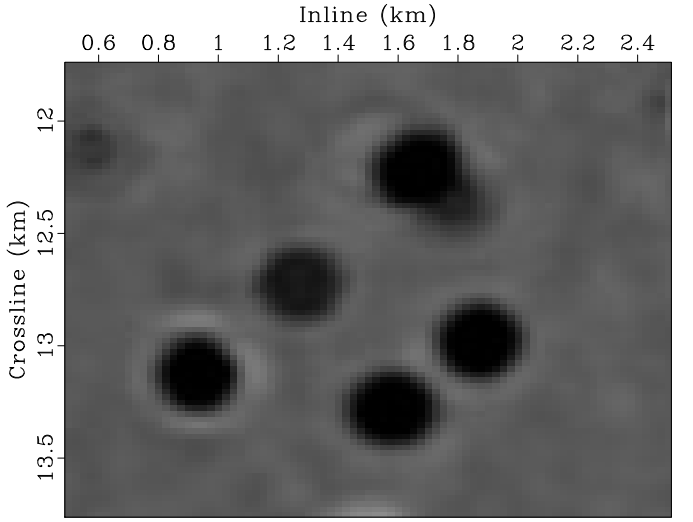

a

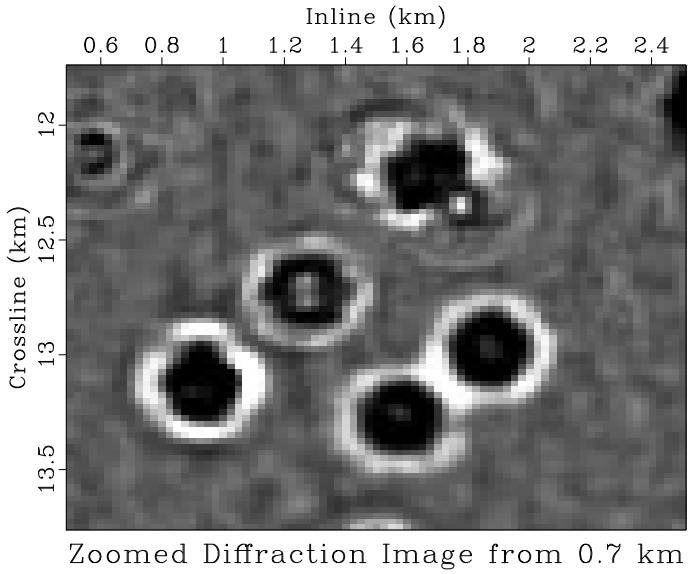

b

Figure 5.9: Zoomed Ordovician depth slices from 0.7 km: (a) conventional image; (b) seismic diffraction image chap04/ord20hz img2dstkb-2,dif2dstkb-2

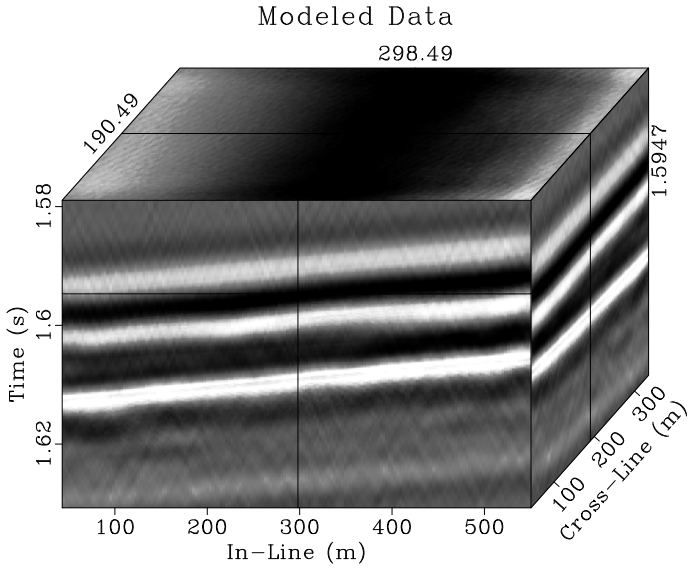

a

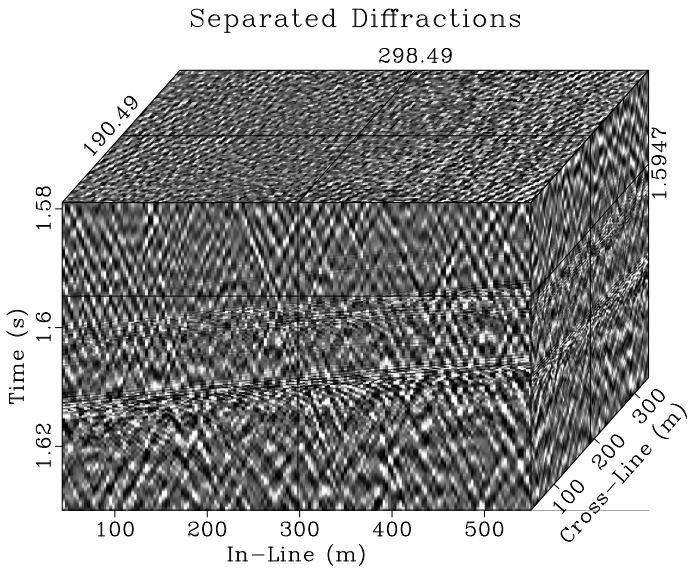

b

Figure 5.10: Zero-offset Khuff data: (a) conventional; (b) diffraction

chap04/smallkhuff zo-ovr,k-diffractions

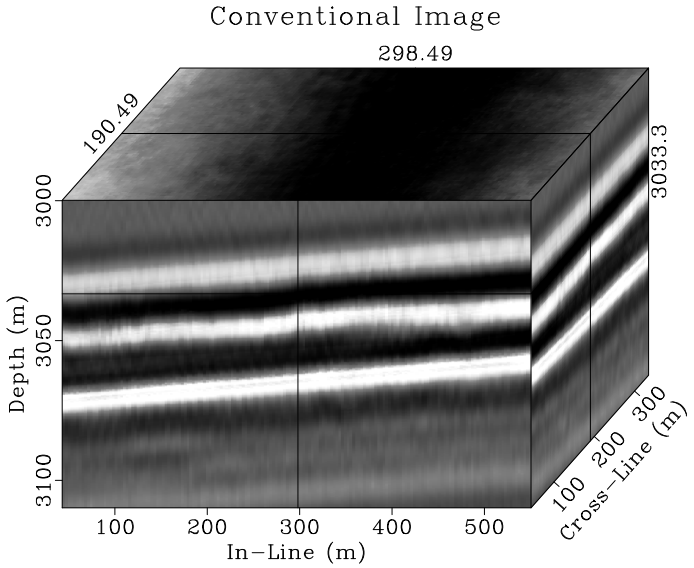

a

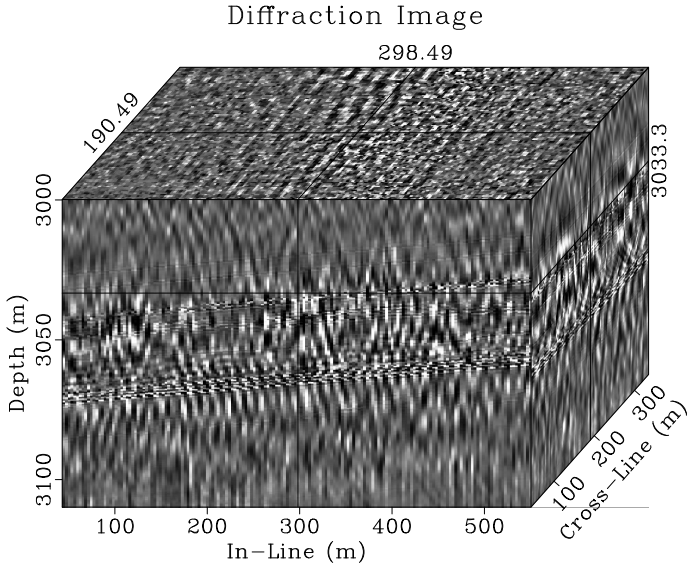

b

Figure 5.11: Migrated Khuff images: (a) conventional; (b) diffraction chap04/smallkhuff zo-ovr-mig,k-diffractions-mig

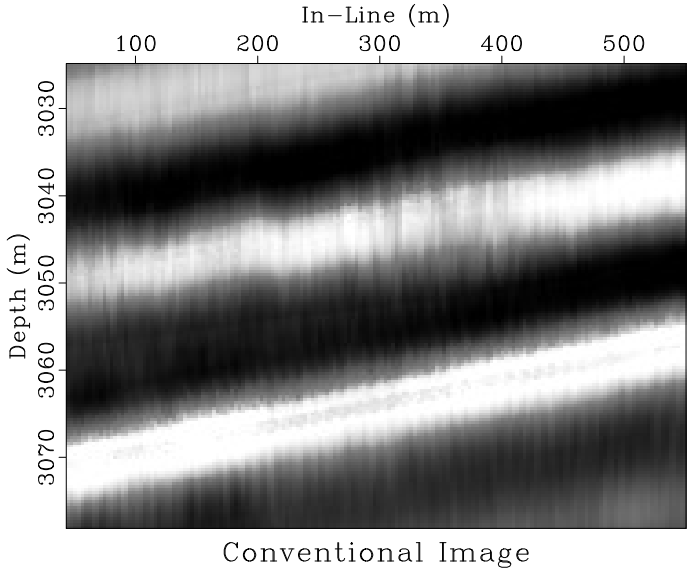

a

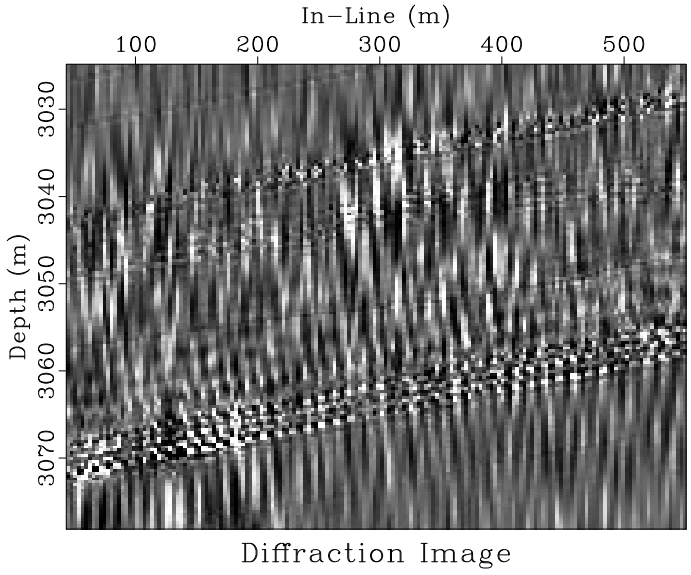

b

Figure 5.12: Khuff image cross sections with for 150 m Cross-Line: (a) conventional; (b) diffraction chap04/smallkhuff zo-ovr-migI,k-diffractions-migI

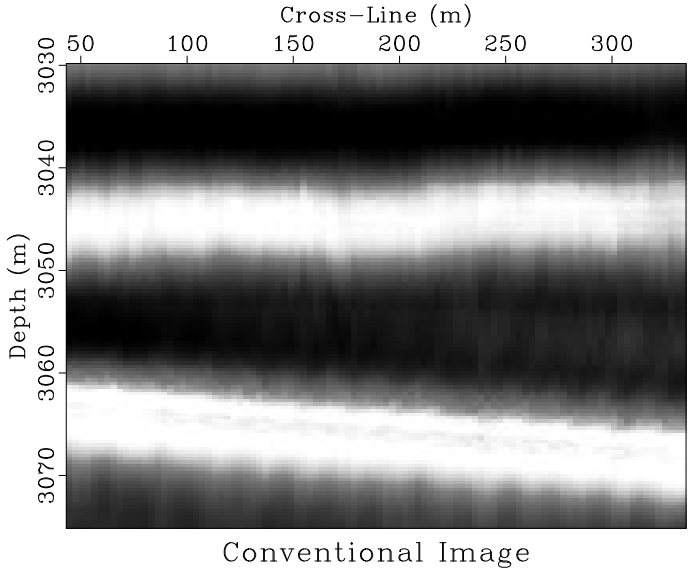

a

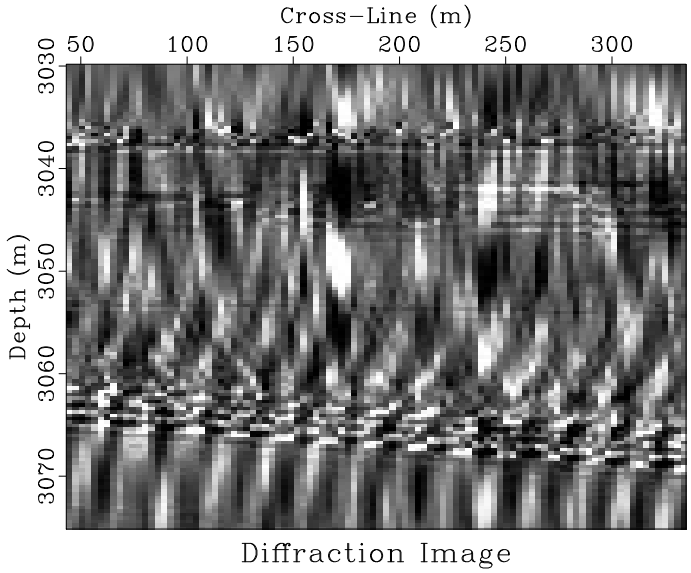

b

Figure 5.13: Khuff image cross sections with for 250 m In-Line: (a) conventional; (b) diffraction chap04/smallkhuff zo-ovr-migX,k-diffractions-migX

Ordovician

Seismic diffraction imaging improves the resolution of voids present in time slices relative to seismic reflection imaging. Examining the zoomed conventional and diffraction images from 0.55 km depth (Figures 5.7a and 5.7b) can enable the interpreter to tell that what appears as single shapes in the reflection image are actually superpositions of multiple void responses. Examining the features centered at Inline 8.85 km, Crossline 4.5 km; Inline 10.15 km, Crossline 4.25 km; and Inline 10 km Crossline 6.5 km in the conventional image, Figure 5.7a, responses are visible that may appear to be single voids. In the corresponding diffraction image, Figure 5.7b, these shapes separate into joined rings, which define the edges of two overlaying voids.

The deeper slices from 0.7 km depth illustrate how diffraction imaging increases void edge resolution. Comparing the voids visible in the zoomed image (Figure 5.9), using the diffraction image an interpreter may better discern where void edges are located; edges are marked by the reverse of seismic polarity. Additionally, diffraction imaging enables an interpreter to see that the feature centered at Inline 1.65 km, Crossline 12.25 km is actually a superposition of two nearby voids.

Therefore, using seismic diffraction imaging methods on the Ordovician model demonstrates its ability to better distinguish between overlaying voids in depth slices, and better spatially locate void edges.

Khuff

Seismic diffractions in the Khuff model highlight two strata with increased heterogeneity that are not immediately apparent in the conventional image.

Examining the Khuff seismic diffraction image, Figure 5.11b, I notice that

amongst a chaotic diffraction background, there are two upward sloping linear features which intersect the left side of the image cube's In-Line axis near depths of 3040 m and 3065 m, and the right side of the image cube's In-Line axis near 3030 m and 3055 m. These layers correspond to the heterogeneous zones in the acoustic impedance model, Figure 5.3. These heterogeneous regions are lost in the reflection image, Figure 5.11a, which features a series of parallel reflections.

Examining the diffraction image cross sections, Figures 5.12b and 5.13b provides a clearer view of the heterogenous layers, which remain less apparent in the corresponding conventional image cross sections, Figures 5.12a and 5.13a.

The heterogeneous strata are also apparent in the Khuff seismic diffraction data (Figure 5.10b). These strata, located where at the left edge of the cube's In-Line axis near Time 1.6 s and Time 1.618 s slope upward to the right, and are rich in hyperbolic diffractions.

I conclude that applying seismic diffraction imaging methods on the Khuff model helped to more accurately determine regions of heterogeneity in a reservoir-scale model.

CONCLUSIONS

Using two synthetic models, I have investigated the potential of seismic diffraction imaging for aiding seismic interpreters of carbonate systems. I use the first model to demonstrate how seismic diffraction imaging can better constrain the edges of voids and distinguish between the superposition of overlaying features. I use the second model to illustrate how diffraction imaging can detect reservoir-scale heterogeneous zones that might be indistinguishable in a conventional reflection image. Additional

case studies with field-data will be required to verify the effectiveness of these promising methods on real carbonate systems.

Chapter 6

Conclusions

Seismic diffractions are a fundamentally different phenomenon than seismic reflections. Because diffractions carry much less energy than seismic reflections they need to be extracted to be successfully used. Once separated, diffractions can be utilized to determine migration velocity and image geologically interesting features with greater resolution than that available in conventional reflection imaging.

I have examined three methods of seismic diffraction extraction: data domain plane-wave destruction, Fresnel zone elimination, and partial image plane wave destruction. I found Fresnel zone elimination, a method that extracts diffractions by muting the stationary phase of reflections in dip-angle gathers, their apex or Fresnel zone, to be a less powerful method because it masks diffraction energy existing within the stationary regions of reflections. Data domain plane-wave destruction (DD-PWD) is a powerful method of diffraction extraction, which uses PWD filters in the common-offset data domain to remove locally planar features in seismic data, including reflections. The method functions well, except for regions with complex seismic event geometry where its requirement of continuously variable data slope may be violated. I overcome that complication by proposing partial image plane-wave destruction (PI-PWD). This method accomplishes stationary phase elimination with PWD by destroying events in constant dip partial images coinciding with image slope. Reflection events with other slopes interfere destructively on stacking and therefore

can be ignored. PI-PWD is more computationally expensive than DD-PWD because of the added angle gather dimension of PWD, but removes more reflection energy in areas with complex geology. This is because migration produces an image that is simpler than the common-offset data for complex areas, enabling a more stable slope calculation.

I have proposed oriented velocity continuation to determine migration velocity by flattening diffraction events along slope gathers. The method functioned by decomposing data by slope and propagating different slope components in velocity in the midpoint-time-slope domain. Semblance is used as a measure of diffraction event flatness in these continued slope gathers, and velocities with the highest semblance are selected, indicating the migration velocity that best flattens diffraction events. This method holds potential for higher resolution velocity estimation, particularly after it is extended from zero-offset data to prestack data.

My experiments using two carbonate synthetic models illustrated how seismic diffraction imaging may be used to better resolve geologically interesting features or highlight heterogeneous zones in carbonate reservoirs that might be less apparent in a reflection image. In these experiments I generated synthetic zero-offset data, separated seismic diffractions using DD-PWD, and migrated the diffraction and complete data to generate diffraction and conventional images. Using this approach, I was better able to resolve the horizontal boundaries of voids in the first synthetic model, the Ordovician, while I was able to better resolve heterogenous strata in the second reservoir-scale model, the Khuff. Additional case studies will be required to demonstrate the promise of diffraction imaging for carbonate interpretation on real field-data.

According to the studies reported in this thesis, seismic diffractions can be a powerful tool for better understanding the subsurface. Successfully separated diffractions can be utilized in seismic data processing to determine migration velocities or migrated to better resolve the subsurface features that cause them. Much work remains to be done in the emerging field of seismic diffraction imaging, but the promise of higher resolution migration velocity analysis and high-resolution seismic images makes it an area worth of attention.

Bibliography

Adam, L., and M. Batzle, 2008, Elastic properties of carbonates from laboratory measurements at seismic and ultrasonic frequencies: The Leading Edge, **27**, no. 8, 1026–1032.

Al-Hadab, S., 2012, Diffraction imaging of sediment drifts in Cantebury Basin: M.S. Thesis, The University of Texas at Austin.

Audebert, F., P. Froidevaux, H. Rakotoarisoa, and J. Svay-Lucas, 2002, Insights into migration in the angle domain: 72nd Annual International Meeting, SEG, Expanded Abstracts, 1188–1191.

Baechle, G., A. Colpaert, G. Eberli, and R. Weger, 2008, Effects of microporosity on sonic velocity in carbonate rocks: The Leading Edge, **27**, no. 8, 1012–1018.

Baechle, G. T., R. J. Weger, G. P. Eberli, J. L. Mossaferro, and Y. F. Sun, 2005, Changes of shear moduli in carbonate rocks: Implications for gassmann applicability: The Leading Edge, **24**, 507–510.

Bashkardin, V., T. J. Browaeys, S. Fomel, F. Gao, and S. A. Mo, 2012, Phase-space computation of multi-arrival traveltimes: Part II Implementation and applicat ion to angle-domain imaging: SEG Technical Program Expanded Abstracts, **684**, 1–6.

Berkovitch, A., I. Belfer, Y. Hassin, and E. Landa, 2009, Diffraction imaging by multifocusing: Geophysics, **74**, no. 6, WCA75–WCA81.

Brandesberg-Dahl, S., M. V. de Hoop, and B. Ursin, 2003, Focusing in dip and ava compensation on scattering-angle/azimuth common image gathers: Geophysics, **68**, 232–254.

Burger, H. R., A. F. Sheehan, and C. H. Jones, 2006, Introduction to Applied Geophysics: W.W. Norton and Company.

Burnett, W., and S. Fomel, 2011, Azimuthally anisotropic 3D velocity continuation: International Journal of Geophysics, Article ID 484653.

Chapman, C., 2004, Fundamentals of Seismic Wave Propagation: Cambridge.

Chen, Z., S. Fomel, and W. Lu, 2013a, Accelerated plane-wave destruction: Geophysics, **78**, no. 1.

———, 2013b, Omnidimensional plane-wave destruction: Geophysics, **78**, no. 5.

Cheng, J., J. Geng, H. Wang, and Z. Ma, 2011, 3D Kirchhoff prestack time migration in average illumination-azimuth and incident-angle domain for isotropic and vertical transversely isotropic media: Geophysics, **76**, S15S27.

Claerbout, F. F., 1986, Velocity extrapolation by cascaded 15 degree migration, *in* SEP-48: Stanford Exploration Project, 79–84.

Claerbout, J., 1992, Earth sounding analysis: Processing versus inversion: Blackwell Scientific Publications, Inc.

Claerbout, J. F., 2005, Basic Earth Imaging: Stanford Exploration Project.

Courant, R., and D. Hilbert, 1989, Methods of mathematical physics: John Wiley & Sons.

Crummett, W. P., 1986, Seismic exploration: The Physics Teacher, **24**, 462–471.

Decker, L., and S. Fomel, 2014, Diffraction imaging and velocity analysis using oriented velocity continuation: SEG Technical Program Expanded Abstracts, Submitted.

Decker, L., X. Janson, and S. Fomel, 2014, Carbonate reservoir characterization using seismic diffraction imaging: Interpretation, Submitted.

Decker, L., and A. Klokov, 2014, Diffraction extraction by plane-wave destruction of partial images: SEG Technical Program Expanded Abstracts, Submitted.

Decker, L., A. Klokov, and S. Fomel, 2013, Comparison of seismic diffraction imaging techniques: Plane wave destruction versus apex destruction: SEG Technical Program Expanded Abstracts, 4054–4059.

Eberli, G. P., G. T. Baechle, F. S. Anselmetti, and M. L. Incze, 2003, Factors contrillong elastic properties in carbonate sediments and rocks: The Leading Edge, **22**, 654–660.

Eberli, G. P., J. L. Massaferro, and J. F. Sarg, 2004, Introduction; Seismic imaging of carbonate reservoirs and systems, *in* Seismic Imaging of Carbonate Reservoirs and Systems: Eberli, G.P., Massaferro, J.L., and Sarg, J.F., eds., AAPG Memoir: Tulsa, American Association of Petroleum Geologists, 1–9.

Evans, L. C., 2010, Partial differential equations, 2nd ed.: American Mathematical Society.

Fehler, M. C., and L. Huang, 2002, Modern Imaging Using Seismic Reflection Data: Annual Review of Earth and Planetary Sciences, **30**, 259–284.

Fomel, S., 2002, Applications of plane wave destruction filters: Geophysics, **67**, no. 6, 1946–1960.

———, 2003a, Angle-domain seismic imaging and the oriented wave equation: Society of Exploration Geophysicists 73rd Annual International Meeting Expanded Abstracts, 893–898.

———, 2003b, Time-migration velocity analysis by velocity continuation: Geophysics, **68**, no. 5, 1662–1672.

———, 2003c, Velocity continuation and the anatomy of residual prestack time migration: Geophysics, **68**, 1650–1661.

———, 2007, Shaping regularization in geophysical-estimation problems: Geophysics, **72**, no. 2, R29–R36.

———, 2009, Adaptive multiple subtraction using regularized nonstationary regression: Geophysics, **74**, V25–V33.

Fomel, S., and A. Guitton, 2006, Regularizing seismic inverse problems by model reparameterization using plane-wave construction: Geophysics, **71**, no. 5, A43–A47.

Fomel, S., and E. Landa, 2014, Structural uncertainty of time-migrated seismic images: Journal of Applied Geophysics, **101**.

Fomel, S., E. Landa, and M. T. Taner, 2007, Poststack velocity analysis by separation and imaging of seismic diffractions: Geophysics, **72**, no. 6, U89–U94.

Fomel, S., and M. Prucha, 1999, Angle-gather time migration, *in* SEP-100: Stanford Exploration Project, 141–150.

Fomel, S., P. Sava, I. Vlad, Y. Liu, and V. Bashkardin, 2013a, Madagascar: open-source software project for multidimensional data analysis and reproducible computational research: Journal of Open Research Software, **1**, e8.

Fomel, S., L. Ying, and X. Song, 2013b, Seismic wave extrapolation using lowrank symbol approximation: Geophysical Prospecting, **61**, 526–536.

Fomel, S. B., 1994, Method of velocity continuation in the problem of temporal seismic migration: Russian Geology and Geophysics, **35**, 100–111.

Fontaine, J. M., R. Cussey, J. Lacaze, R. Lanaud, and L. Yapaudjian, 1987, Seismic interpretation of carbonate depositional environments: AAPG Bulletin, **71**, 281–297.

Fowler, C. M. R., 2004, The Solid Earth: An Introduction to Global Geophysics: Cambridge University Press.

Gazdag, J., and P. Sguazzero, 1984, Migration of seismic data by phase-shift plus interpolation: Geophysics, **49**, 124–131.

Ghosh, S., and S. Fomel, 2012, Multiple suppression in the t-x-p domain: 82nd Annual International Meeting, SEG, Expanded Abstracts, `http://dx.doi.org/10.1190/segam2012--1398.1`.

Harlan, W., J. Claerbaut, and F. Rocca, 1984, Signal to noise separation and velocity estimation: Geophysics, **49**, no. 11, 1869–1880.

Janson, X., and S. B. Fomel, 2011, 3-D forward seismic model of an outcrop-based geocellular model, *in* Outcrops revitalized: tools, techniques and applications: Martinsen, O., Pulham, A.J., Haughton, P.D.W., and Sullivan, M.D. eds, volume **10** *of* SEPM Concepts in Sedimentology and Paleontology, 87–106.

Janson, X., F. J. Lucia, J. A. Bellian, A. A. AbuBshai, R. K. Al-Dukhayyail, H. W. Mueller III, and D. Cantrell, 2013, Chapter 12: Outcrop-based 3d geological and reservoir model of the uppermost Khuff Formation in central Saudi Arabia, *in* Permo-Triassic Sequence of the Arabian Plate: Ppelreiter, M., ed., EAGE Special Publication, 269–302.

Janson, X., H. Zeng, B. Loucks, A. John, Y. G. Jackson, Q. Wang, and C. Wang, 2010, An Ultra-Deep Paleokarst System in the Ordovician North-Central Tarim Basin China: Outcrop Analog And Synthetic Seismic Models: 80th Annual International Meeting, SEG, Expanded Abstracts.

Kanasewich, E. R., and S. M. Phadke, 1988, Imaging discontinuities on seismic sections: Geophysics, **53**, no. 3.

Keller, J. B., 1962, Geometrical Theory of Diffraction: Journal of the Optical Society of America, **52**, 116–130.

Kessinger, W., 1992, Extended split-step Fourier migration: 62nd Annual International Meeting, SEG, Expanded Abstracts, 917–920.

Khaidukov, V., E. Landa, and T. Moser, 2004, Diffraction imaging by focusing-defocusing: an outlook on seismic super resolution: Geophysics, **56**, 1478–1490.

Klem-Musatov, K., 1994, Theory of seismic diffractions: SEG.

Klokov, A., and S. Fomel, 2012, Separation and imaging of seismic diffractions using migrated dip-angle gathers: Geophysics, **77**, S131–S143.

———, 2013a, Seismic diffraction imaging, one dip at a time: SEG Technical Program Expanded Abstracts, 3697–3702.

———, 2013b, Selecting an optimal aperture in Kirchhoff migration using dip-angle gathers: Geophysics, **76**, no. 6.

Koren, Z., and I. Ravve, 2011, Full-azimuth subsurface angle domain wavefield decomposition and imaging part I: Directional and reflection image gathers: Geophysics, **76**, no. 1, S1–S13.

Kozlov, E., N. Baransky, E. Korolev, A. Antonenkoa, and E. Koshchuck, 2004, Imaging scattering objects masked by specular reflections: 74th Annual International Meeting, SEG, Expanded Abstracts, 1131–1134.

Landa, E., S. Fomel, and M. Reshef, 2008, Separation, imaging, and velocity analysis of seismic diffractions using migrated dip-angle gathers: 78th Annual International Meeting, SEG, Expanded Abstracts, 2176–2180.

Landa, E., and S. Keydar, 1998, Seismic monitoring of diffraction images for detection of local hetorogeneities: Geophysics, **63**, 1096–1100.

Landa, E., V. Shtivelman, and B. Gelchinsky, 1987, A method for detection of diffracted waves on common-offset sections: Geophysical Prospecting, **34**, 359–373.

Larner, K., and C. Beasley, 1987, Cascaded migrations -Improving the accuracy of finite-difference migration: Geophysics, **52**, 618–643.

Liu, Y., and S. Fomel, 2013, Seismic data analysis using local time-frequency decomposition: Geophysical Prospecting, **74**, 516–525.

Lucia, F. J., 1999, Carbonate Reservoir Caracterization: An Integrated Approach: Springer.

Moser, T., and C. Howard, 2008, Diffraction imaging in depth: Geophysical Prospecting, **56**, j.1365–2478.

Neidell, N. S., 1997, Perceptions in seismic imaging part 2: Reflective and diffractive contributions to seismic imaging: The Leading Edge, **16**, no. 9.

Onajite, E., 2013, Seismic data analysis techniques in hydrocarbon exploration: Elsevier.

Ottolini, R., 1986, Signal/noise separation in dip space, *in* SEP-37: Stanford Exploration Project, 143–150.

Palaz, I., and K. J. Marfurt, 1997, Chapter 1: Carbonate Seismology: an overview, *in* Carbonate Seismology: I. Palaz and K. J. Marfurt, ed., volume **6** *of* SEG Geophysical Developments, 1–7.

Reshef, M., and E. Landa, 2009, Poststack velocity analysis in the dip-angle domain using diffractions: 70th Conference and Exhibition, EAGE, Expanded Abstracts.

Rothman, D. H., S. A. Levin, and F. Rocca, 1985, Residual migration - Applications and limitations: Geophysics, **50**, 110–126.

Sava, P. C., B. Biondi, and J. Etgen, 2005, Wave-equation migration velocity analysis by focusing diffractions and reflections: Geophysics, **70**, no. 3.

Sayers, C., 2008, The elastic properties of carbonates: The Leading Edge, **27**, no. 8, 1020–1024.

Sayers, C., and R. Latimer, 2008, An introduction to this special section: Carbonates: The Leading Edge, **27**, no. 8, 1010–1011.

Stein, S., 2002, An Introduction to Seismology, Earthquakes and Earth Structure: Blackwell Publishing.

Sturzu, I., A. M. Popovici, N. Tanushev, I. Musat, M. A. Pelisser, and T. J. Moser, 2013, Specularity gethers for diffraction imaging: 75th Annual International Conference and Exhibition, EAGE, Expanded Abstracts.

Taner, M. T., S. Fomel, and E. Landa, 2006, Prestack separation of seismic diffractions using plane-wave decomposition: 76th Annual International Meeting, SEG, Expanded Abstracts, 2401–2404.

Ursin, B., M. V. de Hoop, S. Brandsberg-Dahl, and A. Sollid, 2005, Seismic angle migration: The Leading Edge, **24**, 116–130.

Vanario, T., C. Scotellard, and G. Mavko, 2008, The effect of chemical and physical processes on the acoustic properties of carbonate rocks: The Leading Edge, **27**, no. 8, 1040–1048.

Červený, V., 2001, Seismic Ray Theory: Cambridge University Press.

Ventosa, S., C. Simon, and M. Schimmel, 2012, Window length selection for optimum slowness resolution of the local-slant-stack transform: Geophysics, **77**, V31–V40.

Wang, Z., 1997, Seismic properties of carbonate rocks, *in* Carbonate Seismology: I. Palaz and K. J. Marfurt, ed., volume **6** *of* SEG Geophysical Developments, 29–52.

Weger, R., G. P. Eberli, G. Baechle, J. L. Masaferro, and Y. F. Sun, 2009, Quantification of pore structure and its effect on sonic velocity and permeability in carbonates: The Leading Edge, **93**, 1297–1317.

Xu, S., H. Chauris, G. Lambare, and M. Noble, 2001, Common-angle migration: A strategy for imaging complex media: Geophysics, **66**, 1877–1894.

Zeng, H., R. Loucks, X. Janson, G. Wang, Y. Xia, B. Yuan, and L. Xu, 2011a, Three-dimensional seismic geomorphology and analysis of the Ordovician paleokarst drainage system in the central Tabei Uplift, northern Tarim Basin, western China: AAPG Bulletin, **95**, no. 12.

Zeng, H., G. Wang, X. Janson, R. Loucks, Y. Xu, and B. Yuan, 2011b, Case History Characterizing seismic bright spots in deeply buried, Ordovician Paleokarst strata, Central Tabei uplift, Tarim Basin, Western China: Geophysics, **76**, no. 4, B127–B137.

Zhang, Y., and J. Sun, 2009, Practical issues in reverse time migration: true amplitude gathers, noise removal and harmonic source encoding: First Break, **26**, 29–35.

Vita

Luke Decker was born in Seattle, Washington. After completing high school at Bishop Blanchet in 2004 he left Seattle for Walla Walla, Washington, where he enrolled at Whitman College studying physics. After graduating with his bachelor's degree in 2008 he went to work for King Canyon Buffalo, Inc. as a mudlogger working on drilling rigs across the continental United States. Early in 2011 he returned to school at Western Washington University in Bellingham, Washington. He graduated from WWU with a bachelor's degree in geophysics at the end of the year. In August 2012 he entered graduate school as a member of the Texas Consortium for Computational Seismology at the University of Texas at Austin's Bureau of Economic Geology. When Luke is not working or studying he loves bicycle touring.

Permanent address: 7530 12th Ave. NE Seattle, WA 98115

This thesis was typeset with LaTeX[†] by the author.

[†]LaTeX is a document preparation system developed by Leslie Lamport as a special version of Donald Knuth's TeX Program.